Development and validation of two novel x-ray filters in computed tomography with focus on fluence modulation for region-of-interest imaging

Sascha Manuel Huck

München 2021

Development and validation of two novel x-ray filters in computed tomography with focus on fluence modulation for region-of-interest imaging

Sascha Manuel Huck

Dissertation
der Fakultät für Physik
der Ludwig-Maximilians-Universität
München

vorgelegt von
Sascha Manuel Huck
aus Bruchsal

München, den 22. Juni 2021

Erstgutachter: Prof. Dr. Katia Parodi
Zweitgutachter: Prof. Dr. Thomas Flohr
Tag der mündlichen Prüfung: 4. August 2021

Zusammenfassung

Entwicklung und Validierung zweier neuartiger Röntgenfilter für die Computertomographie mit Fokus auf Fluenzmodulation für "Region-of-Interest" Bildgebung

Die Röntgen-Computertomographie (CT) hat sich zu einem zentralen Element der klinischen Bildgebung entwickelt. Sie liefert Schichtbilder, die sich durch eine hohe zeitliche und räumliche Auflösung bei sehr kurzen Aufnahmezeiten auszeichnen. Allerdings verwendet die CT zur Bildaufnahme ionisierende Röntgenstrahlung, die ein potenzielles Gesundheitsrisiko für den Patienten darstellt. Über die Jahre wurden viele Maßnahmen ergriffen, um die Strahlendosis zu reduzieren. Ein Ansatz ist die dynamische Vorfilterung des Röntgenstrahls, um die Abschwächung der Röntgenstrahlung durch den Patienten, die über die Projektionen und die Fächerstrahlbreite variiert, zu kompensieren. Bowtie-Filter moderner CT Systeme nach dem Stand der Technik sind jedoch statische Vollkörper und können sich nicht an die individuelle Patientenschwächung anpassen. Eine Lösung für patienten- und aufgabenspezifische CT Bildgebung ist die Modulation des Fluenzbereichs (FFM) unter Verwendung eines dynamischen Strahlabschwächers (DBA). DBAs ermöglichen es, die Röntgenfluenz während der Datenaufnahme anzupassen. Existierende DBA-Konzepte zeigen jedoch grundsätzliche Schwachstellen (z.B. zu groß oder zu langsam), die eine Realisierung in klinischen CT Systemen ausschließen.

In dieser Thesis wurden zwei grundlegend neue DBA-Konzepte entwickelt, um die mangelnde Flexibilität derzeitiger Bowtie-Filter und die Einschränkungen bisheriger DBA-Ansätze zu überwinden. Der lamellenbasierte DBA (sbDBA) besteht aus einer Anordnung von stark röntgenabsorbierenden Lamellen. Je nach Verkippung des sbDBA verändert sich die Transmission durch den sbDBA – vergleichbar mit Jalousien. Auch der artverwandte, z-ausgerichtete sbDBA (z-sbDBA) besitzt Absorptionslamellen zur FFM, verwendet jedoch eine überarbeitete Strukturierung und eine einfachere Mechanik. Ausgehend von einfachen Skizzen wurden reale Prototypen des sbDBA und des z-sbDBA gebaut und in ein klinisches CT System integriert.

Im ersten Teil dieser Arbeit wurden das modifizierte CT System und Monte-Carlo Simulationen, die dieses CT System nachbilden, verwendet, um die DBAs zu untersuchen. In Versuchsmessungen konnten beide DBAs verschiedene Transmissionprofile erzeugen und somit FFM – die Hauptfunktion eines DBA – realisieren. Während der sbDBA auch die Verschiebung der Maximaltransmission erlaubte, wurden mit dem z-sbDBA geeignetere Verläufe der Transmissionsprofile erzielt. Ein Vergleich spektraler Abhängigkeit der Transmission und DBA-induzierter Streustrahlung zeigte bemerkenswerte Vorteile gegenüber herkömmlichen Bowtie-Filtern. Obwohl einzelne Ringartefakte in ersten Bildrekonstruktionen Herausforderung hinsichtlich der mechanischen Stabilität der DBAs aufzeigten, war die Bildqualität insgesamt vielversprechend.

Im zweiten Teil wurde das Potenzial für Zielvolumen (ROI) Bildgebung untersucht, bei der nur ein bestimmter Bereich mit hoher Qualität dargestellt und im umliegenden Gewebe die Dosis minimiert wird. Zunächst wurde hierzu ein Optimierungskriterium entwickelt, mit dem die Kippbewegungen der DBAs hinsichtlich eines diagnostischen Ziels optimiert werden. Dabei soll die Patientendosis minimiert und die Bildqualität innerhalb der ROI maximiert werden. Die erzeugten DBA-Trajektorien passten die emittierte Röntgenfluenz an die Geometrie der ROI an. Anschließend wurden verschiedene FFM-Konfigurationen, einschließlich Röhrenstrommodulation und zweier Bowtie-Filter, mit den DBAs bezüglich ihrer Dosiseffizienz bei ROI-Bildgebung verglichen. Es zeigte sich, dass die DBAs die Röntgenstrahlung effizienter einsetzten als Bowtie-Filter moderner CT Systeme: Bei Verwendung der DBAs konnten die ROIs bei gleichbleibender Bildqualität mit bis zu 30 % (z-sbDBA) bzw. 60 % (sbDBA) weniger Dosis im Vergleich zu einem typischen Bowtie-Filter dargestellt werden.

In dieser Arbeit wurden zwei neuartige DBA-Konzepte entwickelt und in ein klinisches CT System installiert. Diese DBAs wurden hinsichtlich FFM erfolgreich validiert und zeigten bei ROI-Bildgebung erhebliches Dosiseinsparpotential im Vergleich zu heutiger FFM-Technik. Die vielversprechenden Ergebnisse bilden eine Grundlage für zukünftige Dosisreduktionen und ebnen den Weg für ROI-Bildgebung in der CT Diagnostik.

Abstract

Development and validation of two novel x-ray filters in computed tomography with focus on fluence modulation for region-of-interest imaging

X-ray computed tomography (CT) imaging has become a workhorse of today's clinical imaging. It provides cross-sectional diagnostic images featuring high temporal and spatial resolution at very short acquisition times. However, CT images are acquired using x-rays, which bears a potential health detriment to the patient due to ionization radiation. Over the decades, many efforts have been undertaken to reduce the radiation burden. One approach is to employ dynamic pre-filtration of the x-ray beam to compensate for the patient's x-ray attenuation that changes across the projections and the fan beam angle. State-of-the-art bowtie filters in clinical CT systems, however, are static and therefore cannot adapt to patient attenuation individually. A solution for patient- and task-specific CT imaging is fluence field modulation (FFM) by employing a dynamic beam attenuator (DBA). DBAs are capable of adapting the x-ray fluence during the data acquisition. Existing DBA concepts, however, suffer from inherent limitations (e.g., too large or too slow) that preclude an implementation in clinical CT systems.

In this thesis, two fundamentally new DBA concepts were developed to overcome the lack of flexibility of present bowtie filters and the pitfalls of previous DBA approaches. The sheet-based DBA (sbDBA) was composed of an array of highly x-ray attenuating sheets. Depending on the way the sbDBA was tilted, the transmission through the sbDBA changed – comparable to Persian blinds. Likewise, the z-aligned sbDBA (z-sbDBA) employed attenuation sheets for FFM, although it used a revised structuring and simplified mechanics. Starting from simple sketches, physical prototypes of the sbDBA and the z-sbDBA were built and integrated into a clinical CT system.

In the first part of this thesis, the DBAs were investigated using the modified CT system and Monte Carlo simulations mimicking this CT system. In experimental measurements, both DBAs were able to realize a wide range of transmission profiles and therefore successfully demonstrated their feasibility of FFM — the key function of a DBA. While the sbDBA allowed to shape the transmission profiles more flexibly by shifting the peak transmission also laterally, the z-sbDBA realized more suitable shapes. A comparison regarding the spectral dependency of the transmission and attenuator-induced scatter revealed remarkable advantages over conventional bowtie filters. Although ring artifacts in first-time image reconstructions unveiled challenges concerning the mechanical reliability of the DBAs, the overall image quality was promising.

In the second part, the potential for region-of-interest (ROI) imaging, where only a specific region is imaged at high quality while the dose is minimized in surrounding tissue, was explored. In the first step, an optimization objective was developed to optimize the angular movements of the DBA regarding a given imaging task. The optimization aims at minimizing the patient dose and maximizing the image quality inside the ROI. The optimized DBA movements reasonably adapted the emitted x-ray fluence to the geometry of the ROI. In the second step, different FFM configurations, including tube current modulation and different bowtie filters, were compared with the DBAs regarding their dose efficiency in ROI imaging. The DBAs were shown to exploit the x-ray radiation more efficiently than the bowtie filters of modern CT systems: using the DBAs, the ROIs were imaged with up to 30 % (z-sbDBA) or 60 % (sbDBA) less radiation dose compared to a typical bowtie filter while maintaining the image quality in the ROI.

In conclusion, two novel DBA concepts were developed and installed into a clinical CT system. These DBAs were successfully validated regarding FFM and demonstrated a remarkable dose saving potential in ROI imaging compared to state-of-the-art FFM technology. The promising results give rise for future radiation dose reductions and pave the way to ROI imaging in diagnostic CT.

Contents

List of Publications

Publications in scientific journals

I. S. M. Huck, G. S. Fung, K. Parodi, and K. Stierstorfer. "Sheet-based dynamic beam attenuator – A novel concept for dynamic fluence field modulation in x-ray CT". In: *Medical Physics* 46.12 (2019), pp. 5528–5537. DOI: 10.1002/mp.13690.

II. S. M. Huck, G. S. Fung, K. Parodi, and K. Stierstorfer. "The z-sbDBA, a new concept for a dynamic sheet-based fluence field modulator in x-ray CT". In: *Medical Physics* 47.10 (2020), pp. 4827–4837. DOI: 10.1002/mp.14430.

III. S. M. Huck, G. S. Fung, K. Parodi, and K. Stierstorfer. "On the potential of ROI imaging in x-ray CT - A comparison of novel dynamic beam attenuators with current technology". In: *Medical Physics* (2021). In Press. DOI: 10.1002/MP.14879.

Contributions to international conferences

I. S. M. Huck, K. Parodi, and K. Stierstorfer. "First experimental validation of a novel concept for dynamic beam attenuation in CT". In: *CT-Meeting: Fifth International Conference on Image Formation in X-Ray Computed Tomography*. Ed. by F. Noo. Salt Lake City, UT, USA, May 2018, pp. 24–27. URL: https://www.ct-meeting.org/data/ProceedingsCTMeeting2018.pdf. Extended oral presentation.

II. S. M. Huck, G. S. Fung, K. Parodi, and K. Stierstorfer. "Optimized intensity modulation for a dynamic beam attenuator in x-ray computed tomography". In: *Medical Imaging 2019: Physics of Medical Imaging*. Ed. by T. G. Schmidt, G.-H. Chen, and H. Bosmans. Vol. 10948. International Society for Optics and Photonics (SPIE). San Diego, CA, USA, Feb. 2019, p. 1094824. DOI: 10.1117/12.2511704. Oral presentation.

III. S. M. Huck, G. S. Fung, K. Parodi, and K. Stierstorfer. "A New Concept for Fluence Field Modulation in X-ray CT: the z-sbDBA". In: *Medical Imaging 2020: Physics of Medical Imaging*. Ed. by G.-H. Chen and H. Bosmans. Vol. 11312. International Society for Optics and Photonics (SPIE). Houston, TX, USA, Feb. 2020, p. 1131202. DOI: 10.1117/12.2543185. Oral presentation.

IV. S. M. Huck, G. S. Fung, K. Parodi, and K. Stierstorfer. "Fluence field modulation in x-ray CT for ROI imaging: Optimization of primary fluence and comparison of attenuator scenarios". In: *CT-Meeting: Sixth International Conference on Image Formation in X-Ray Computed Tomography*. Ed. by M. Kachelrieß. Regensburg, Germany (online), Aug. 2020, pp. 214–217. URL: https://www.ct-meeting.org/data/ProceedingsCTMeeting2020.pdf. Oral presentation.

V. S. M. Huck, G. S. Fung, K. Parodi, and K. Stierstorfer. "A method for optimization of the x-ray tube current in ROI imaging using a simulation framework for radiation dose and image quality calculation for arbitrary fluence distributions". In: *Medical Imaging 2021: Physics of Medical Imaging*. Ed. by H. Bosmans, W. Zhao, and L. Yu. Vol. 11595. International Society for Optics and Photonics (SPIE). San Diego, CA, USA (online), Feb. 2021, p. 1159505. DOI: 10.1117/12.2580828. Oral presentation.

Contributions to national conferences

I. S. M. Huck, K. Parodi, and K. Stierstorfer. "Erstmalige experimentelle Validierung eines neuartigen Konzeptes zur dynamischen Intensitätsmodulation in CT". In: *Abstractband der 49. Jahrestagung der Deutschen Gesellschaft für Medizinische Physik (DGMP)*. Ed. by C. Bert, M. Wucherer, and F. B. Laun. Nürnberg, Germany, Sept. 2018, pp. 183–184. ISBN: 978-3-9816002-5-4. URL: https://cdn.dgmp.de/media/document/3018/DGMP-und-ISMRM-DS-2018-Abstractband.pdf. Oral presentation, nominated for the *Young Investigator Award*.

II. S. M. Huck, G. S.-K. Fung, K. Parodi, and K. Stierstorfer. "Optimierte Intensitätsmodulation für einen dynamischen Formfilter in CTs". In: *Abstractband der 50. Jahrestagung der Deutschen Gesellschaft für Medizinische Physik (DGMP)*. Ed. by C. Gromoll and N. Wegner. Stuttgart, Germany, Sept. 2019, pp. 197–198. ISBN: 978-3-948023-08-9. URL: https://cdn.dgmp.de/media/document/3147/DGMP2019-Abstractband.pdf. Poster presentation.

III. S. M. Huck, G. S.-K. Fung, K. Parodi, and K. Stierstorfer. "z-sbDBA – ein neues Konzept zur dynamischen Röntgenflussmodulation in CT". In: *Abstractband der 51. Jahrestagung der Deutschen Gesellschaft für Medizinische Physik (DGMP)*. Ed. by U. Wolf and B. Sattler. Leipzig, Germany (online), Sept. 2020, pp. 297–298. ISBN: 978-3-948023-10-2. URL: https://www.dgmp-kongress.de/fileadmin/_newsletter/DGMP2020_Abstractband.pdf. Oral presentation, nominated for the *Young Investigator Award*.

List of Acronyms

a/p	anterior/posterior
ALARA	as low as reasonably achievable
ASG	anti-scatter grid
CNR	contrast-to-noise ratio
CT	Computed tomography
CTDI	computed tomography dose index
DBA	dynamic beam attenuator
DNA	deoxyribonucleic acid
DRASIM	Deterministic Radiological Simulation
EADL	Evaluated Atomic Data Library
EPDL	Evaluated Photon Data Library
FBP	filtered backprojection
FDBF	fluid-filled dynamic bowtie filter
FFM	fluence field modulation
FOV	field of view
FPGA	field-programmable gate array
hsqTCM	heuristic square root TCM
HU	Hounsfield unit
ICRP	International Commission on Radiological Protection
IMCT	intensity-modulated computed tomography
IMRT	intensity modulated radio therapy
LNT	linear-no-threshold
MAD	multiple aperture device
MC	Monte Carlo
MOCASSIM	Monte Carlo Scatter Simulation

NEA	Nuclear Energy Agency
NPS	noise power spectrum
PCCT	photon counting computed tomography
PCD	photon counting detector
PMMA	polymethyl methacrylate
ROI	region-of-interest
sbDBA	sheet-based dynamic beam attenuator
SNR	signal-to-noise ratio
TCM	tube current modulation
VOI	volume-of-interest
WLAN	wireless local area network
z-sbDBA	z-aligned sheet-based dynamic beam attenuator

Chapter 1

Introduction

1.1 Motivation

"The health and well-being of my patient will be my first consideration"

says the second pledge of the Declaration of Geneva, a modern version of the Hippocratic Oath.[1] In principle, this oath of ethics obliges physicians to do no harm to the patient. However, a dilemma arises regarding the principle of non-maleficence as soon as it comes to diagnostic imaging using x-ray radiation. On the one hand x-ray imaging is the key to obtain additional diagnostic information, but on the other hand the radiation exposure is potentially harmful. In order to still do justice to the oath, the radiology community implemented guiding principles for radiation protection in medicine:[2,3]

1. Justification: a radiologic examination is justified if the expected benefit of the imaging procedure exceeds the associated, potential health detriment (Artikel 55).[3]
2. Optimization: the radiation exposure is to be optimized such that the radiation dose is kept as low as reasonably achievable (ALARA), in accordance with the diagnostic objective (Artikel 56).[3]

Before initiating a radiologic examination, the advantages and disadvantages of the examination must be thoroughly weighed under consideration of these major guidelines. Accordingly, an x-ray based examination – for example computed tomography (CT) imaging – should only be performed if the health risk is deemed to be justified and technical aspects of the examination are optimized. This thesis addresses the second principle, the aim of optimizing the radiation dose further.

The role of x-ray CT imaging in medical diagnostics and for the collective dose exposure

The success story of x-ray CT imaging began with its advent in 1972 and revolutionized radiology henceforth. CT imaging is a non-invasive imaging modality that provides diagnostic information about the interior of the examined patient. In contrast to conventional x-ray imaging, CT delivers sectional images of the desired body region that are not obscured by overlying anatomical structures.

Over the decades, CT systems have technologically advanced and feature superior spatial and temporal resolution, short acquisition times, and high contrast for dense tissue compared to other imaging modalities. Due to its improved performance, increase in application fields, and higher availability, CT imaging has become a workhorse in diagnostic imaging, today. The other side of the coin, however, is the radiation dose burden associated with the rising number of CT examinations, as shown in Figure 1.1.[4,5] Although the benefit of a proper CT examination outweighs the statistical health detriment at the individual level by far, the health burden of a growing collective dose – projected to an entire population – is certainly relevant for the health care system. It is noteworthy that even though the number of CT examinations accounts for only about one tenth of all x-ray procedures, they contribute to more than half of the overall collective dose from x-ray examinations in Europe, compare Figure 1.2.[6]

The increasing radiation dose associated with CT imaging and the public concerns about medical-driven radiation burden are focusing technical innovations on dose reduction strategies.[7–11] Driven by the aim of gaining diagnostic information at lower radiation dose to improve therapy and patient outcomes, CT imaging advances toward a more tailored imaging modality with improving dose efficiency.

This thesis contributes to this aim by introducing two x-ray filter concepts that facilitate a dynamic adaptation of the radiation exposure to the given imaging scenario. A dynamic modulation of the x-ray beam during the acquisition is the key to fluence field modulation (FFM) and region-of-interest (ROI) imaging in CT imaging. The research on these x-ray filters pursues the longstanding wish to realize task-specific and patient-centered CT examinations that deliver high-quality images at the lowest possible radiation dose to continue the success story of CT imaging.

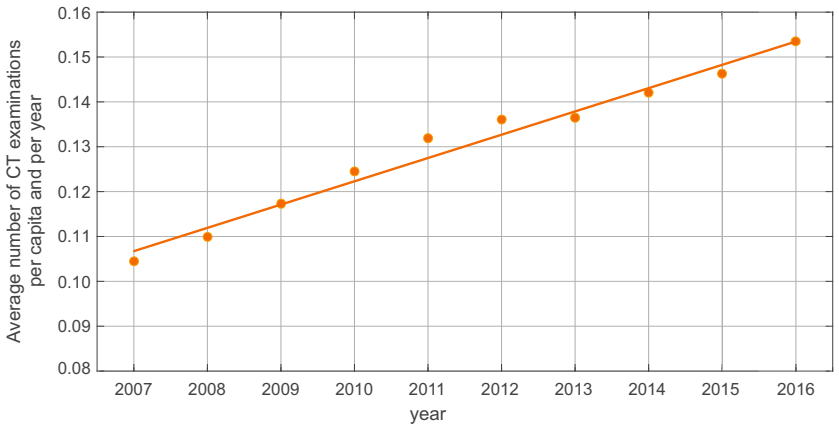

Figure 1.1: Increase of the average number of CT examinations in Germany per capita and per year from 2007 to 2016. A similar trend is observed in other European countries.[12–16] Data taken from the report of the German Federal Office for Radiation Protection (Bundesamt für Strahlenschutz) on *Umweltradioaktivität und Strahlenbelastung* (2021).[5]

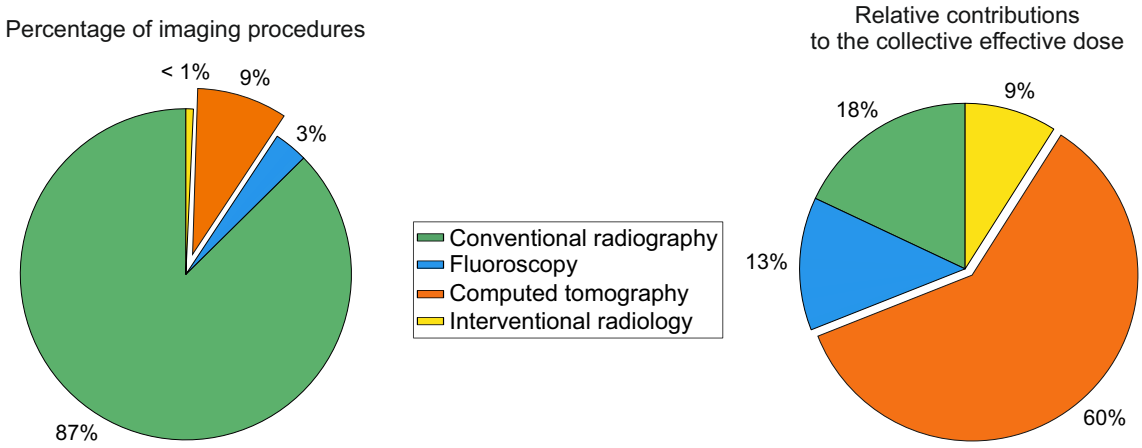

Figure 1.2: Contributions of x-ray examinations. Percentage of x-ray imaging procedures and their associated relative contributions to the overall collective effective dose in Europe (conventional radiography includes dental procedures; nuclear imaging not included). Data taken from the report of the European Commission on *Radiation Protection no. 180: Medical Radiation Exposure of the European Population* (2014).[6]

1.2 Physics of x-ray CT imaging

Diagnostic imaging using CT systems is based on the tissue-specific attenuation of x-ray radiation. Therefore, this section summarizes the fundamental physical principles relevant for x-ray CT imaging. First, the generation of x-rays and their spectral characteristics are explained, followed by a description of the relevant interaction processes with matter. The elaborations are focused on the properties of diagnostic x-rays as typically used in CT systems. The technical principles of a CT system, including the image acquisition and reconstruction, are introduced thereafter. Image quality and patient radiation dose are central performance indicators for CT imaging, which are detailed at the end of this section.

The physical and technical background of CT imaging is based on the literature stated at the beginning of each topic and the description is partly inspired by a previous master thesis of the author.[17] Each section provides the interested reader a selection of relevant literature offering more comprehensive details on the specific topic.

1.2.1 X-rays and x-ray generation

The x-ray tube represents a core component of a CT system. It generates the x-ray radiation, the electromagnetic radiation that penetrates the examined patient, from accelerated electrons in two different ways. The emission spectrum of the x-ray tube is a superimposition of both kinds of radiation, which can be modified by pre-filters and tube settings.

The background on x-ray radiation is mainly based on corresponding text books[18–22] and the reviews by Kalender,[23] Seibert and Boone,[24,25] and Hubbell,[26] which are recommended for a more detailed understanding of this topic.

X-ray radiation

Electromagnetic radiation builds upon periodic cyclic waves of electric and magnetic fields. The radiation travels at speed of light in vacuum (approximately $c \approx 3 \times 10^8\,\mathrm{m/s}$) and can transport energy. It is characterized by the spatial or temporal properties of the associated wave, corresponding to the wavelength or the frequency, respectively. The relation between the propagation velocity v, wavelength λ, and frequency f of radiation is given by

$$v = \lambda \cdot f. \tag{1.1}$$

Within the broad spectrum of naturally occurring electromagnetic waves (a few Hertz up to 10^{24} Hertz and beyond) x-ray radiation is a high-frequency, short-wavelength kind of radiation. It ranges in the order of $\lambda \approx 10^{-8}\,\mathrm{m}$ to $10^{-13}\,\mathrm{m}$. More common in CT imaging, however, is the denotation in photon energies which emphasizes the particle-like trait of x-ray radiation. In the particle regime, x-ray photons cover an energy range from about 100 eV to more than 10 MeV (e.g., in radiotherapy).[21] Accordingly, x-ray radiation is highly ener-

getic, which is described by the relationship between the frequency f and the corresponding energy E of the radiation,

$$E = h \cdot f, \tag{1.2}$$

where h denotes the Planck's constant ($h = 6.626 \times 10^{-34}\,\mathrm{Js}$). The spectrum of x-ray radiation overlaps with that of gamma radiation toward higher energies and ultraviolet radiation toward lower energies. X-ray and gamma radiation are indistinguishable, except for their origin. Gamma radiation is released from the atomic nucleus, e.g., in the process of a radioactive decay, whereas x-rays originate from interactions with electrons of the atomic shell. The part of the x-ray spectrum typically used for medical diagnostics covers the energy range from $E \approx 25\,\mathrm{keV}$ to $150\,\mathrm{keV}$. This photon energy corresponds to a wavelength of $\lambda \approx 10^{-11}\,\mathrm{m}$ to $10^{-12}\,\mathrm{m}$, which is about four orders of magnitude shorter than visible light.

Generation of x-rays

The x-ray radiation in CT is produced when highly accelerated electrons collide with the target material, see Figure 1.3. To this end, electrons are emitted from a heated cathode (about 2500 °C) by thermionic emission. A high voltage between the emitting cathode and the target anode, referred to as tube voltage U, accelerates the electrons toward the anode. Wehnelt cylinders focus the electron beam.[27] Considering the classical regime, the potential energy of the electrons in the electric field is transformed into kinetic energy

$$E = U \cdot e = \frac{m_e \cdot v^2}{2}, \tag{1.3}$$

where e denotes the elementary charge of an electron ($1.602 \times 10^{-19}\,\mathrm{C}$) and m_e the electron mass ($9.109 \times 10^{-31}\,\mathrm{kg}$). In a typical CT x-ray tube, the electrons reach about half the speed of light before they impinge on the anode. In the collision process, almost all kinetic energy is transformed into heat. Only a small portion of about 1 % can be used to generate x-rays. Two independent interaction mechanisms of the accelerated electrons with the anode material are relevant for the generation of x-rays: i) the deceleration of electrons in the electric field of the atomic nuclei to generate so-called *Bremsstrahlung* and ii) the interaction of the impinging electrons with electrons of the atomic shell resulting in the emission of characteristic radiation. The x-ray generation due to *Bremsstrahlung* on nuclei of the anode atoms is the dominant process compared to the contribution of characteristic x-ray radiation. The physical processes are detailed in the following paragraphs with focus on their application in CT imaging.

Bremsstrahlung

The majority of x-rays composing a usual CT x-ray spectrum results from *Bremsstrahlung*. Electrons that pass very close to an atomic nucleus in the anode material are decelerated and deflected by the electric field of the atomic nucleus. This change in motion is accompanied by an energy conversion where parts of the kinetic energy of the electrons are released

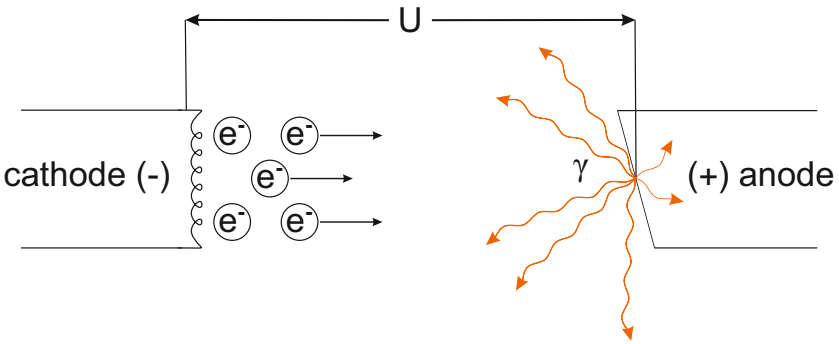

Figure 1.3: Scheme of an x-ray tube. Electrons are emitted by thermionic emission from the tube anode. The applied tube voltage U accelerates the electrons (e^-) toward the anode. The impinging electrons interact with the atoms of the anode material (typically tungsten) and produce x-ray photons (γ). Adapted from Oppelt (2005).[18]

as *Bremsstrahlung*. The transferred energy is carried by the emanating x-ray photons. The closer the electrons pass the atomic nucleus, the higher is the energy transfer and the photon energy. The electrons are either decelerated in several steps, releasing only a portion of their energy, or in a single event. In the latter case, which is very rare, the entire kinetic energy of the electrons, see Eq. 1.3, is transferred to the x-ray photons. The energy of these photons depends on the applied tube voltage as described by the *Duane-Hunt law*.[28] It determines the maximum possible energy of a photon $E_{\max}$ and the corresponding minimum wavelength λ_{min} as a function of the applied tube voltage U:

$$E_{\max} = U \cdot e = h \cdot \frac{c}{\lambda_{min}} \tag{1.4}$$

$$\lambda_{min} = \frac{h \cdot c}{U \cdot e}. \tag{1.5}$$

Typically, an impinging electron releases its energy step by step along its path through the anode material until all of its energy is dissipated. Thus, the energy transferred to the photons E_γ can assume any value between $E_\gamma = 0\,\mathrm{keV}$ and the maximum photon energy $E_\gamma = E_{\max}(U)$, forming the continuous *Bremsstrahlung* spectrum. As the probability of an interaction closer to the target nucleus is lower, the number of produced x-rays decreases linearly with increasing photon energy E_γ

$$N(E_\gamma) \propto E_{\max} - E_\gamma, \tag{1.6}$$

where $N(E_\gamma)$ denotes the photon count of the emanating x-ray radiation. According to Eq. 1.6, the unfiltered *Bremsstrahlung* spectrum in vacuum exhibits a decreasing slope from a high count rate at low photon energies to a minimum number of photons at the maximum energy $E_{\max}$, as visualized in Figure 1.5.

Alternatively, *Bremsstrahlung* occurs due to electron-electron interactions. The interaction with atomic electrons, however, is less likely as it is only linearly proportional to

the atomic number Z. In contrast, interactions with the atomic nucleus exhibit an approximate Z^2 dependency. Hence, at common diagnostic x-ray energies, electron-nucleus interactions are dominant over electron-electron interactions, particularly in high-Z anode material.[29,30]

Characteristic radiation

The second interaction process contributing to the x-ray spectrum is characteristic radiation. It is generated when accelerated incident electrons remove inner shell electrons from the target atom. In an atom, the innermost K shell (principal quantum number $n = 1$) exhibits the highest binding energy. In more peripheral electron shells (L, M, N... shells), corresponding to higher quantum numbers n, the binding energy decreases, see Figure 1.4. In tungsten, a commonly used target material, the binding energies for the K and L shells correspond to binding energies of about $E_{\text{bind,K}} = -69.5\,\text{keV}$ and $E_{\text{bind,L}} = -11.5\,\text{keV}$, respectively.

A highly energetic incident electron can remove an inner shell electron of the atom in the target material. For this process to happen, the kinetic energy E_{kin} of the incident electron must exceed the binding energy E_{bind} of the inner shell electron. The atomic electron escapes from the atomic shell at a kinetic energy E'_{kin} equal to:

$$E'_{\text{kin}} = E_{\text{kin}} - E_{\text{bind}}. \tag{1.7}$$

In case of an interaction with a K shell electron, for example, a kinetic energy of $E_{\text{kin}} > 69.5\,\text{keV}$ of the incident electron is necessary to eject the atomic K shell electron. The ionized atom is energetically unstable. Thus, the electron vacancy in the K shell is readily filled by an electron from a shell of a higher principal quantum number ($n \geq 2$). To preserve the total energy in this process, an x-ray photon is produced that carries the excess energy released by the electron transition. The energy E_γ transferred to the produced x-ray photon is determined by the difference between the binding energy levels E_{bind} (n_1 and n_2) involved:

$$E_\gamma = |E_{\text{bind},n_1} - E_{\text{bind},n_2}| \quad \text{where } n_1 < n_2\,. \tag{1.8}$$

The energy E_γ and the wavelength λ_γ of the emitted x-ray photon is characteristic for the specific electron transition. The transition-specific wavelength is calculated using Eq. 1.4:

$$\lambda_\gamma = \frac{h \cdot c}{E_{\text{bind},n_1} - E_{\text{bind},n_2}}. \tag{1.9}$$

The wavelength characterizing the K transition ($n = 1$) is given by *Moseley's law*:[31]

$$\lambda_\gamma = \frac{h \cdot c}{E_{\text{bind},1} - E_{\text{bind},n_2}} \tag{1.10}$$

$$= \frac{h \cdot c}{13.6\,\text{eV}\,(Z-1)^2\,(1 - 1/n_2^2)}. \tag{1.11}$$

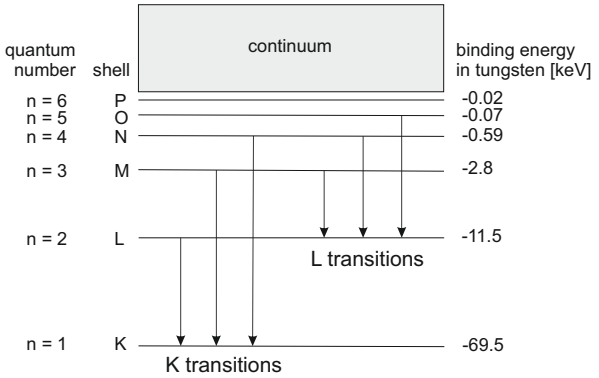

Figure 1.4: Energy levels of tungsten. A simplified scheme showing the discrete energy levels of atomic electrons in tungsten. The electron shells (K, L, M etc.) are associated with the quantum numbers n. Adapted from Oppelt (2005).[18]

It describes the transition from an electron shell with quantum number n_2 to the innermost ($n = 1$) K shell. An electron transition from the L ($n = 2$) to the K shell causes the so-called K_α and a transition from the M ($n = 3$) to the K shell the K_β lines. In tungsten, the K transitions are within the typical range of an x-ray spectrum. These can be further split depending on the orbital and spin quantum number of the ejected electron: $E_\gamma(K_{\alpha_1}) = 59.3\,\text{keV}$, $E_\gamma(K_{\alpha_2}) = 57.9\,\text{keV}$, $E_\gamma(K_{\beta_1}) = 67.2\,\text{keV}$, $E_\gamma(K_{\beta_2}) = 69.1\,\text{keV}$.[32] The photons of the characteristic radiation generate specific lines, e.g., the K lines, in the CT x-ray spectrum, see Figure 1.5.

Typical CT x-ray spectrum

The broad, continuous *Bremsstrahlung* spectrum and the monoenergetic, sharp characteristic radiation compose the CT emission spectrum. A typical CT x-ray spectrum, as shown in Figure 1.5, is characterized by the maximum photon energy $E_{\max}$ occurring for the given tube voltage and the material specific transition lines of the characteristic radiation. Compared to the unfiltered linear *Bremsstrahlung* spectrum, the actual spectrum emitted toward the examination area is different: as indicated in Figure 1.5, low energy photons are largely removed due to inherent absorption (e.g., in the anode material, the tube exit window, or pre-filters). This filtering process is also called beam hardening, as the mean energy of the spectrum is shifted toward harder x-rays corresponding to a higher mean energy. The change of the spectrum is a favorable side effect as the low energy photons would be readily absorbed by the patient. Hence, these photons would only contribute to the patient dose but not to the image data. The processes relevant for the absorption are explained in Section 1.2.2.

An increase in tube voltage U leads to a higher maximum energy $E_{\max}$ of the emitted x-ray photons. Thus, the spectrum is expanded to higher photon energies. In comparison, an increase in tube current J raises the photon count N. Due to a higher tube current, a

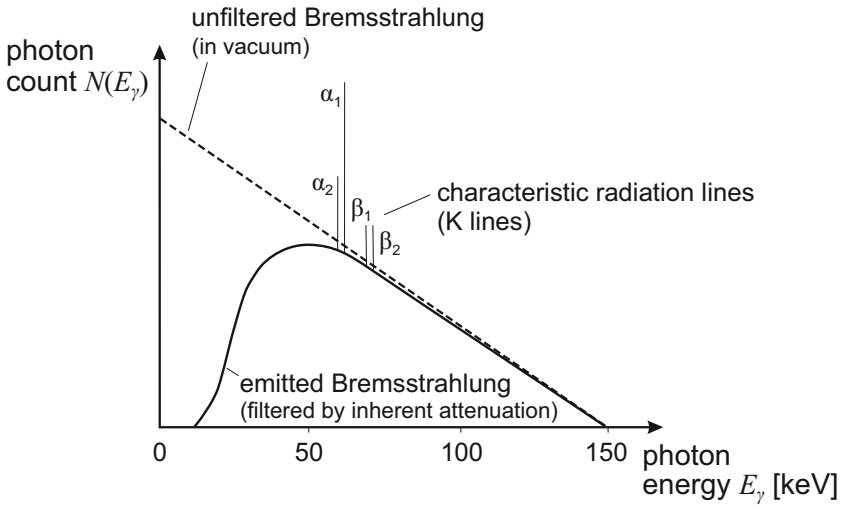

Figure 1.5: Typical CT x-ray emission spectrum at 150 kV tube voltage. The emission spectrum $N(E_\gamma)$ is composed of a broad, continuous *Bremsstrahlung* spectrum with superimposed K-characteristic radiation at discrete photon energies E_γ. In the emitted *Bremsstrahlung* spectrum (solid line), low-energy photons are removed due to inherent attenuation (anode disk, exit window, pre-filters) compared to the unfiltered spectrum in vacuum (dashed line). Adapted from Oppelt (2005).[18]

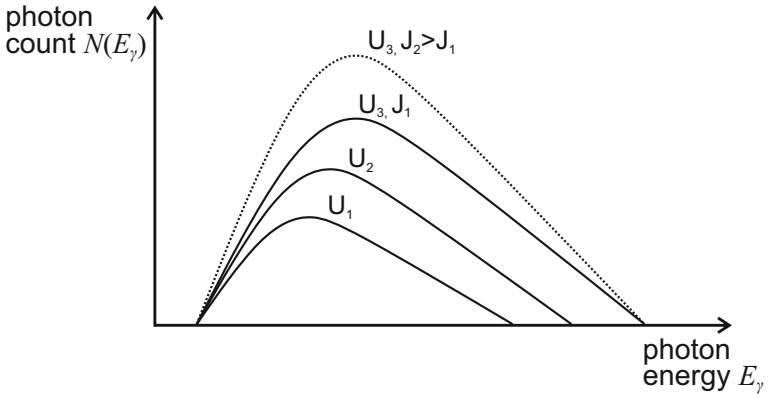

Figure 1.6: Modifications on the *Bremsstrahlung* spectrum. Increasing the tube voltage U ($U_1 < U_2 < U_3$) expands the *Bremsstrahlung* spectrum to higher photon energies E_γ. In comparison, a higher tube current ($J_2 > J_1$) increases the number of photons emitted $N(E_\gamma)$ without change in maximum photon energy (dotted line). Adapted from Schlegel et al. (2018).[21]

greater number of electrons is accelerated toward the anode generating more x-rays. The influence of both parameters affecting the x-ray spectrum is depicted in Figure 1.6.

1.2.2 Photon interactions with matter

Diagnostic x-ray imaging, such as CT imaging, relies on the partial transparency of body tissue to x-ray radiation. Dependent on the tissue type, the penetrating x-ray radiation is attenuated differently on its path through the patient body. The three major interactions of x-rays with matter in the medical imaging energy spectrum – photoelectric absorption, Rayleigh and Compton scattering – are detailed in this section. Pair production is not considered as it is only relevant at photon energies above 1.02 MeV which is far above the typical CT energy range (approx. 25 keV to 150 keV).

The description of the physical processes focuses on the application in x-ray CT imaging. A more comprehensive explanation is given in related text books[18,19,21,30] and in the reviews authored by Seibert and Boone,[24,25] and Hubbell.[26]

Photoelectric absorption

Photoelectric absorption[a] involves an incident x-ray photon and an inner shell electron of the target atom. For this interaction to occur, the binding energy E_{bind} of the atomic electron has to be lower than the energy E_γ of the incident x-ray photon. In the case of an interaction, the photon transfers all its energy to the atomic electron which then is ejected from the electron shell (K, L, M etc. shell), see Figure 1.7(a). While the x-ray photon is absorbed, the kinetic energy E_{kin} of the emitted electron is equal to the difference between the photon energy E_γ and the binding energy E_{bind} of the electron shell:

$$E_{\text{kin}} = E_\gamma - E_{\text{bind}}. \tag{1.12}$$

Immediately after the ejection of the electron, the vacant electron shell is occupied by an electron of an outer shell (lower binding energy). The transition from an outer to the vacant inner shell releases energy equal to the difference in binding energies of the involved electron shells. To preserve the total energy in the system, an x-ray photon can be produced carrying the released energy, see Figure 1.7(a). The energy of the emitted photon $E_{\gamma\prime}$ is characteristic for the electron transition in the atom. Alternatively, the released energy is carried by an Auger electron originating from a peripheral shell.[34] Both effects, the emission of characteristic photons and Auger electrons, usually occur in cascades, initiated by the ejection of the inner shell electron.[35]

If the photon energy E_γ is below the binding energy E_{bind} of a certain electron shell, photoelectric absorption cannot occur. The likelihood of photoelectric absorption, however, is high when the photon energy is equal or a somewhat higher then the binding energy. At these energies the photoelectric absorption suddenly raises and pronounced attenuation

[a] The photoelectric effect was first discovered by Albert Einstein[33] who received the Nobel Prize in Physics for his observation in 1921.

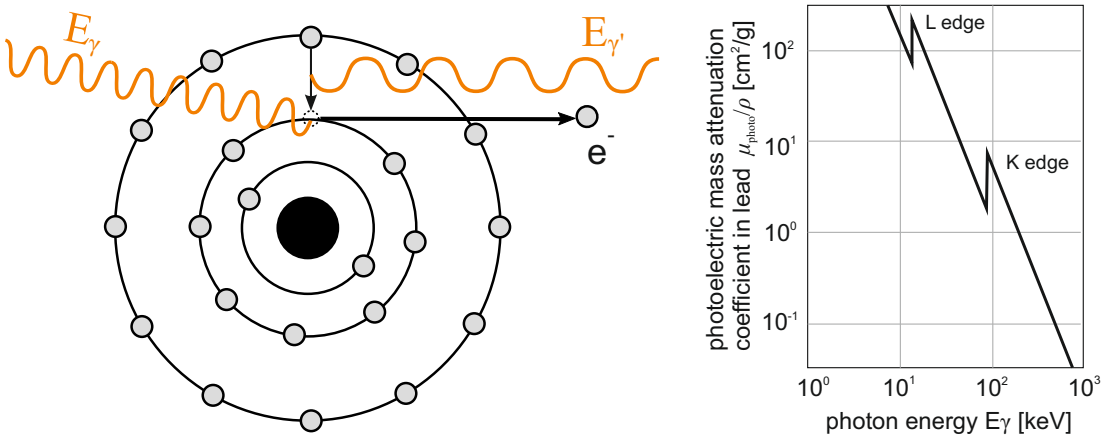

(a) (b)

Figure 1.7: Photoelectric absorption. (a) An impinging photon interacts with an inner shell electron if its energy E_γ is higher than the binding energy of the atomic electron. The photon is absorbed and the electron is emitted from the atom. The vacant electron shell is filled by an electron of a higher shell under the emission of a photon. The energy of the photon $E_{\gamma'}$ is equal to the released energy of the electron transition (difference in binding energies), which is characteristic for the target matter. (b) Photoelectric mass attenuation coefficient in lead (simplified): the probability of photoelectric absorption in matter decreases strongly with the photon energy (Eq. 1.14). It exhibits absorption edges, e.g., the K and L edge, which are characteristic for the target matter. (a) Adapted from Buzug (2008).[19] (b) Redrawn from Krieger (2012).[30]

edges, e.g., the K edge, arise, see Figure 1.7(b). The attenuation edges of a material can be exploited for contrast enhancement. For example, iodine exhibits a K edge in the relevant CT energy range and is commonly used as contrast agent in angiography.

At energies above the (K, L, M etc.) absorption edges, the probability of photoelectric absorption rapidly decreases. The photoelectric attenuation coefficient μ_{photo}, a measure to describe the attenuation due to photoelectric absorption, is approximately proportional to:

$$\mu_{\text{photo}} \propto \rho \frac{Z^4}{A\, E_\gamma^3} \tag{1.13}$$

$$\mu_{\text{photo}} \propto \rho \frac{Z^3}{E_\gamma^3}, \qquad (\text{with } Z/A \approx 1/2) \tag{1.14}$$

where ρ denotes the mass density, Z the atomic number, and A the atomic mass number.[36] In Eq. 1.14 it is assumed that in light atoms the ratio of the atomic number Z and the mass number A is roughly constant ($\frac{Z}{A} \approx \frac{1}{2}$), except for hydrogen.[30] Accordingly, photoelectric absorption is more likely in high-Z material and for low-energy x-rays.

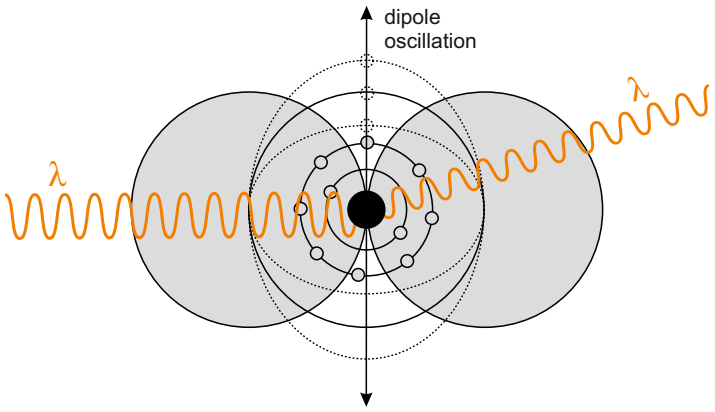

Figure 1.8: Rayleigh scattering (elastic, coherent scattering). Due to the interaction with the electromagnetic field of the incident x-ray photon, the atomic electrons oscillate. A dipole antenna develops from the oscillation that scatters the photon. Although the energies and the wavelengths (λ) of the incident and the scattered photon do not change, their directions differ. Adapted from Buzug (2008).[19]

Rayleigh scattering

The interaction of an x-ray photon and a target atom is described as Rayleigh[b] scattering if the diameter of the scattering particle is small with respect to the wavelength λ of the incident x-ray photon. Although the x-ray photon propagates in a different direction after the interaction, the energy of the photon is unchanged. Thus, Rayleigh scattering is characterized as elastic (or coherent) scattering.

In a classical model, the atomic electrons oscillate due to the interaction with the electromagnetic field of the interacting photon. The dipole antenna developed due to the electron oscillation emits the corresponding radiation, as depicted in Figure 1.8. The attenuation coefficient of Rayleigh scattering μ_{Rayleigh} is approximately proportional to

$$\mu_{\text{Rayleigh}} \propto \rho \frac{Z^{2.5}}{A\,E_\gamma^2}, \tag{1.15}$$

$$\propto \rho \frac{Z^{1.5}}{E_\gamma^2} \qquad (\text{with } Z/A \approx 1/2) \tag{1.16}$$

in the energy range of medical x-ray imaging.[40] Due to the low effective atomic number of human soft tissue ($Z \approx 7.5$), the contribution of Rayleigh scattering to the overall attenuation is only relevant at low photon energies ($E_\gamma \leq 20\,\text{keV}$). In high-Z absorbing matter and at low photon energies, the contribution of Rayleigh scattering to the overall attenuation is below 15 %.[30]

[b]The elastic scattering process of electromagnetic radiation on small particles – later called Rayleigh scattering – was theoretically described by John W. Strutt, 3rd Baron Rayleigh.[37–39]

Compton scattering

In contrast to elastic (coherent) Rayleigh scattering, Compton[c] scattering describes inelastic (incoherent) scattering events where energy is transferred. Hence, an x-ray photon undergoing Compton scattering changes the direction as well as the energy. The target electron is considered as quasi-free due to its low binding energy at an outer electron shell. Compton scattering is feasible if the energy E_γ of the incident photon is much higher than the binding energy of the atomic electron.[42] The collision between the incident photon and the quasi-free electron removes the electron from its electron shell. The remaining energy is transferred to the scattered photon which emanates under a specific deflection angle Θ, see Figure 1.9. In comparison to photoelectric absorption, the photon loses only a fraction of its energy when being Compton scattered. Taking the preservation of energy and momentum into account, the shift in wavelength $\Delta\lambda$ associated with the energy loss is given by:

$$\Delta\lambda = \lambda^{sc} - \lambda \tag{1.17}$$

$$= \frac{h}{m_e\, c}\,(1 - \cos\Theta). \tag{1.18}$$

It describes the relation between the wavelength λ of the incident and the one of the scattered photon λ^{sc}. In this consideration, the interacting photon is treated as a particle-like structure.[41]

The so-called *Klein-Nishina formula*, developed by Oscar Klein and Yoshio Nishina in 1992,[43] describes the interaction of Compton scattering. It reveals the dependency of the associated Compton attenuation coefficient μ_{Compton}, which is approximated as:

$$\mu_{\text{Compton}} \propto \rho\,\frac{Z}{A}\,\frac{1}{E_\gamma^{\chi}}. \tag{1.19}$$

The Compton attenuation coefficient μ_{Compton} is widely independent of the atomic number in light atoms (except hydrogen) as the ratio of the atomic number Z and the mass number A is roughly constant ($\frac{Z}{A} \approx \frac{1}{2}$) in these atoms. Furthermore, a linear dependency on the target mass density ρ is derived. Compton scattering is primarily relevant for low-Z target atoms and high-energy x-ray photons. Within the relevant energy range of diagnostic x-rays, the energy of the photon E_γ has only a minor influence on the probability of Compton scattering, which is approximated by the exponent $\chi \in [0.5, 1.0]$,[30] see Figure 1.10.

While photoelectric absorption is relevant for the object contrast, Compton scattering is an adverse side effect in CT imaging as it impairs the image quality by increasing the image noise. Both effects, however, contribute to the radiation dose of an object. An overview of the main influences on the attenuation coefficient is shown in Figure 1.11.

[c] Arthur H. Compton was rewarded with the Nobel Prize in Physics for discovering the nature of incoherent scattering in 1927.[41]

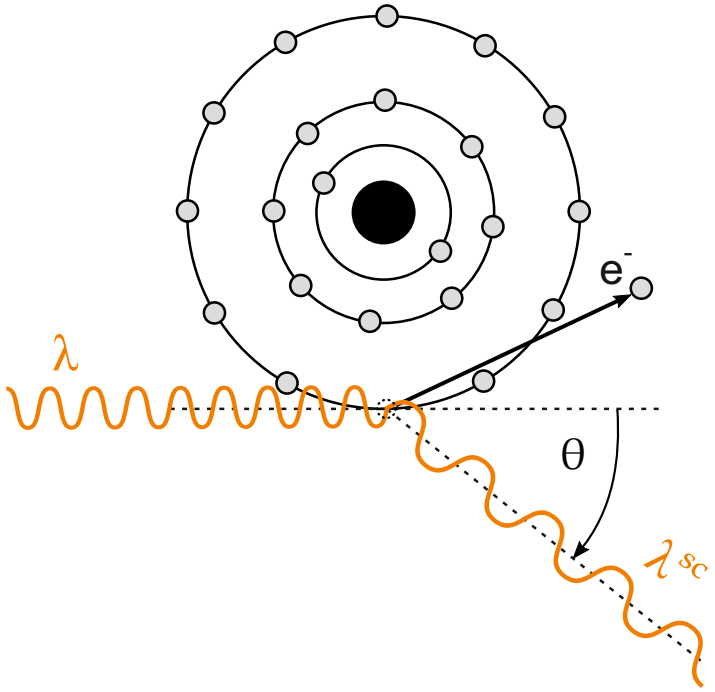

Figure 1.9: Compton scattering (inelastic, incoherent scattering). An incident photon of wavelength λ interacts with a quasi-free electron of an outer atomic shell. Energy is transferred to the electron which is ejected from the atom. The photon loses parts of its energy due to the interaction and emanates under a specific deflection angle Θ. The scattered photon exhibits a longer wavelength λ^{sc} due to the loss in energy (Eq. 1.17). Adapted from Buzug (2008).[19]

Linear attenuation coefficient and Lambert-Beer law

The overall attenuation of an x-ray beam when penetrating an object is approximated by the linear attenuation coefficient μ. It sums up the contributions of the major x-ray interactions with matter and describes how strong the beam is attenuated when penetrating a volume of matter:

$$\mu = \mu_{\text{photo}} + \mu_{\text{Rayleigh}} + \mu_{\text{Compton}} + \mu_{\text{pair}}. \qquad | \ [\mu] = \text{cm}^{-1} \tag{1.20}$$

This approximation of the x-ray beam attenuation is also referred to as the *narrow beam approximation* and is closely related to the mean free path of a photon and the cross-section. Pair production (μ_{pair}) is not further detailed, as photon energies far above the typical CT emission spectrum are required ($E_\gamma \geq 1.022\,\text{MeV}$). A variation of the linear attenuation coefficient is the mass attenuation coefficient μ/ρ ($[\mu/\rho] = \text{cm}^2\text{g}^{-1}$) that describes the ratio of the linear attenuation coefficient μ and the mass density ρ of the target material. Due to the normalization by the mass density, the mass attenuation coefficient is commonly preferred to compare the attenuation properties of different materials. The contributions of the single photon interaction processes – photoelectric absorption, Rayleigh scattering, Compton scattering, and pair production – to the mass attenuation coefficient in water are depicted in Figure 1.10.

Generally, the linear attenuation coefficient depends on the photon energy E_γ, the atomic number Z, and the mass density ρ, compare Figure 1.11. Assuming a homogeneous object and a monoenergetic x-ray beam, the linear attenuation coefficient simplifies $\mu(E_\gamma, Z, \rho) \rightarrow \mu$.

Using the linear attenuation coefficient μ, one can determine the number of photons dN that interact with the matter of an infinitesimally thin slice. The reduction in photon number dN is proportional to the attenuation coefficient μ, the number of photons N, and the path through the slice dx:

$$dN = -\mu\, N\, dx. \tag{1.21}$$

The *Lambert-Beer law* – a fundamental relation in x-ray physics – is obtained by integration of Eq. 1.21:

$$\int_{N_0}^{N(x')} \frac{1}{N}\, dN = -\int_0^{x'} \mu\, dx \tag{1.22}$$

$$\Rightarrow N(x') = N_0\, e^{-\mu\, x'}, \tag{1.23}$$

where N_0 is the number of incident photons and $N(x')$ is the number of remaining photons after propagating through an object of thickness x'. This relation results from the observations by Pierre Bouguer,[44] Johann H. Lambert,[45] and August Beer[46] and assumes the *narrow beam approximation* (Eq. 1.20).

In a heterogeneous object, where the local mass density ρ changes depending on the location in the object, $\rho \rightarrow \rho(x)$, the linear attenuation coefficient becomes locally dependent as well, $\mu \rightarrow \mu(x)$. The spatial dependent formulation of the *Lambert-Beer law*, an extension of Eq. 1.23, results in:

$$N(x') = N_0\, e^{-\int_0^{x'} \mu(x)\, dx}. \tag{1.24}$$

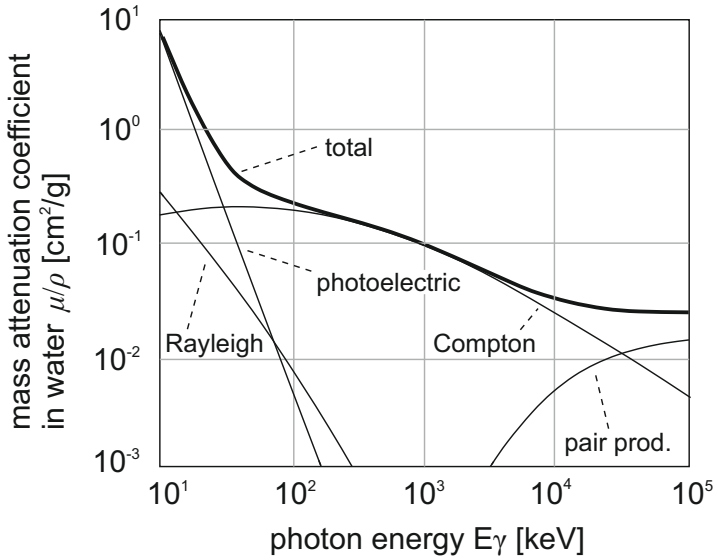

Figure 1.10: The (total) mass attenuation coefficient μ/ρ is composed of contributions from photoelectric absorption (μ_{photo}), Rayleigh scattering (μ_{Rayleigh}), Compton scattering (μ_{Compton}), and pair production (μ_{pair}). The relations are shown for the attenuation in water. The diagnostic energy range is approximately $E_\gamma \in [25\,\text{keV}, 150\,\text{keV}]$. Adapted from Oppelt (2005).[18]

It determines the photon number $N(x')$ at a depth x' in a heterogeneous object. Commonly, polychromatic x-ray radiation is used in medical x-ray imaging systems. Hence, the linear attenuation coefficient further depends on the photon energy of the emitted x-ray beam such that $\mu \to \mu(x, E_\gamma)$. The energy and spatial dependent version of the *Lambert-Beer law* is obtained by the integration over the employed photon energies $E_\gamma \in [0\,\text{keV}, E_{\max}]$:

$$N(x') = \int_0^{E_{\max}} N_0(E)\, e^{-\int_0^{x'} \mu(x,E_\gamma)\,dx}\, dE. \tag{1.25}$$

In CT systems, N_0 corresponds to the emitted photon number and $N(x')$ to the photon number measured at a detector behind the object. These attenuation data are used for the image reconstruction process, see Section 1.2.3, in order to obtain an image of the object's cross-section.

1.2.3 Basic principles of CT imaging

This section gives an overview about the basics of diagnostic imaging with CT systems. It starts with a summary of the milestones in the CT development, followed by a description of the major components of a modern CT system. The section closes with a brief explanation on how CT data are acquired and processed in order to provide diagnostic CT images.

This overview preliminary focuses on aspects that are relevant for the context of this thesis. Further background on these aspects is given by related text books[18–21,48,49] which forms the basis of this section.

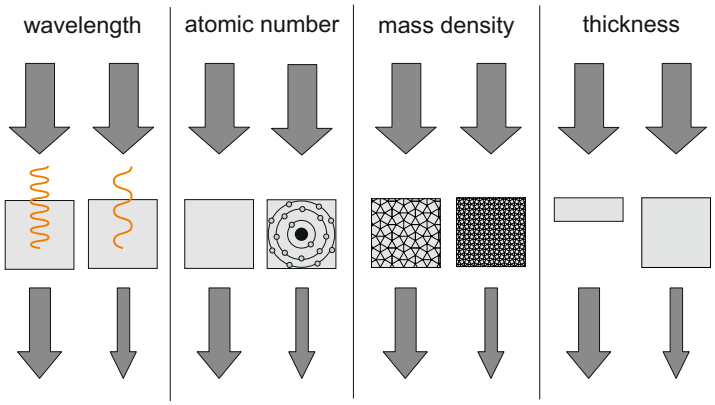

Figure 1.11: Factors influencing the attenuation of an x-ray beam. Besides the wavelength λ (inversely related to the photon energy E_γ) of the incident photons, the atomic number Z, the mass density ρ, and the thickness dx of the target material affect the attenuation of the penetrating x-ray beam. The width of an arrow indicates the intensity of the in- and outgoing x-ray beams. Adapted from Laubenberger and Laubenberger (1999).[47]

Historical development of CT systems

Wilhelm C. Röntgen discovered x-rays by accident during experiments on cathode rays in gases. On November 8, 1895 he observed that a fluorescence screen nearby his experimental setup began to glow when operating the cathode-ray tube. After weeks of intensive research, he submitted his observations "On a new kind of rays" for publication.[50] Shortly afterwards, the discovered radiation was already used for medical purposes. First, x-rays were used for conventional x-ray imaging – also denoted as projectional radiography. The images obtained from projectional radiography show the superimposition of anatomic structures located at different depths.

However, the leap to CT imaging required fundamental contributions from mathematics and advances in computer technology before the first CT scan in 1972 was performed. A major contribution was provided by Johann Radon in 1917. He proved that one can reconstruct the spatial distribution of a material feature if the line integrals through the corresponding object plane are known.[51] In 1963, Allan M. Cormack presented a method to determine the spatial distribution of the x-ray attenuation in human tissue based on transmission measurements.[52,53] Likewise, William H. Oldendorf contributed to the maturation of CT systems.[54] Finally in 1972, Godfrey N. Hounsfield[d] translated the theory into practice and realized the first CT system.[55] Neither Allan M. Cormack nor Godfrey N. Hounsfield knew about the previous works and developed the reconstruction methods independently[e]. The term "computed tomography" addresses the fact that a computer-based

[d]Godfrey N. Hounsfield built the first of the CT system at the laboratories of his employer, EMI Records Ltd., which was a British company and a well-known record label (e.g., The Beatles). In the beginning of CT imaging, the imaging systems commonly were denoted as "EMI scanners".

[e]In 1979, Allan M. Cormack and Godfrey N. Hounsfield were recognized the Nobel Prize in Physiology or Medicine for their achievements in the CT development.

technology allows to "write" (Greek for *graphein*) "slices" (Greek for *tome*) of an object.

Over the decades, CT systems steadily improved. Major breakthroughs, for example, represent whole-body imaging enabled by the fan beam geometry (1970s), shorter acquisition times by slip ring technology (1980s), spiral CT[56,57] (1990s), multi-row detectors[58] and dual-source systems[59] (2000s). Ongoing and future aims in CT imaging are, e.g., low-kilovolt imaging, multi-energy and photon counting capabilities, and – what is addressed in this thesis – reductions in patient dose as well as personalized imaging.[9–11,60,61] A comprehensive view on the future of CT imaging is provided to the interested reader in the reviews by Alkadhi and Euler (2020)[11] and by Lell and Kachelrieß (2020).[10]

This historical introduction is mainly based on publications by Kalender (2006)[23] and Dirnberger et al. (2020),[62] which offer an interesting historical review on the development of CT imaging.

Components of a CT system

In modern clinical CT systems, the so-called 3$^{\text{rd}}$ generation geometry is established, see Figure 1.12. Descriptions of the 1$^{\text{st}}$, 2$^{\text{nd}}$, and 4$^{\text{th}}$ generation geometries can be found in the mentioned text books. The characteristic of the 3$^{\text{rd}}$ generation geometry is that the two core components – the x-ray tube and the detector – are both mounted on a CT gantry that rotates around the patient. The patient is located at the isocenter of the CT system, which defines the geometrical center of the CT gantry rotation. The patient's longitudinal axis and the rotation axis of the CT gantry are aligned parallel to the z axis of the CT system. The x-ray fan beam is emitted from the x-ray tube and covers fan beam angles in the range of approximately $\beta \in [-25°, 25°]$. The detector, mounted on the opposite side, is composed of about 700 to 900 detector channels (also: detector elements). The field of view (FOV), the region where the x-ray attenuation of a projection is measured, is about 50 cm. Thus, a usual patient cross-section is covered by the FOV of a fan beam at a single tube position α (note: this is not feasible with 1$^{\text{st}}$ and 2$^{\text{nd}}$ generation CT geometries). The CT patient table (also: patient couch) carries the patient under examination and moves it into the circular opening of a CT system for imaging. Most CT systems allow to adjust the patient table height (vertical movement) and the movement along the system's z axis, but no lateral adjustment.

During the rotation about the patient, the CT gantry acquires about 1000 projections (also: readings) at different tube positions α. A rotation typically lasts between 1/4 s and 1 s, resulting in high centripetal forces. Accordingly, mechanically demanding accelerations of 40 g and above occur at, e.g., the position of the x-ray tube.[9,22] The rotating gantry is connected to the stationary part of the CT system by slip rings for, e.g., power supply. Parts of the data are transmitted wireless.

CT detectors commonly comprise several detector rows – so-called multi-row or multi-slice detectors. The extent in z direction allows for a larger volumetric coverage. Modern CT detectors feature an isotropic spatial resolution corresponding to less than 0.5 mm at the CT isocenter (note: the size of the detector elements on the detector arc is larger according to the intercept theorem). An anti-scatter grid (ASG) is a fine structure of highly x-ray

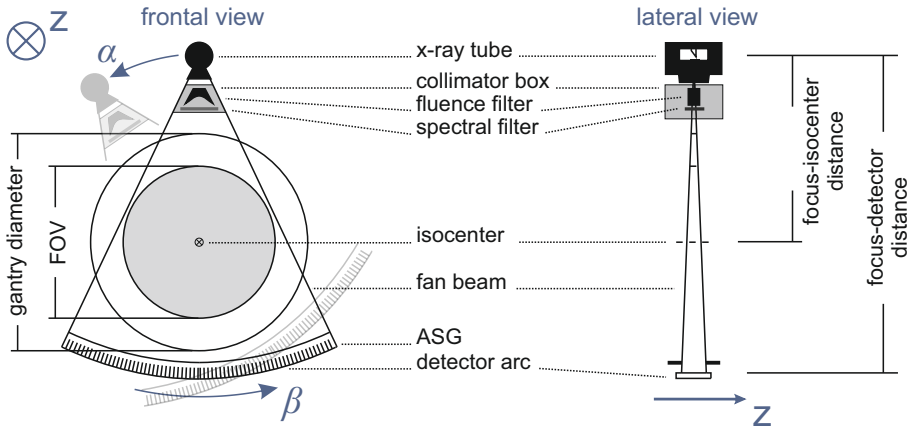

Figure 1.12: CT setup and components. A CT system based on the 3rd generation geometry in the fan beam plane (left: frontal view) and along the z axis (right: lateral view). The components depicted are mounted on a CT gantry that rotates around the CT isocenter about an axis parallel to the z axis. The angle β denotes the fan beam angle and the angle α the projection angle of the current tube position. Adapted from Kalender (2011).[20]

absorbing blades attached on the CT detector. The blades are focused toward the focal spot in order to filter scatter radiation before it impinges on the detector. The collimator box is attached on the x-ray tube housing. It comprises collimators to limit the extend of the fan beam in β and in z direction. Furthermore, spectral filters are employed to design the x-ray emission spectrum, see Figure 1.5. For example, thin sheets of aluminum or copper filter low-energy photons to reduce the patient radiation dose, see Section 1.3.1. A CT component that is central in this thesis is the x-ray fluence filter. Due to its shape, it is usually referred to as "bowtie filter" and is also integrated in the collimator box. As the typical patient cross-section is roughly elliptically shaped, the x-ray attenuation is high for central rays and comparably low for rays penetrating the patient at the periphery. A static bowtie filter aims at achieving equal noise within one projection and avoiding unnecessary radiation dose. To compensate for the varying attenuation, the thickness of the static bowtie filter increases toward the edges corresponding to more peripheral fan beam angles β. A picture of a static bowtie filter is shown in Figure 1.13. The transmission profile obtained from a static bowtie filter is pre-defined by its shape and material. Static bowtie filters as a measure for dose reduction are discussed more comprehensively in Section 1.3.

Image data acquisition and image reconstruction in CT

In CT imaging, the local attenuation, represented by the linear attenuation coefficients μ, determines the pixel values in the reconstructed image of the investigated object.

Sinogram In rotating CT systems, the remaining photon count after passing the patient is measured from different directions. Therefore, the attenuation of a ray along the

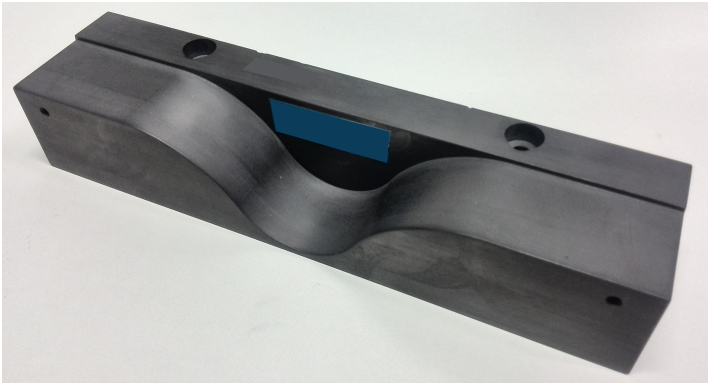

Figure 1.13: A static bowtie filter for x-ray fluence filtration. It is installed in the fan beam path inside the collimator box, see Figure 1.12. Depending on the fan beam angle β, the rays of the fan beam are attenuated when penetrating the wave-shaped solid. Central rays are hardly attenuated while the x-ray attenuation increases toward larger fan beam angles at the periphery. The transmission profile resulting from a static bowtie filter is pre-defined by its shape and material composition (e.g., aluminum). The straight part at the rear end (with two holes) is for the mounting.

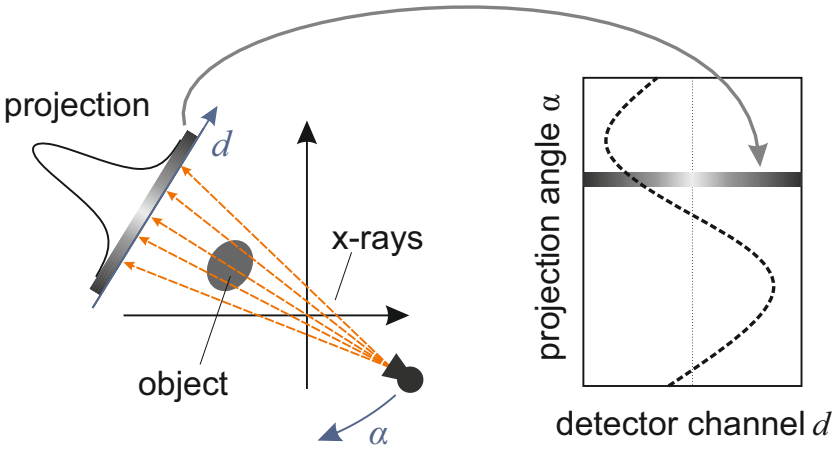

Figure 1.14: Composition of a sinogram. The attenuation of an object at a specific tube position α is projected onto the detector elements d (left). The continuous record of the attenuation at different projection angles α composes the sinogram (right). An item that is located off-center w.r.t the CT isocenter shows a sinosoidal curve in the sinogram (dashed line). Adapted from Hsieh (2009).[48]

path $\boldsymbol{r}(\alpha, d)$, described by the straight line from the focus at projection angle α through the patient to the detector element d, determines the line integral $p(\alpha, d)$. It relates the photon count detected behind the patient N to the initial photon count N_0. During the acquisition, the gantry rotates such that the line integrals are measured from multiple projections angles α. The calculation of a line integral p results from the *Lambert-Beer law* (Eq. 1.23). It is given by

$$p(\alpha, d) = -\ln \frac{N(\alpha, d)}{N_0(\alpha, d)} \tag{1.26}$$

$$= \int_{\alpha,d} \mu(\boldsymbol{r})\, d\boldsymbol{r}, \tag{1.27}$$

which equals the integral over the linear attenuation coefficient $\mu(\boldsymbol{r})$ along the path $\boldsymbol{r}$ of a ray specified by its projection angle α and detector element d. The resulting matrix of line integrals $p(\alpha, d)$ is commonly denoted as sinogram. The composition of the sinogram is indicated in Figure 1.14.

Image reconstruction Knowing the line integrals composing the sinogram (Radon space), the solution of the inverse problem in Eq. 1.26 reveals the local attenuation coefficients to build the reconstructed image (image space). A common method to solve the inverse problem is filtered backprojection (FBP). It aims to reverse the Radon transformation: the measured line integrals p are first convoluted with a high-pass filter (for increased edge definition) and then backprojected to the image space, see Figure 1.15. The FBP returns the requested distribution of the linear attenuation coefficient $\mu(\boldsymbol{x})$ in the investigated slice of the patient. The choice of the convolution kernel influences the sharpness and the noise properties of the image and is selected according to the clinical task.

In projectional radiography, the image shows a superimposition of all structures along the path of a ray. Thus, highly attenuating structures dominate the detector signal and suppress minor contributions of soft tissue. In comparison, the sinogram employed in CT imaging represents the local attenuation in the object without superimposition. As a consequence, the image reconstruction resulting from the CT acquisition allows to reproduce also small variations in adjacent voxels to provide enhanced soft tissue contrast.

HU scale The image reconstruction delivers an image of the patient cross-section, where the pixel values are based on the local linear attenuation coefficients. In the next step, the linear attenuation coefficients μ are transferred into Hounsfield units (HU) returning the CT values:

$$\text{CT value } = 1000 \cdot \frac{\mu - \mu_{\mathrm{H_2O}}}{\mu_{\mathrm{H_2O}}}. \qquad | \ [\text{CT value}] = \text{HU} \tag{1.28}$$

The linear attenuation coefficient of water is $\mu_{\mathrm{H_2O}} \approx 0.192\,\mathrm{cm}^{-1}$. The resulting CT image shows the investigated slice of the patient on a gray scale where water is normalized to 0 HU (independent of the x-ray emission spectrum). Air corresponds to -1000 HU and bony tissue reaches 2000 HU and above. A selection of CT values in HU of different tissue is shown in Figure 1.16.

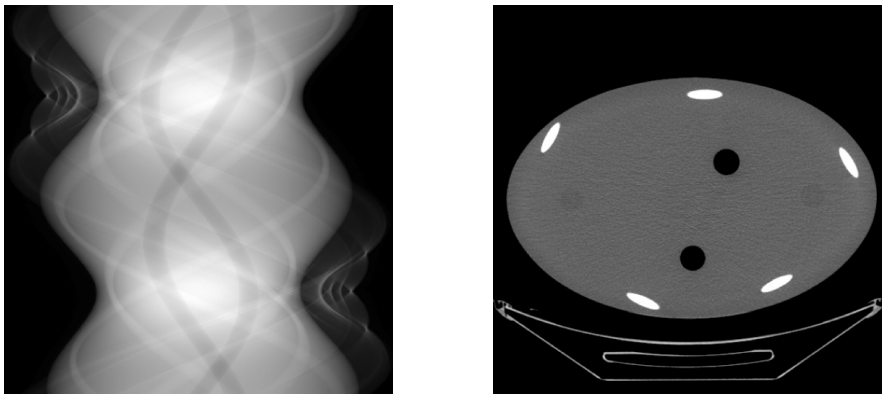

Figure 1.15: Object data in the Radon (sinogram) space and the image space. Using reconstruction methods, such as FBP, the object data composing the sinogram (left) are transformed into a reconstructed image of the examined object (right). Taken from Hsieh (2009).[48]

Windowing The typical HU scale ranges from $-1024\,\mathrm{HU}$ to $3071\,\mathrm{HU}$. The human eye can distinguish only a limited number (< 100) of gray levels and is therefore not able to resolve the gray levels of the entire range ($2^{12} = 4096$) simultaneously. Therefore, only a smaller HU range is selected that is resolved on the monitor. CT values above or below the specified range are shown in white or black, respectively. The choice of the HU range resolved is denoted as windowing and is characterized by a window center and a window width.

1.2.4 Image quality

This section provides an overview of possible metrics to assess the image quality in an image that is independent of the observer. Furthermore, typical image artifacts arising in CT images are presented. Related literature gives further insights in image quality aspects and builds the basis of this section.[19,21,49]

Influencing parameters

A pixel of a CT image depicts the local x-ray attenuation in HU in relation to the attenuation in water. The image quality of a CT image is closely related to radiation dose. Thus, it is generally recommended to compare image quality only at equal dose levels or vice versa. There are several parameters that influence image quality: for example, the tube voltage U, the tube current J, or the acquisition time affect the image quality but also the dose. Furthermore, the selection of the convolution kernel (Section 1.2.3), the slice thickness, and the reconstruction algorithm have an impact on the image quality. A detailed explanation on these parameters can be found, e.g., in Schlegel et al. (2018)[21] or in Buzug (2008).[19]

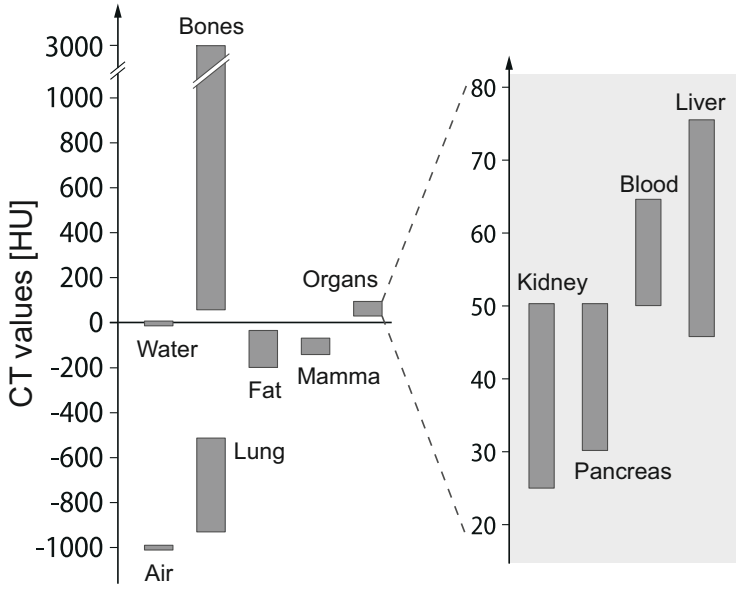

Figure 1.16: HU scale and HU values of exemplary tissue. Depending on the local attenuation, HU values are assigned to the pixels in a reconstructed CT image. The resulting image shows the HU values in gray values that obey the HU scale, as given in Eq. 1.28. The scaling uses water as reference (μ_{H_2O}: 0 HU). A stronger attenuation (higher mass density) corresponds to higher HU values, which is represented by brighter gray values. The typical range of HU values is shown for some exemplary tissue types and some organs. Air corresponds to −1000 HU and bony tissue reaches 2000 HU and above. The CT values of some organs are similar and may overlap. Adapted from Alkadhi et al. (2011).[49]

Image quality metrics

A commonly used metric to quantitatively assess the image quality is image noise. The image noise σ is Poisson distributed such that the expectation value of the detected photon count N equals the variation σ^2 of the photon count: $\langle N \rangle = \sigma^2(N)$. The image variance is inversely proportional to the number of detected photons. A higher image quality (in terms of image noise) is obtained at the expense of an increase in x-ray photons, which raises the patient radiation dose D, though. The Brooks' relation[63] summarizes the dependencies of the noise level (reformulated by Nagel[64]):

$$\sigma^2 \propto \frac{e^{-\mu\, x}}{D}, \qquad (D \propto N) \tag{1.29}$$

where $e^{-\mu\, x}$ describes the attenuation of the x-ray beam at depth x in an object with linear attenuation coefficient μ and D denotes the radiation dose (see Section 1.2.5), which is proportional to the number of photons N. In realistic CT images, however, the image noise comprises additional contributions from quantum noise, electronic noise, and projection data, which are not captured by the Brooks' relation. Therefore, it should be considered only as an approximation of the dependencies.

A more comprehensive characterization of noise is obtained by the noise power spectrum (NPS) that considers the correlation of noise between neighboring pixels. Besides the level of noise, also its texture is evaluated. The NPS is the Fourier transform of the auto-covariance function. A mathematical derivation is provided in different literature.[22,65,66]

Another property to assess image quality is the image contrast. It describes the difference in pixel intensities (i.e., HU) between different pixels i (e.g., the brightest and the darkest pixel in an image). The contrast C can be calculated as

$$\mathrm{C} = \frac{\mathrm{HU}_1 - \mathrm{HU}_2}{\mathrm{HU}_1}, \tag{1.30}$$

which does not depend on the photon count. More commonly, however, the contrast-to-noise ratio (CNR) is preferred that relates the contrast to the noise level σ:

$$\mathrm{CNR} = \frac{\mathrm{HU}_1 - \mathrm{HU}_2}{\sigma}. \tag{1.31}$$

The signal-to-noise ratio (SNR) relates the detected photon count N to the noise level σ:

$$\mathrm{SNR} = \frac{N}{\sigma}. \tag{1.32}$$

For Poisson distributed signals, such as the photon distribution in CT acquisition, the SNR obeys:

$$\mathrm{SNR} = \frac{N}{\sqrt{N}} = \sqrt{N}. \tag{1.33}$$

There are additional measures for evaluating image quality, especially the spatial resolution. For a more comprehensive description, the reader is referred to relevant text books.[19,21,22,49,67]

Artifacts in CT images

The discrepancy between the attenuation represented by the image reconstruction and the actual attenuation in the object is denoted as image artifact. The image artifacts have different origins, e.g., due to the reconstruction method or patient movement. Relevant in this thesis, however, are image artifacts due to physical processes and the CT system.

Beam hardening artifacts A CT emission spectrum consists of photons of different energies, see Figure 1.5. Low-energy photons are more likely to be absorbed by the investigated object than high-energy photons, as elaborated in Section 1.2.2. As a consequence of the energy dependent absorption, the mean energy of an x-ray beam shifts toward higher energies – denoted as harder x-rays – the further the beam propagates through the object. Hence, a volume element at the inside of an object shows a lower attenuation than a volume element of the same attenuation closer to the surface. In an uniform object, the HU values are lower (darker) inside the object than at the edges, if this is not taken into account by an appropriate correction. Due to the appearance in a homogeneous cylindrical object – dark in the center, bright at the edges – this artifact is also called "cupping artifact".

Photon starvation artifacts A strong x-ray attenuation at some parts of the fan beam causes the number of photons impinging on the corresponding detector elements to be small. For example, the shoulders drastically lower the photon count in lateral projections of upper torso acquisitions. The low data fidelity entails streaky artifacts with increased noise at the corresponding regions in the reconstructed image.

Ring artifacts A miscalibration of, e.g., the x-ray tube output, the gain of detector elements, or the unintended displacement of a pre-filter, potentially causes ring artifacts in the reconstructed image. The latter case, an accidental displacement of an x-ray fluence filter is an issue considered in this thesis. As the error is constant across the rotation, a ring appears in the reconstructed image where the HU values deviate from the actual object attenuation. The center of the ring coincides with the isocenter of the CT system. A precise calibration and a reliable operation of the CT components involved are required to avoid such ring artifacts.

Scatter radiation artifacts Due to the photon interactions, a considerable fraction of the primary photons is scattered when penetrating the investigated object. This is particularly crucial when employing multi-row detectors or dual-source CT systems.[68] The secondary photons can escape the object under a scatter angle that deviates from the initial direction of the primary photon. Thus, a scattered photon that reaches the detector biases the photon count in the detector element. Due to the excess photon count, the measured photon count does no longer correlate with the physical properties of the investigated object and underestimates the object attenuation. The appearance in the reconstructed image can be similar to that of beam hardening artifacts.[69] To account for scatter radiation artifacts, ASGs are employed to filter scattered photons before they impinge on the detector surface, see Figure 1.12.

1.2.5 Radiation dose and biological effects

This section introduces the major quantities to asses and compare radiation exposures and their biological effects. Additional information on this topic is available in related literature, which serves as the basis of this section.[2,21,49]

In CT imaging, the energy deposition of ionizing x-ray radiation is of stochastic nature. Thus, the occurrence of radiation induced damages, such as cell mutation, is a statistical risk[f]. In the range of low radiation doses, meaning below 100 mSv according to the International Commission on Radiological Protection (ICRP),[70] the linear-no-threshold (LNT) model is applied. Radiation doses by CT imaging are approximately 100 times lower than this limit and thus within the LNT energy range. The LNT model hypothesizes a linear relation between the imparted dose and the biological effect without any threshold. Thus, the risk of a radiation damage linearly increases with rising radiation dose.

The fundamental quantity to describe radiation dose is the absorbed dose D. It relates the energy E absorbed by an object to its mass m:

$$D = \frac{E}{m}. \qquad | \; [D] = \mathrm{J/kg} = \mathrm{Gy\ (Gray^g)} \tag{1.34}$$

In cases where the object is composed of a single homogeneous organ or tissue T, the absorbed dose D equals the mean absorbed dose D_T.

The biological effect resulting from a radiation exposure differs depending on what type of radiation R is applied (at equal absorbed dose). Thus, the equivalent dose H is determined based on the absorbed dose. It accounts for the variations between different kinds of radiation by an additional weighting factor w_R. The equivalent dose $H_\mathrm{T,R}$ for a specific organ or tissue T obeys

$$H_\mathrm{T,R} = w_\mathrm{R}\, D_\mathrm{T,R}, \qquad | \; [H] = \mathrm{J/kg} = \mathrm{Sv\ (Sievert^h)} \tag{1.35}$$

with the mean absorbed dose $D_\mathrm{T,R}$ in the organ or tissue T by the radiation type R. The radiation weighting factor w_R is a dimensionless parameter that is $w_\mathrm{R} = 1$ for x-ray radiation.

Different organs and tissues exhibit an individual sensitivity to radiation. To account for these tissue-specific variations, the tissue weighting factor w_T is introduced to calculate the effective dose. The accumulated and weighted equivalent doses in all tissues or organs T exposed to the radiation R return the effective dose δ:

$$\delta = \sum_\mathrm{T} w_\mathrm{T}\, H_\mathrm{T,R}\,. \qquad | \; [\delta] = \mathrm{J/kg} = \mathrm{Sv\ (Sievert)} \tag{1.36}$$

[f] In comparison, typical radiation doses in radiotherapy or severe radiation accidents are rather deterministic effects, which can entail cell death (apoptosis) and single or double strand-breaks of the deoxyribonucleic acid (DNA).

[g] Luis H. Gray was a British physicist. He introduced the unit for radiation dose *rad* (*r*adiation *a*bsorbed *d*ose). To credit his efforts in radiation dose research the unit *rad* was later replaced by the SI unit *Gray* (Gy) named after him.

[h] Rolf M. Sievert was a Swedish medical physicist. He was honored with the SI unit *Sievert* (Sv) for his contributions on biological effects of ionizing radiation.

The dimensionless tissue weighting factors ($\sum_T w_T$=1) are proposed by the ICRP and reflect the radio-sensitivity and the size of a tissue or organ in relation to the entire body. The values are average values for male and female patients of different ages.[70] The tissue weighting factors w_T used in this work are summarized in Table 3.2.

The effective dose estimates the stochastic risk of a radiation-induced health detriment.[71] It represents the corresponding whole-body dose that would entail the same statistical health risk as that due to the partial body examination.[72,73] The effective dose is a suitable measure to compare the radiation burden of an x-ray exposure between different CT technologies, as conducted in this work.[73,74]

1.3 Dose reduction strategies

The clinical application fields of CT are expanding and the number of CT examinations is continuously increasing, see Figure 1.1. In view of the fact that CT examinations account for almost half of the overall radiation dose of medical origin, care should be exercised when preparing a CT examination. Radiological guidelines[75,76] demand that the benefit from an x-ray based examination must exceed the estimated potential risk of a radiation exposure. The ALARA principle, see Section 1.1, is a well-known established guideline. It requires keeping the dose as low as reasonably possible to accomplish the diagnostic objective. Notwithstanding the criteria to decide whether a CT examination is justified, this section focuses on measures – particularly technical innovations – to reduce the radiation burden for the examined patient. A more comprehensive overview on dose reduction techniques is provided in related literature.[7,19,49,73,77]

1.3.1 General technical approaches

Over the decades, different approaches have been implemented to improve patient radiation protection. A selection of major techniques is explained in this section.

Spectral filter Due to the photon interactions with matter (Section 1.2.2), low-energy photons are likely to be absorbed in the patient. Hence, these photons raise the patient dose without contributing to the image. To account for that, collimator boxes accommodate spectral filters (Figure 1.12) that filter low-energy photons before they emanate toward the examination area. In addition, beam hardening artifacts (Section 1.2.4) are mitigated. Spectral filters are commonly implemented as thin blades made of, e.g., aluminum, tin, or copper.

Overscanning In spiral CT with multi-row detectors, the irradiated volume exceeds the desired reconstruction volume in z direction in order to provide sufficient projection data. The excess exposure, however, can be reduced by dynamic z collimators. A pair of x-ray absorbing blades dynamically adjusts the collimation in z direction to effectively block unnecessary parts of the x-ray beam.[78,79]

Tube voltage selection If exercised carefully, the selection of a lower tube voltage can reduce the radiation burden for the patient in a CT examination. However, the effect of a tube voltage reduction on the image noise and tissue contrast is complex, as a lower tube voltage improves the image contrast but in turn impairs the patient dose. Its impact strongly depends on the patient size.[80–82] Yet, a tube voltage reduction can be meaningful for small-size patients and in the case of angiography using iodine. The attenuation of iodine (K edge at 33 keV) is higher at lower tube voltages, which improves the image contrast and the visibility of pathological features.[83]

Tube current modulation (TCM) Another patient- and task-specific measure to reduce the patient radiation dose is the adaptation of the tube current.[84] The attenuation of the x-ray beam by the patient can vary considerably between the different projections and body regions. Variations over two orders of magnitude and more are realistic.[85] Unless properly compensated, the reconstructed image suffers from anisotropic noise (noise texture). Theoretical considerations show that the pixel noise is dominated by the noise contributions of highly attenuated (noisy) projections, as indicated in Figure 1.17.[85,86] This implies that a low tube current is sufficient at low-attenuation projections without negatively affecting the final pixel noise substantially.[87–90] There are different methods to determine the tube current applied. The attenuation-based concept uses localizer radiographs (also called CT topograms), which are obtained in anterior/posterior (a/p) and in lateral projections to provide information about the patient attenuation.[87,88,91] Alternatively, the tube current is modulated in real-time by a feedback loop. Using the detector data of the current projection, the tube current of the subsequent projections is chosen. Both methods allow to adapt the tube current depending on the angular (α) as well as the longitudinal (z) position of the x-ray tube. In addition, TCM is exploited to protect x-ray sensitive organs. For example, breast tissue is protected by reducing the tube current at anterior projections, which is compensated by a higher tube current at posterior projections, as reported in e.g., Huck et al. (2021)[92] and other related studies.[93,94]

Bowtie filter The cross-section of a patient can be approximated by an ellipse. Consequently, the x-ray attenuation by the patient is lower for peripheral than for central rays. If this is not taken into account, image artifacts, particularly radial streaks toward the patient edges, can arise (Figure 1.17). So-called bowtie filters aim to compensate for the patient attenuation by pre-attenuating peripheral rays of the x-ray beam. Accordingly, bowtie filters are designed to minimize the path length through the bowtie filter in the center and increase the path length toward the periphery, see Section 1.2.3 and Figure 1.13. Prefiltration by a bowtie filter lowers the patient radiation dose (particularly the surface dose) and distributes the image noise more isotropically.[96–98] Nevertheless, the pre-filtration by a static bowtie filter is a compromise between different imaging situations, as elaborated in the subsequent Section 1.3.2. The transmission profile produced by a bowtie filter is predefined by its shape and its material composition and therefore cannot be adapted to the individual imaging situation. This is a central aspect in this thesis, which – among other topics – explores the benefits from dynamic x-ray fluence filters on the dose efficiency. In addition to the dose reduction measure, bowtie filters mitigate beam hardening artifacts

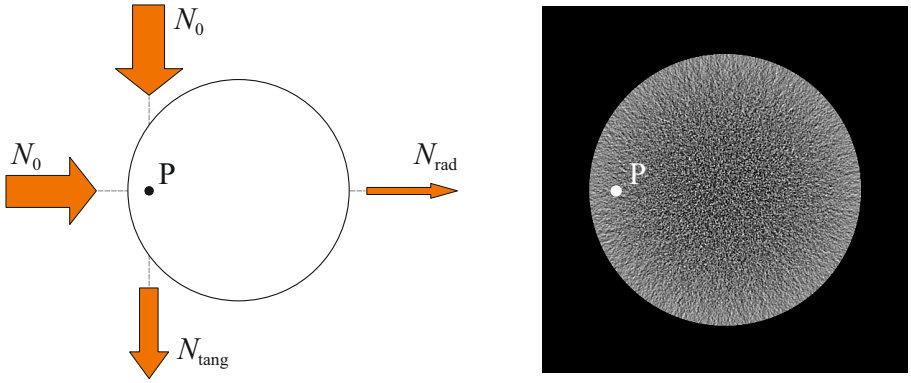

Figure 1.17: Origin of noise texture. For the same incident x-ray fluence N_0, the ray along the radial direction is much stronger attenuated than the tangential ray, which crosses a shorter path through the cylindrical object. Thus, the remaining x-ray fluence behind the object is smaller in the radial than in the tangential direction: $N_{rad} < N_{tang}$. The width of the arrows indicates the intensity of the x-ray fluence (left). At a peripheral sample point P, the noise is anisotropic and exhibits radial streaks due to the dominance of the noise contributions along the high-attenuation radial directions (right).[85,86] Adapted from Hanson (1980).[95]

by reducing the variations in x-ray energies between central and peripheral rays impinging on the CT detector.[99,100]

Apart from these major technical implementations for radiation dose reduction, there are additional measures dedicated to specific imaging scenarios such as pediatric, cardiac, or dual energy computed tomography. These considerations, however, are beyond the scope of this thesis and can be found in reviews on dose reduction strategies.[7,73]

1.3.2 Fluence field modulation

Present technology for modulating the emitted x-ray fluence does not enable to dynamically adapt the spatial distribution of the x-ray fluence for every projection individually. While TCM enables only a modulation of the overall fluence across the projections (α), static bowtie filters distribute the fluence according to a pre-defined transmission profile that is fixed during the acquisition.[22,73] Thus, the distribution across the fan beam cannot be modulated independently for each projection. In realistic CT examinations, however, the attenuation changes due to different

1. patient sizes and anatomies (e.g., pediatric, tall, obese patients; different sex),
2. body regions (e.g., neck, shoulder, thorax, and abdomen),
3. projection angles α (lateral vs. a/p projections).

If these variations are not taken into account, the image suffers from unequally distributed noise, see Figures 1.17 and 1.18(a), and the radiation is not exploited optimally. An ideal

x-ray fluence filter would dynamically adapt the emitted x-ray fluence to the patient- and task-specific variations. However, the combination of a static bowtie filter and TCM often cannot realize the required variation in x-ray fluence that may occur in these situations. Although high-performance CT systems are equipped with multiple bowtie filters, state-of-the art x-ray pre-filtration is a compromise between different imaging scenarios.

To overcome these limitations, FFM was suggested for CT imaging. FFM allows the photon distribution to be changed across both the projections (α) *and* the fan beam width (β).[97,101] The basic idea of FFM in CT was adopted from intensity modulated radiotherapy[i] (IMRT) used in cancer treatment. As exemplified for an homogeneous elliptical phantom in Figure 1.18(b), the propagated beam differs between the lateral and the a/p projection in its peak fluence and the profile width. When moving from the a/p to the lateral projection, a higher fluence and a narrower beam profile is emitted. Thus, the radiation exposure accounts for the increasing x-ray attenuation through the object and the narrowing object cross-section toward the lateral projection.

During the last years, several technical approaches have been proposed to enable FFM in diagnostics[102,105–120] and different algorithms to control the emitted fluence have been developed.[101,103,120–127] These adjustable pre-filters and the multi-source inverse-geometry CT scanner aim to dynamically adapt the x-ray fluence to the varying attenuation. To this end, the x-ray fluence is modulated as a function of the projection and fan beam angle. In this work such a dynamic x-ray filter is referred to as dynamic beam attenuator (DBA). In literature, also "dynamic bowtie", "digital beam attenuator", or other concept-specific terms are used. A selection of relevant concepts is described later in this section ("Dynamic beam attenuator concepts").

ROI imaging

Apart from the reasons for a changing attenuation listed above (patient sizes and anatomies, body regions, and projection angles), the x-ray radiation exposure can be adapted to the given imaging task. In many CT examinations, only a specific body region or a single organ is of diagnostic interest – the ROI. In these cases it is sufficient to image exclusively the ROI at high image quality while the radiation exposure to the surrounding tissue is minimized.

To this end, a higher x-ray fluence is only emitted toward the ROI while the peripheral non-ROI tissue is exposed to a much lower x-ray fluence, as indicated in Figure 1.18(c). Hence, the emitted x-ray beam does not only adapt to the given object but also to the requirements of the imaging task. This imaging method is referred to as ROI imaging (also: volume-of-interest (VOI) imaging) and is a special case of FFM. Several

[i]Due to the parallels with IMRT, where the beam intensity is adapted according to, e.g., the patient anatomy, the target volume (i.e., tumor), or the gantry angle, FFM in CT is sometimes also referred to as intensity modulated computed tomography (IMCT).[102] Treatment plans determining the spatial dose deposition in IMRT correspond to "image quality plans" in IMCT.[103] The terminology FFM, however, describes the technique more accurately and is widely established.

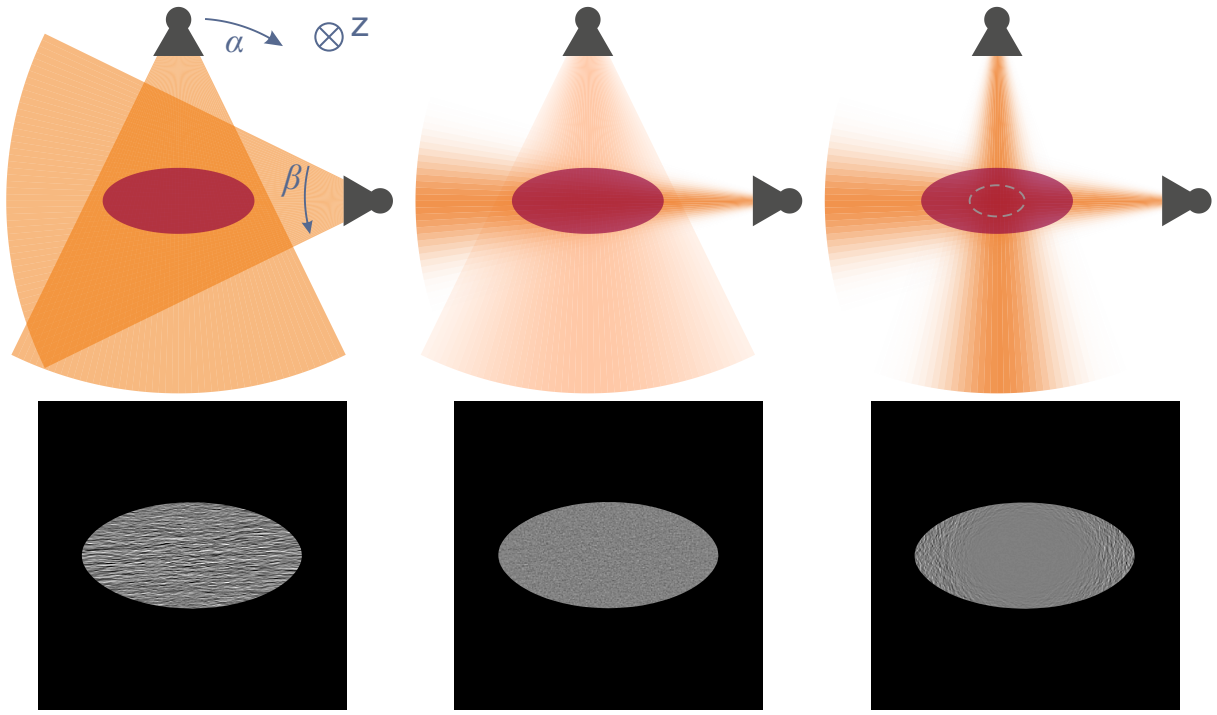

(a) (b) (c)

Figure 1.18: Principle and effect of FFM and ROI imaging. The upper row shows different configurations of the x-ray fan beam (orange) to image an elliptical homogeneous phantom (purple). A higher color saturation corresponds to a higher x-ray fluence of the emitted beam. The lower row depicts corresponding exemplary image reconstructions. (a) In the unmodulated case (no TCM, no x-ray pre-filter), the x-ray fluence is constant across all projection and fan beam angles ($N = \text{const.}\ \forall\alpha, \beta$). The reconstructed image suffers from unequally distributed image noise and a strong texture. (b) Using FFM, the peak fluence *and* the width of the transmission profile change depending on the tube position ($N \rightarrow N(\alpha, \beta)$). The reconstructed image exhibits a more isotropic noise distribution and less artifacts. (c) In ROI imaging, the x-ray fluence ($N(\alpha, \beta)$) is adapted to the elliptical ROI (circumscribed by dashed line) inside the phantom. Only the ROI is imaged at high quality while radiation dose is reduced elsewhere. Adapted with permission from Huck et al. (2019).[104]

CT researchers have proposed ROI imaging as one strategy to further enhance the dose efficiency – the radiation dose burden caused to accomplish the imaging task – in CT imaging.[7,8,22,73,77,103,120,128–133] The increase in dose efficiency by ROI imaging has been demonstrated in several studies.[122,126,127,129,130,133–137] So fay, no clinical CT system available facilitates ROI imaging, though.

Dynamic beam attenuator concepts

As mentioned earlier, different DBA concepts have been proposed aiming to realize ROI imaging. Particularly during the last decade, there has been an increased interest regarding dynamic x-ray fluence filters tailored to FFM and ROI imaging in CT. A selection of DBA approaches is briefly explained in this section. The concepts are categorized according to their basic working principle:

Movable bowtie-shaped concepts The movable bowtie-shaped DBAs comprise only a few (or even a single) movable components and resemble the cross-section of a bowtie filter. However, the shape of the transmission profiles varies by changing the position of the DBA.

The *translating attenuator*[110] is a solid body that features a bowtie-shaped cross-section. The shape changes along the z position (Figure 1.19(a)). Therefore, transmission profiles typical for a bowtie filter are obtained. A linear translation of the DBA along the z axis alters the width of the transmission profile. Alternatively, a rotation along the source-to-detector axis changes the transmission.

The *double wedge attenuator*[107,140] is composed of two opposing halves of a bowtie filter (Figure 1.19(b)). The two halves are movable along the fan beam width, independently from each other. Moving both parts closer together produces a narrower transmission profile and vice versa. Asymmetric arrangements shift the peak transmission laterally along the fan beam width.

Wedge-based concepts A more flexible modulation of the transmission profile is possible with the wedge-based DBAs. These concepts comprise several (>10) wedges, aligned in a series along the fan beam width. Due to the wedge-like shape, the height of the wedges increases along the z axis. The single wedges move independently in z direction and depending on how far a wedge is inserted into the fan beam, the transmission is changed.

The *piecewise constant attenuator*[102,113,114] (also: digital beam attenuator) comprises sets of opposing wedges with a rectangular cross-section in fan beam plane (Figure 1.19(c)). Depending on the overlap of the opposing wedges, the attenuation is controlled. Hence, the transmission behind the attenuator is piecewise constant for the part covered by a single set of wedges and varies continuously across the ensemble of adjacent wedges or the fan beam angle, respectively.

A related concept is the *piecewise linear attenuator*[111,141,142] that is composed of a series of overlapping wedges featuring a triangular cross-section instead (Figure 1.19(d)). Depending on their adjustment on the z axis, the path that the x-rays penetrate through

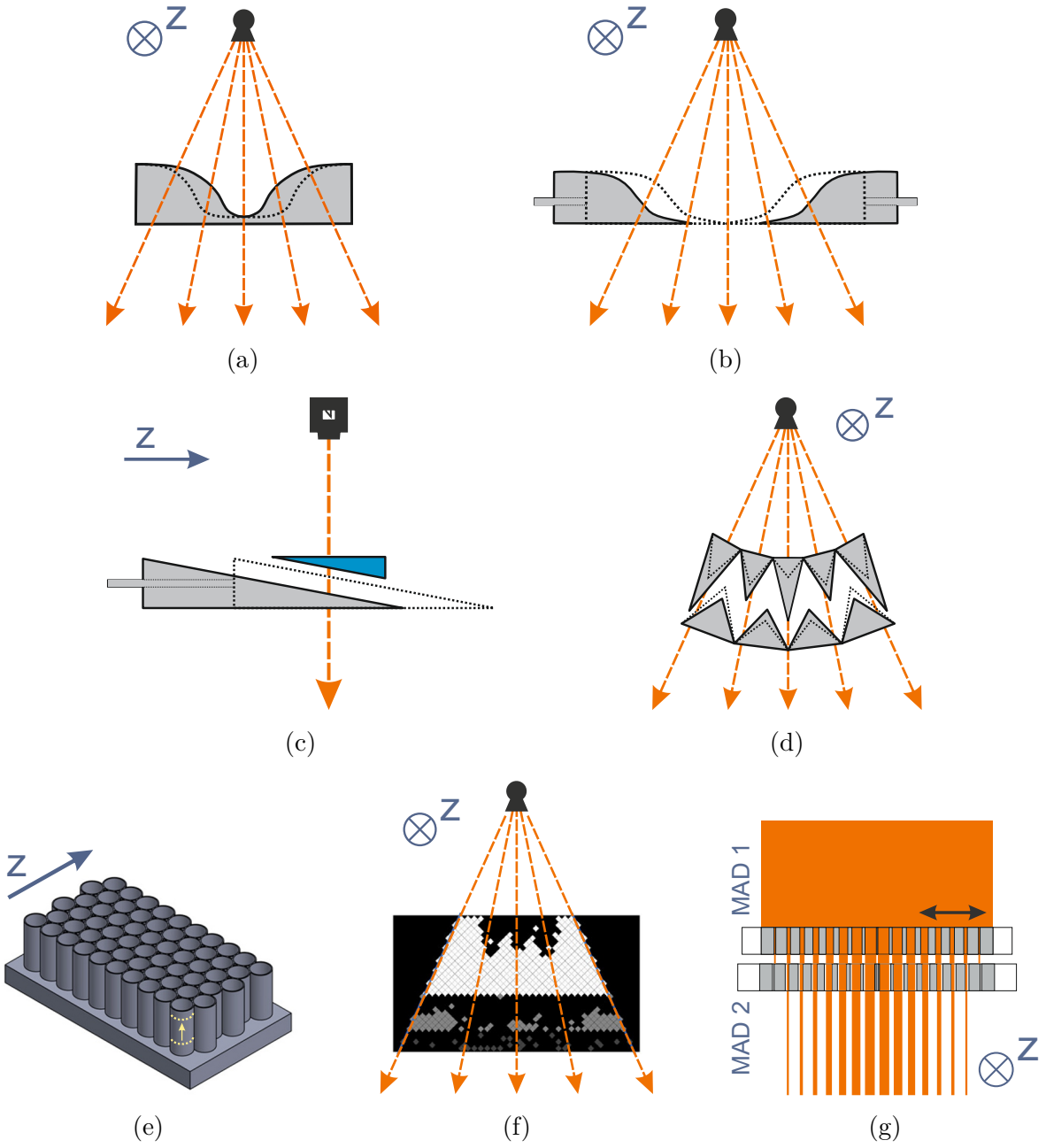

Figure 1.19: Different DBA concepts based on various working principles. (a) translating attenuator,[122] (b) double wedge attenuator,[122] (c) piecewise constant attenuator (digital beam attenuator),[135] (d) piecewise linear attenuator,[111] (e) 2D array of cylindrical cells parallel to the source-to-detector axis,[138] (f) tubes perpendicular to the source-to-detector axis (FDBF),[139] (g) based on Moiré patterns (MAD).[119] The figures are redrawn or adapted from the corresponding figures in the cited literature.

the wedges changes. Therefore, piecewise linear transmission profiles are obtained behind the attenuator.

Fluid-based concepts These DBA approaches use an array of cells or tubes located in the beam path. The cavities can be filled with an x-ray attenuating fluid to spatially modulate the attenuation of the x-ray beam during the image acquisition.

A *2D array of cylindrical cells* parallel to the source-to-detector axis is used in one approach (Figure 1.19(e)).[115,116,143] The attenuation of the x-ray beam is modulated by adapting the individual fluid levels in the cells of the DBA.

In another fluid-based approach – denoted by the authors as *fluid-filled dynamic bowtie filter* (FDBF)[117,139] – a larger number of tubes composes a 2D array parallel to the z axis (Figure 1.19(f)). The individual tubes are either filled with an x-ray attenuating fluid or evacuated in order to gradually set the transmission.

Attenuator exploiting Moiré patterns The so-called *multiple aperture device* (MAD) is a comparably compact DBA consisting of two overlapping grids.[118–120] The width of the fine-scale, highly attenuating bars varies across the grid. Likewise, the duty cycle – ratio of x-ray transparent to x-ray opaque area of the grid – changes. Thus, multiple, variably sized apertures are aligned across the fan beam width (Figure 1.19(g)). The x-rays are either blocked by the thin bars or pass the MAD. Depending on the overlap of the two grids, the x-ray transmission through the MAD is controlled. The shape of the transmission profiles is based on the Moiré effect (interference pattern), which arises from the displacement of the two grids. Only small shifts of the grids suffice to modulate the shape of the transmission profile and the lateral position of the peak transmission.

These DBA approaches aim at delivering a more patient- and task-specific fluence to enhance the dose efficiency. While prototypes have been built for some of the concepts for evaluations using an experimental setup, other approaches are merely investigated by simulations. However, none of these methods have yet been implemented in a clinical CT system to enable ROI imaging in CT. These concepts are discussed with respect to the DBA concepts presented in this thesis in Section 6.1.

1.4 Aims of the thesis

The overall aim of this thesis is to advance the "health and well-being" of the patients. To this aim, it introduces two DBA concepts that aim to deliver task- and patient-specific radiation exposures by FFM. This describes the ability to modulate the x-ray fluence during a CT acquisition and paves the way for further radiation dose reductions in CT imaging compared to state-of-the-art technology. In addition, FFM obtains diagnostic images of higher image quality due to less anisotropic noise and lower noise levels. A leap in radiation dose reduction can be achieved by performing ROI imaging, where a high image quality is realized only where it is needed and, in turn, surrounding tissue is spared from unnecessary radiation.

In order to leverage more patient-centered, dose-efficient CT imaging, this thesis pursues four major objectives:

Objective 1 *Develop and validate two DBA concepts proposed for FFM in CT.*
Taking into account the requirements of CT imaging, two DBA concepts are developed to enable FFM. Based on the two DBA concepts introduced in this thesis, physical prototypes are built and integrated into a clinical CT system. Using the modified CT system, the feasibility of the DBAs for FFM is demonstrated in a proof-of-concept.

Objective 2 *Investigate relevant physical properties of the DBA concepts.*
The influence of the DBAs on the propagated x-ray beam is analyzed and compared to that of a conventional bowtie filter. The investigations evaluate whether the transmission through the attenuators depends on the applied tube voltage, which affects the photon energies, and assess the occurrence of attenuator-induced secondary radiation. In addition, first-time image reconstructions unveil the mechanical stability of the DBAs integrated into a clinical CT system.

Objective 3 *Determine and optimize dose-efficient and task-specific DBA trajectories.*
FFM requires the DBAs to dynamically adapt to a given situation by changing the angular adjustment. In order to determine reasonable DBA trajectories, an optimization objective is developed that takes the image quality and the radiation dose by Monte Carlo (MC) simulations into account. By mimicking different (clinical) imaging tasks, it is tested whether the trajectory optimization method determines suitable, task-specific x-ray exposures for both DBAs.

Objective 4 *Explore the potential of ROI imaging among different FFM configurations.*
In ROI imaging only a specific region or organ in the patient is imaged at high quality while the radiation dose is minimized in the periphery. Employing three ROI imaging tasks (Objective 3), the dose efficiency – the radiation dose necessary to achieve the prescribed image quality inside the ROI – is compared. The comparison evaluates the potential of ROI imaging when using the most promising x-ray fluence filter for future CT systems.

Chapter 2

Materials and Methods – Part I: DBA concepts and physical properties

This chapter introduces two novel DBA concepts developed for FFM and elaborates how the physical properties of the DBA prototypes were investigated. First, the structure of these two DBA concepts is presented, followed by a description on how the DBAs dynamically modulate the propagated x-ray fluence. Based on these concepts, physical prototypes were built for experimental measurements. The manufacturing process and the actuation of the DBA prototypes are described for each DBA concept in Section 2.1. These DBA prototypes allowed to modulate the x-ray transmission through the DBAs, which was measured experimentally. The process of measuring the transmissions of the DBA prototypes in a clinical CT system is explained in Section 2.2. As elaborated in Section 2.3, the acquired DBA transmission profiles were then used to comprehensively characterize the DBAs: the variability of the transmission profiles – a decisive factor of a DBA – was investigated based on these measurements. Furthermore, the impact on spectral beam properties and the production of attenuator-induced scatter radiation when using pre-patient DBAs was explored in simulations. Reconstructed images of a phantom were used to reveal potential image artifacts due to the DBA usage. Besides the experimental measurements on a CT system, an x-ray simulation software package was used to further characterize the DBA concepts, which is described in Section 2.4.

The development of the DBAs To put the work presented in this doctoral thesis in the proper context, it is worth mentioning that the two DBA concepts presented in this chapter have been developed successively. At the beginning, there was only the idea of building a dynamic, pre-patient beam attenuator based on focused attenuation sheets. This concept was denoted as the sheet-based dynamic beam attenuator (sbDBA).[144] Starting from a simple sketch, the exact geometry of the sbDBA was determined and a first prototype was built in the scope of a master thesis preceding this work.[17] Also some representative measurements of the x-ray transmission through the sbDBA were acquired,

which generally demonstrated the ability to modulate the x-ray beam when using sbDBA. However, some challenges were identified at that time, particularly regarding the properties of the transmission profiles and the mechanical realization. The described situation, which on the one hand delivered promising findings concerning FFM and on the other hand revealed open challenges, forms the starting point of this doctoral thesis. In an effort to overcome the abovementioned limitations, the sbDBA design was revised, resulting in the z-aligned sbDBA (z-sbDBA).[145] The specific features and differences between both concepts are detailed in this chapter.

Parts of this chapter have been published in journal articles, Huck et al. (2019, 2020),[104,146] and have been presented at scientific conferences, Huck et al. (2018, 2020).[147,148] The content is reproduced with permission.

A detailed description of the applied coordinate system and the setup of a CT system is provided in Figure 1.12.

2.1 Introducing the DBA concepts

2.1.1 The sbDBA: concept and prototype

The basic principles of the sbDBA are depicted in Figure 2.1. The core component consists of an array of rectangular, highly x-ray attenuating sheets, stacked along the fan beam width (y axis) and thus perpendicular to the fan beam plane (z axis), see Figure 2.1(a). The array is located pre-patient in proximity to the x-ray tube and is covered by the x-ray fan beam. In focused position, the closely spaced attenuation sheets are focused toward the focal spot of the x-ray source. As a result, the transmitted fluence is only a little reduced by the width of the thin attenuation sheets and is constant across the fan beam, as shown in Figure 2.1(b).

The x-ray fluence through the sbDBA can be modulated in two ways: 1) The shape of the transmission profile can be varied by tilting the sbDBA about the y axis. Such a tilt, specified by the attenuation angle G, causes the peripheral attenuation sheets to defocus. Hence, the transmission toward the edges of the fan beam progressively declines. In contrast, the transmission of central rays is not affected by the tilt as the central attenuation sheets remain focused. Consequently, the peak transmission is at the center of the fan beam, compare Figure 2.1(c). 2) The location of the peak transmission can be shifted along the fan beam width by additionally tilting the defocused sbDBA about the z axis, specified by the shift angle H. Changing the shift angle H varies the direction where the attenuation sheets are focused. For shift angles $H \neq 0°$, certain off-center attenuation sheets are focused and the peak transmission is shifted accordingly, as shown in Figure 2.1(d).

Manufacturing the sbDBA prototype

The attenuation sheets of the first sbDBA prototype were composed of a tungsten alloy to provide high x-ray attenuation. The rectangular sheets were 80 µm thick, 5 mm high (along the beam propagation direction) and 50 mm long (along the z direction). The equiangular distance between adjacent attenuation sheets was approximately 0.1° in order to realize a common focus of the attenuation sheets in 220 mm distance.

The attenuation sheets were manually inserted into grooves of two opposing combs, developed for this purpose.[149] The customized apparatus guaranteed the correct position and the exact focus of the attenuation sheets, which are exposed to at high accelerations due to the CT gantry rotation.[22] The high-precision grooves were manufactured by silicon etching technology (Micromotive GmbH, Mainz, Germany). The fragile construction was reinforced by a solid frame element carrying the combs and the attenuation sheets. This frame element was mounted on a Cardan suspension (gimbal) to facilitate a simultaneous rotation about two axes. Accordingly, the Cardan suspension allowed to (manually) adjust the attenuation angle G and the shift angle H independently of each other. A picture of the sbDBA prototype is shown in Figure 2.1(e). The apparatus of the sbDBA prototype was mounted on top of the collimator box of a clinical CT system.[150] Hence, the sbDBA was located pre-patient and the attenuation sheets were focused on the focal spot of the x-ray tube in 220 mm distance. The attachment onto the collimator box, however, reduced the clearance radius (or bore radius) of the CT system by the height of the prototype. Consequently, the gantry cover of the CT system did no longer fit because of the different radii. Hence, the gantry cover had to be disassembled during the experiments and the rotating CT gantry remained opened. Furthermore, a direct access to the sbDBA prototype was required as it was adjusted manually. For measuring the sbDBA properties, the conventional bowtie filters were removed from the collimator box. The sbDBA covered an area corresponding to about 110 mm (in z direction) by 550 mm (in y direction) at the isocenter of the CT system in focused position (Figure 1.12). In defocused alignments ($G \neq 0°$), the extent in z direction was somewhat smaller due to the tilt.

2.1.2 The z-sbDBA: concept and prototype

As outlined at the beginning of this chapter, the previously introduced sbDBA revealed some technical limitations as reported in a master thesis preceding this work.[17] In particular: i) A high-frequency transmission pattern occurred at central parts of the fan beam, compare Figure 4.1. Such a signal is difficult to calibrate and potentially causes ring artifacts in the reconstructed image. ii) The transmission profiles achieved were triangular, while bell-shaped transmission profiles would be desirable for imaging typical CT geometries. iii) The sbDBA allowed for flexibly shaping the transmission. This, however, was only achieved at the expense of a high mechanical effort necessary to enable a simultaneous tilt about two axes. Therefore, the sbDBA design was revised in this thesis in order to overcome the aforementioned limitations and maintain the feasibility to dynamically adjust the transmitted x-ray fluence.

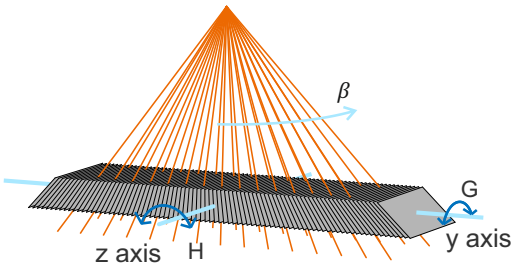

(a) perspective view

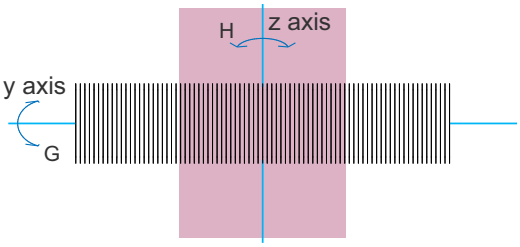

(b) $G = 0°, H = 0°$

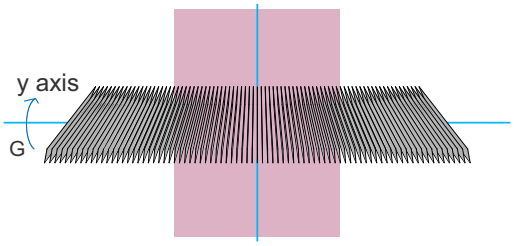

(c) $G \neq 0°, H = 0°$

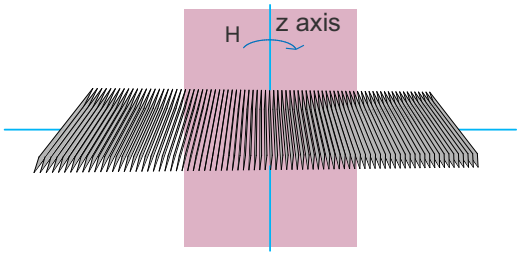

(d) $G \neq 0°, H \neq 0°$

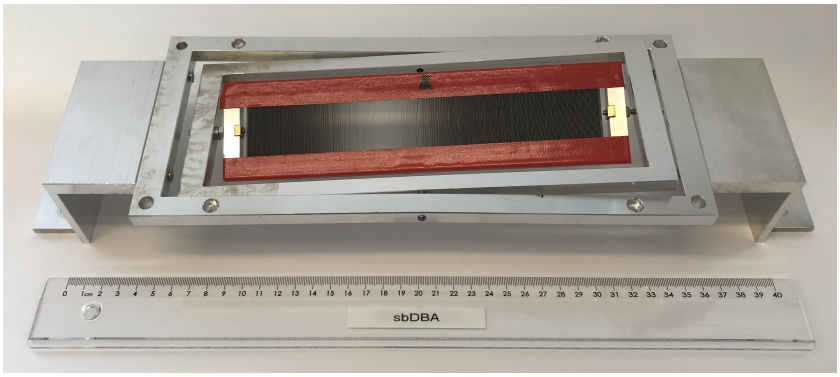

(e) sbDBA prototype

Figure 2.1: Structure and basic principle of the sbDBA in perspective (a) and beam's eye view (b)-(d). (a) The attenuation sheets (gray) of the sbDBA are stacked along the y axis covered by the x-rays (orange) of the fan beam. The sbDBA is rotatable about the y axis, specified by the attenuation angle G, and the z axis, specified by the shift angle H. (b) In focused position ($G = 0°$, $H = 0°$), the transmission is maximum and constant across the fan beam width. The purple rectangle represents an exemplary patient cross-section. (c) A tilt about the y axis by the attenuation angle G defocuses peripheral attenuation sheets and reduces the transmission toward higher fan beam angles β. (d) An additional tilt about the z axis by the shift angle H focuses off-center attenuation sheets instead and shifts the peak transmission laterally along the fan beam width. The drawings are not to scale. (e) The picture shows the sbDBA prototype mounted on the Cardan suspension. The z axis is aligned parallel and the y axis is perpendicular to the longitudinal patient axis. Adapted with permission from Huck et al. (2019).[104]

In Figure 2.2 the structure and the basic principles of the z-sbDBA are shown. Similar to the sbDBA, the z-sbDBA builds upon an array of focused, highly x-ray attenuating sheets, as shown in Figure 2.2(a). However, there are two major differences regarding the attenuation sheets in contrast to the sbDBA: 1) The attenuation sheets of the z-sbDBA are stacked along the z direction (parallel to the fan beam plan). Thus, a high-frequency structure along the fan beam, as caused by the sbDBA, is omitted. 2) The height of the attenuation sheets varies as a function of the fan beam angle β. At the center of the fan beam, the attenuation sheets are very low and symmetrically increase toward larger fan beam angles. Thus, the aspect ratio – the ratio of the height of the attenuation sheets relative to the x-ray transparent interspace between adjacent attenuation sheets – increases toward the edges.

The z-sbDBA is rotatable about the y axis, specified by the attenuation angle ϑ, in order to modulate the transmitted fluence. In focused position, i.e., $\vartheta = 0.0°$, the transmitted fluence is only reduced by the thickness of the thin attenuation sheets. Thus, the transmission is maximum in focused position and almost independent of the fan beam angle β. The ratio between the thickness of the attenuation sheets and the width of the x-ray transparent gap, the duty cycle, determines the transmission in focused position, see Figure 2.2(b). A small tilt of the z-sbDBA about the y axis ($\vartheta \neq 0.0°$) defocuses the z-sbDBA such that the x-ray source faces the sides of the attenuation sheets. By increasing the attenuation angle ϑ, the area absorbing the propagated x-ray photons can be enlarged, compare Figure 2.2(c). Due to the varying height of the attenuation sheets – very low in the center and high at the edges – the attenuation is stronger toward larger fan beam angles. This means that the transmitted fluence is almost independent of the angular adjustment at central rays whereas it can be modulated at larger fan beam angles by the attenuation angle ϑ.

Manufacturing the z-sbDBA prototype

The z-sbDBA prototype was composed of an array of alternating highly x-ray attenuating (lead) and almost x-ray transparent (paper) sheets. The width of the x-ray attenuation sheets was 21.5 µm and the height smoothly increased from 0.5 mm in the center to a maximum of 4.5 mm at the edges. The exact shape of attenuation sheets was determined heuristically. The paper sheets between adjacent lead sheets had two purposes: first, the width of the paper sheets ensured the correct distance of 100 µm between the attenuation sheets and second, the paper sheets were almost transparent for the x-ray beam. Thus, the exact distance between adjacent attenuation sheets were maintained without considerably attenuating the x-ray beam in between. As this prototype was designed to be installed inside the collimator box of a CT system, the attenuation sheets were focused toward the focal spot at 105 mm distance. Due to the high periodicity of the attenuation sheets, the finite size of the focal spot blurred the shadow of the individual attenuation sheets. The fragile array was protected against physical damage and the high centripetal forces (Section 1.2.3) by a customized plate of carbon fiber reinforced polymer.

The apparatus for actuating the z-sbDBA prototype

In contrast to the sbDBA, which was attached on top of the collimator box and adjusted manually, the z-sbDBA was mounted inside the collimator box and actuated by an electric drive. For this purpose, the conventional bowtie filters were removed from the collimator box of the clinical CT system[150] to provide the necessary space for the z-sbDBA. A rotatable suspension was attached to the housing of the collimator box carrying the z-sbDBA, as shown in Figure 2.2(d). The suspension enabled the rotation (y axis) and ensured that the z-sbDBA was located in the exact position, 105 mm from the focal spot and 490 mm from the isocenter of the CT system (Figure 1.12). The z-sbDBA was directly connected to a rotational, electric drive equipped with a high-resolution encoder (*EC-4pole30/16RIO*, Maxon Motor GmbH, Munich, Germany) to move the z-sbDBA precisely. The drive was controlled by a customized firmware package, executed on a field-programmable gate array (FPGA) board that allowed to adjust the z-sbDBA at the desired attenuation angle. The FPGA board further facilitated to maintain and to record the angular position of the z-sbDBA. It also featured the ability to store a scheduled trajectory, which was retrievable by a trigger. The trigger was activated by either a control command or a specific angular position of the CT gantry. For the purpose of radiation protection, the data connection between the FPGA, connected to the z-sbDBA prototype, and the control computer was established via a wireless local area network (WLAN) module. Hence, a safe and wireless remote control of the z-sbDBA was realized from outside the examination room. The additional components, the FPGA board, the WLAN module and the modified collimator box were mounted on a collimator module of the CT system, see Figure 2.3(a). After being equipped with the additional components, the collimator module was installed in the CT system, see Figure 2.3(b).

The integration of the z-sbDBA prototype into the standard hardware components of the CT system and the remote control allowed the CT system to be completely reassembled and closed by the gantry cover. Hence, the modification by the z-sbDBA prototype on the CT system was visually not noticeable. This, in contrast, was not feasible with the sbDBA prototype because the attachment on the collimator box of the CT system reduced the clearance radius and thus made the reassembly of the CT gantry cover impossible.

2.1.3 The adjustable static z-sbDBA concept

The adjustable static z-sbDBA is closely related to the z-sbDBA. This DBA concept differs from the z-sbDBA only in its mode of operation, not in the hardware. Unlike the z-sbDBA, that allows for adapting the attenuation angle during the data acquisition ($\vartheta(\alpha) \neq \text{const.}$), the adjustable static z-sbDBA is adjusted in an optimized, task-specific angular position before the actual acquisition ($\vartheta(\alpha) = \text{const.}$). This position is held during the acquisition across all projection angles α. The optimal angular position can be determined by a suitable optimization method taking into account the respective imaging task, as suggested in Section 3.3.

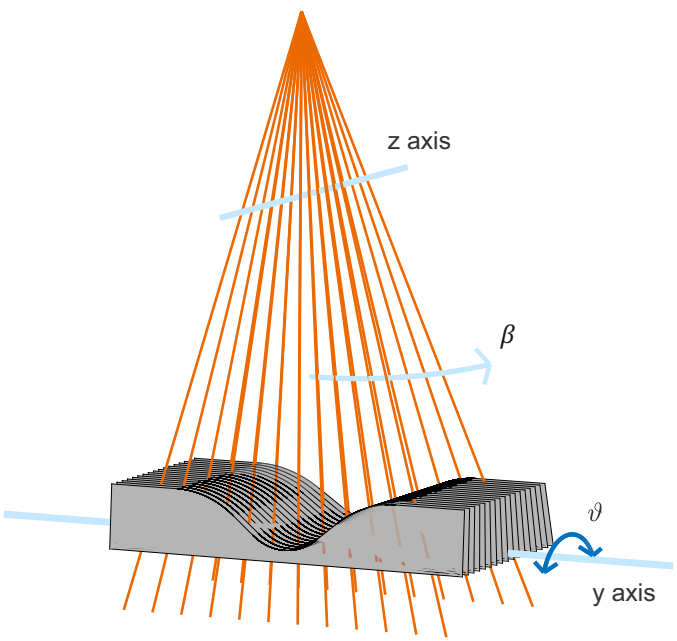

(a) perspective view

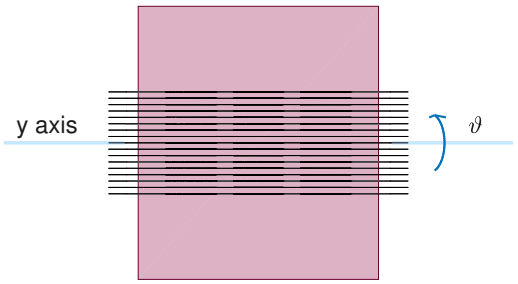

(b) $\vartheta = 0.0°$

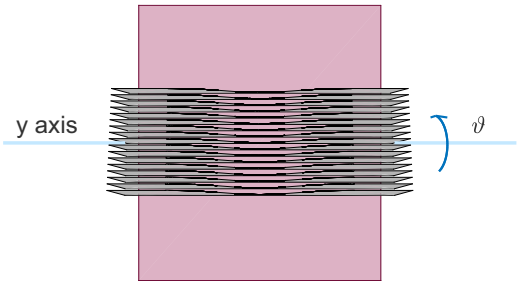

(c) $\vartheta \neq 0.0°$

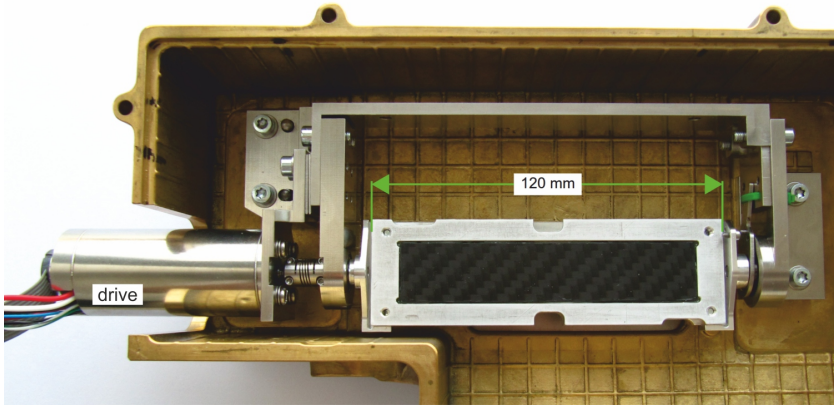

(d) z-sbDBA prototype

Figure 2.2: Structure and basic principle of the z-sbDBA in perspective (a) and beam's eye view (b) - (d). (a) The z-sbDBA is composed of curved attenuation sheets (gray) stacked along the z axis. It is rotatable about the y axis specified by the attenuation angle ϑ and covered by x-rays (orange) of the fan beam. (b) In focused position ($\vartheta = 0.0°$), the transmission is hardly affected by the attenuation sheets and constant across the fan beam width. The purple rectangle represents an exemplary patient cross-section. (c) A tilt about the y axis ($\vartheta \neq 0.0°$) defocuses the attenuation sheets and reduces the transmission toward larger fan beam angles β. The drawings are not to scale. (d) The picture shows the z-sbDBA prototype (black rectangle) carried by a suspension that enables the tilt about the y axis. The drive (left) is directly connected to the z-sbDBA. The setup is mounted into a modified collimator box (bronze) of a clinical CT system. The z axis is parallel and the y axis is perpendicular to the longitudinal patient axis. Adapted with permission from Huck et al. (2020).[146]

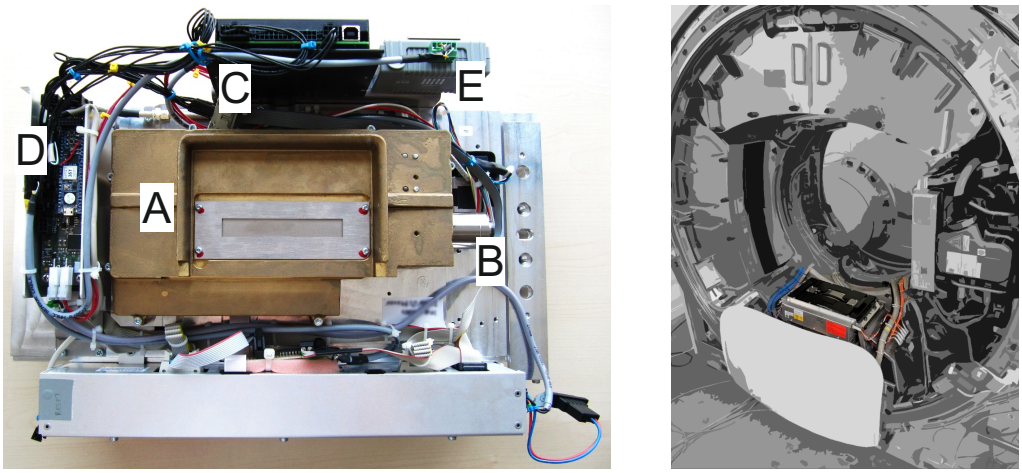

(a) modified collimator module (b) modified CT system

Figure 2.3: Integration of the z-sbDBA prototype into the clinical CT system. (a) The collimator box (A) that incorporates the z-sbDBA prototype (B), see Figure 2.2(d), is mounted on the collimator module of the CT system. The collimator module further carries the motor controller (C), the FPGA board (D), and the WLAN module (E). (b) The modified collimator module is installed (upside down) into the gantry of a clinical CT system, which can be closed after assembly. Some features are blurred to protect confidential details.

The conceptual advantage of this DBA concept is the reduced mechanical complexity. It was motivated by the fact that a resilient, reliable actuation of a dynamic fluence filter is mechanically demanding and a known issue in the field of FFM.[113,122,125] This alternative approach attempts to simplify the mechanical operation of the z-sbDBA by disabling the DBA movement during the acquisition. Accordingly, the risk of image artifacts due to mechanical inaccuracies, which potentially can occur during the movement of a DBA, is mitigated. For example, deviations from the target angular alignment due to the heavy g-forces or miscalibrations can lead to ring artifacts in the reconstructed image. Due to the simplified operation, the adjustable static z-sbDBA is assumed to be technically less demanding and less prone to errors. The reduced complexity is attained at the expense of a limited flexibility in modulating the emitted x-ray fluence, though. A task-specific transmission profile is propagated but in return a dynamic modulation during the acquisition is sacrificed.

2.2 Acquiring the DBA x-ray transmission data

This section details the acquisition process of the x-ray transmission achievable with the described DBAs. For this purpose, a clinical CT system was equipped with the respective DBA prototypes. Additionally, the x-ray transmission of two different bowtie filters was measured for performance comparisons.

2.2.1 The CT system

The measurements of the attenuator transmission profiles were conducted on a clinical CT system (*SOMATOM Force*, Siemens Healthcare GmbH, Forchheim, Germany),[150] modified only by the installation of the respective DBA, see Figure 1.12. The focus-to-detector distance was 1085.6 mm and the focus-to-isocenter distance was 595 mm. The detector comprised 920 detector channels along the fan beam width (approximately: $-24° < \beta < 24°$) and 96 detector rows along the z direction with a pixel size corresponding to approximately 0.6 mm × 0.6 mm at the isocenter of the CT system. The measurements were conducted with the following standard parameters: the raw detector signal was acquired at 120 kVp anode voltage, 300 mA tube current, 1 s rotation time, constant focal spot position and without TCM. In cases where deviating parameters were used, the modified settings are denoted explicitly in the respective section.

The transmission τ of an attenuator was determined as the raw detector signal s, measured with the respective attenuator in the beam path, divided by the raw detector signal s_0 of a calibration measurement (reference) without any attenuator (i.e., without bowtie filter, without DBA) in the fan beam path:

$$\tau = \frac{s}{s_0} \tag{2.1}$$

Accordingly, the transmission τ was normalized ($\tau \in [0, 1]$). The maximum transmission achievable in focused position is denoted as the maximum x-ray transmissivity $\tau_{\max} \leq 1$ of the attenuator.

2.2.2 The sbDBA x-ray transmission

The conventional bowtie filters of the CT system were removed and the sbDBA prototype, described in Section 2.1.1, was installed instead in order to measure the transmission $\tau(G, H)$ of the sbDBA experimentally. The transmission was averaged over the detector rows for the 1D transmission profiles. The sbDBA alignment was performed manually and controlled by a digital protractor (*SPI TRONIC Pro 360 Digital Level*, Swiss Precision Instruments Inc. La Palma, CA, USA) to improve the precision of the angular alignment.[151] Due to the manual alignment of the sbDBA angles (G, H) and the risk of injury from the rotating opened CT gantry, the measurements were an elaborated process. For example, one practical obstacle was that the opened CT gantry rotates quickly and its components are under voltage, which can lead to serious accidents. Normally, this does not pose a risk because the CT gantry is closed by the gantry cover and is therefore inaccessible. Due to safety reasons, it was mandatory to stop the CT gantry from rotating and to turn off the gantry power every time the sbDBA alignment was changed. Afterwards, the CT gantry had to be rebooted again to finally measure the transmission at the adjusted angle. Measurements of a larger number of angular combinations would have been too extensive and likely have suffered from mechanical and practical limitations. Thus, the transmission $\tau(G, H)$ through the sbDBA prototype was only acquired at a few representative

angular combinations. However, in the subsequent dose efficiency comparison (Chapter 5), transmission profiles covering a broader range of angular combinations were necessary, which were obtained from MC simulations, see Section 3.2 for details.

2.2.3 The z-sbDBA x-ray transmission

All transmission profiles of the z-sbDBA and the adjustable static z-sbDBA were measured on the same clinical CT system equipped with the z-sbDBA prototype, as described in 2.1.2. Therefore, the conventional bowtie filters were replaced by the z-sbDBA apparatus. All measurements of the transmission profiles were acquired twice in two successive scans. Hence, noise-only difference images, where the object structure is removed and only the image noise is left, were available. The 1D transmission $\tau(\vartheta)$ was based on the detector signal of a central detector row (no. 42) averaged over the readings of an entire rotation (1152 readings in total).

2.2.4 The bowtie filter x-ray transmission

In addition, the transmission profiles of the bowtie filters regularly integrated in the clinical CT system were acquired. This allowed a comparison between the DBAs and state-of-the-art static bowtie filters, as used in a contemporary CT system. The unmodified CT system considered in this thesis typically accommodates two bowtie filters: one of the filters, here called the *regular bowtie*, is immovable and thus permanently within the fan beam. It represents the regular attenuator to modulate the propagated fluence. The considered CT system is additionally equipped with another bowtie filter, denoted as the *narrow bowtie*. It produces a narrower transmission profile due to the stronger x-ray attenuation toward the edges of the fan beam. Hence, the narrow bowtie is commonly used for cardiac or pediatric applications. Depending on the application, the narrow bowtie is moved in the beam path before the image acquisition starts. However, it cannot be moved in and out during an acquisition.

2.3 Evaluating the physical properties of the DBAs

This section details how the main properties of the DBAs were analyzed. In addition to the main feature of a DBA – the ability to modulate the x-ray fluence – also spectral and scatter properties were investigated, giving an insight into the interactions of the x-ray radiation when passing the attenuator. Furthermore, image reconstructions of homogeneous phantoms were used to evaluate the mechanical stability of the DBAs.

2.3.1 Modulating the x-ray transmission of the DBAs

Experimental measurements

The feasibility of FFM and the versatility of the transmission achievable with the DBAs was subject of this experiment. Therefore, the transmissions $\tau(\beta)$ were investigated as a

function of the fan beam angle β. Additional 2D measurements of the transmission $\tau(\beta, z)$ at different fan beam planes – also referred to as image planes – were acquired to reveal potential variations along the z direction. The coordinate system is described in Figure 1.12.

Feasibility and versatility of FFM

To demonstrate the feasibility of fluence modulation by using the DBAs, transmission profiles $\tau(\beta)$ produced by the sbDBA and the z-sbDBA were measured using the respective prototype. The achievable range of transmissions was investigated by adjusting the DBA prototypes at different DBA angles.

For the sbDBA, the transmission profiles were measured at some exemplary attenuation angles $G \in \{0°, 25°, 35°\}$. In addition, the transmission at the shift angles $H \in \{0°, 1°, 2°\}$ were obtained from measurements of the defocused sbDBA ($G = 35°$). The transmission profiles of the z-sbDBA were measured at attenuation angles ranging from $\vartheta_{min} = 0.0°$ to $\vartheta_{max} = 2.2°$ in steps of $\Delta\vartheta = 0.1°$. The resulting transmission profiles $\tau(\beta)$ revealed the fluence modulation depending on the DBA angles (G, H, and ϑ) across the fan beam width β.

Variations along the z axis (off-center fan beam planes)

2D transmissions $\tau(\beta, z)$ obtained from the defocused sbDBA ($G = 35°$ and $H = 0°$) and the defocused z-sbDBA ($\vartheta = 1.5°$) were analyzed to unveil potential deviations of the transmission along the z direction at different fan beam planes. Therefore, the detector signals – corresponding to the transmission τ – across the detector area and in particular along the detector rows 15, 48, and 81 were compared.

2.3.2 Spectral dependency of the x-ray transmission

Experimental measurements

Due to interactions of the x-ray radiation when penetrating the matter composing the attenuator, the spectrum of the radiation can change. These changes in the spectrum, e.g., beam hardening, can entail changes in the resulting transmission. Hence, the influence of the tube emission spectrum on the transmission τ was investigated by measurements on the CT system. This experiment was conducted for the sbDBA, the z-sbDBA, and the two bowtie filters. To vary the mean energy of the emission spectrum, two tube voltages were chosen within the typical range of CT acquisitions. The low-voltage measurement was performed at $U_{low} = 80\,\text{kVp}$ for all fluence filters. The measurement at the higher tube voltage was at $U_{high} = 140\,\text{kVp}$ in the case of the bowtie filters and the z-sbDBA and $U_{high} = 150\,\text{kVp}$ in the case of the sbDBA. The discrepancy regarding the higher tube voltage was due to different dates of data acquisition and intermediate changes in the scan log. The DBA transmissions were measured at a strongly attenuating adjustment to intensify potential differences: the sbDBA was adjusted at $G = 35°$ and $H = 0°$ and the z-sbDBA at $\vartheta = 2.0°$. The measurements were repeated with the regular and the narrow bowtie filter installed instead to allow for a comparison between the DBAs and current

filter technology. The measurements were performed at the same tube current. Deviations regarding the photon count were considered due to the normalization of the transmission τ, see Eq. 2.1.

The spectral dependency of the x-ray transmission was assessed by comparing the transmission measured in the low-voltage measurement, $\tau(U_{low})$, with the transmission that was achieved in the high-voltage measurement, $\tau(U_{high})$, at the same detector channel:

$$\frac{\tau(U_{high}) - \tau(U_{low})}{\tau(U_{low})} \tag{2.2}$$

This ratio was calculated for every detector channel individually. Subsequently, all ratios calculated were re-sorted: instead of a representation along the detector width, the results were sorted according to the remaining transmission at the low tube voltage $\tau(U_{low})$. Thus, the variation between both tube voltages were shown as a function of the remaining transmission $\tau(U_{low})$, which was chosen as a surrogate for the "strength" of fluence modulation. According to this method (Eq. 2.2), a ratio close to 0 indicates perfect independence of the transmission from the emission spectrum. Likewise, deviations from 0 demonstrate that the transmission depends on the tube voltage (emission spectrum), which requires an additional calibration routine.

2.3.3 Attenuator-induced secondary radiation

MC-based simulations

Interactions of x-ray photons with the bowtie filters is a source of scatter radiation prior to the patient. Scattered x-ray photons that impinge on the patient increase the patient radiation dose and potentially impair the image quality.[25,102,152–154] Hence, secondary radiation, induced when passing the fluence attenuator, was investigated for the sbDBA as well as for the z-sbDBA and was compared with the regular bowtie filter. The 2D distributions of exclusively secondary radiation propagating toward the examined object was simulated in MC simulations. The software package used, called *MOCASSIM*, is detailed in a separate section, see Section 2.4.1.

A model of each of the attenuators was created in the MC simulation software, which replicated the geometry and material properties of the physical prototypes. The sbDBA was aligned at $G = 25°$ and $H = 0°$, the z-sbDBA was aligned at $\vartheta = 1.0°$ to approximately match the x-ray transmission achieved with the bowtie filter. An idealized detector that registers exclusively the signal of secondary radiation was employed and located closely behind (20 mm) the respective attenuator. The detector surface was designed about 10 % larger than the attenuator area in order to detect also strongly scattered radiation. An x-ray fan beam was simulated by 10^{10} photons emanating from an extended focal spot toward the attenuator. The photons were sampled from polychromatic 120 kVp tungsten spectrum with spectral pre-filtration to resemble a realistic CT energy spectrum.

2.3.4 Image reconstruction

Experimental measurements

The sbDBA and the z-sbDBA represent highly structured, movable objects within the fan beam path. Thus, mechanical inaccuracies potentially can cause severe (ring or band) artifacts in the reconstructed images. For example, the high centripetal forces occurring during the CT gantry rotation, causing accelerations of 40 g and above,[22] or an imperfect angular alignment or calibration can be reasons for these inaccuracies. Accordingly, a preliminary evaluation of the sensitivity of the DBA prototypes to mechanical deviations was made. In first-time acquisitions of a cylindrical phantom, the data acquired using the mounted DBA prototypes were reconstructed by FBP. First, calibration scans (with DBA, without phantom) were performed using the sbDBA or the z-sbDBA, respectively. Thereby, the sbDBA was adjusted to $G = 35°$ and $H = 0°$ (manually; digital protractor) and the z-sbDBA to $\vartheta \in \{1.0°, 2.0°\}$ (automatically; electric drive). Second, phantom scans (with DBA, with phantom) were conducted under the same angular adjustments. The DBAs had intentionally been moved between the calibration and the phantom scan in order to account for potential inaccuracies of the setup, particularly of the movement mechanism. Furthermore, some time had elapsed between both measurements to account for potential deviations of the CT system or the environment (e.g., humidity, temperature). Homogeneous phantoms were employed in order to better detect potential image artifacts. In the case of the sbDBA, a cylindrical water phantom (diameter: 30 cm, length: 10 cm) was placed at the isocenter of the CT system. A standardized computed tomography dose index (CTDI) phantom (diameter: 32 cm, length: 15 cm) was used in the case of the z-sbDBA. It was composed of polymethyl methacrylate (PMMA) featuring a mass density of $\rho = 1.18\,\mathrm{g/cm^3}$. Slightly different phantoms were used due to the availability in the lab at the time of the respective experiments.

2.4 X-ray simulation software

2.4.1 MOCASSIM

In multiple investigations reported in this thesis, the so-called *MOnte CArlo Scatter SIMulation* (*MOCASSIM*) software was used. It is a MC simulation package dedicated to diagnostic x-ray radiation (Siemens Healthcare GmbH, Forchheim, Germany).

MC simulations are a useful *in silico* tool to investigate the physical properties of an x-ray beam employed in a user-specified CT acquisition. It simulates the transport and the interactions of a single particle (e.g., x-ray photon) when propagating through the specified setup. The history (e.g., direction, initial energy, type of interaction) of a particle is calculated based on databases and models that describe the random nature of particle-matter interactions. If secondary particles are created due to interactions of the primary particle, the histories of the secondary particles are simulated as well. To properly describe the propagation as well as spectral features of the x-ray beam, a large number of photon histories is necessary. Thus, the simulation is repeated for many primary particles

to provide sufficient statistics. In this manner, the characteristics of a CT system can be investigated without conducting the experiments on a real CT system.

MOCASSIM provides a MC-based framework to simulate x-ray radiation described by individual beam characteristics, such as the beam geometry or the spectrum. The simulations can further comprise typical components of a CT, for example, specific filters, grids and detectors. The phantom object and the components can be designed using a variety of geometries. According to the MC method, photons emanate from the focus with an initial, random direction within the specified beam geometry. Their initial energy is sampled from the specified spectrum, described by the maximum tube voltage and optional spectral pre-filters. Then, the photons propagate step-wise through the simulation setup while interacting with the objects therein.

MOCASSIM considers all photon interactions relevant for diagnostic x-ray radiation, the photoelectric effect, Compton and Rayleigh scatter, K emission and reabsorption. The atomic interaction data are based on databases of the Nuclear Energy Agency (NEA), the Evaluated Photon Data Library (EPDL) and the Evaluated Atomic Data Library (EADL). *MOCASSIM* has been validated with the results presented in Chan and Doi (1983).[155,156]

2.4.2 DRASIM

Furthermore, a deterministic ray propagation simulation software, called *Deterministic RAdiological SIMulation* (*DRASIM*), was employed in this thesis. It allows to simulate the beam properties in a customized x-ray imaging setup (Siemens Healthcare GmbH, Forchheim, Germany).[157] The setup can, e.g., comprise individualized object and beam geometries, pre-filters, collimators, or detectors. *DRASIM* draws straight paths (rays) from the sample points of the x-ray focus through the various objects to the detector (sub-) pixels. Along these paths, the attenuation of the x-ray beam when propagating through transmitted objects (filters, grids, phantoms etc.) is calculated. The attenuated x-ray beam can be measured with a detector behind the sample.

For calculating the attenuation of the primary x-ray radiation, *DRASIM* uses the so-called *narrow beam approximation* (Eq. 1.20), taking into account only the photoelectric effect, Compton and Rayleigh scattering. *DRASIM* uses the EPDL and EADL databases of the NEA for calculating the interaction processes. From this, the intensity and the spectrum of the transmitted radiation are calculated for a given setup.

Chapter 3

Materials and Methods – Part II: Application and evaluation of DBAs in ROI imaging

This chapter describes the optimization of the DBA operation and compares the potential of ROI imaging in x-ray CT between different FFM techniques. To this end, three exemplary ROI imaging tasks relevant in the field of diagnostic CT examinations were defined (Section 3.1). Different configurations enabling FFM – including combinations of TCM with state-of-the-art attenuators or the DBAs – were considered in this thesis (Section 3.2). To compare the movable DBAs with other FFM configurations, first, the exact trajectory of the DBAs were optimized with respect to the specific imaging tasks. Therefore, an optimization objective was proposed that accounts for the x-ray fluence-specific patient dose and image quality (Section 3.3). The resulting optimization framework allows to determine the optimal DBA trajectory and the DBA fluence transmission, respectively, for each imaging task (Section 3.3.4). Finally, the optimization framework was employed to compare the FFM configurations with each other regarding their dose efficiency in the imaging tasks. This comparison explores the potential of ROI imaging and the clinical benefit when using the specific FFM configuration (Section 3.4).

Parts of this chapter have been published in a journal article, Huck et al. (2021),[158] and have been presented at a scientific conference, Huck et al. (2020).[159] The content is reproduced with permission.

3.1 ROI Imaging tasks

The benefit of FFM in ROI imaging was studied on three exemplary ROI imaging tasks relevant in x-ray CT diagnostics. The imaging tasks employed a comparably simple phan-

tom or a model of a female thorax. In addition, the possibility of centering an off-centered ROI by adapting the patient table height was considered.

The specifications of the imaging tasks describe the phantom cross-section in the transverse plane (uv plane) of the phantom. All phantoms were homogeneously extended in z direction (phantom length in z direction: 300 mm) in order to realistically include scattered radiation inside the phantoms. Figure 3.1 depicts the phantom cross-sections associated with the imaging tasks I-III. The respective ROI is circumscribed by a purple line. The uv plane describes the location in the reconstructed images. This plane is parallel to the fan beam plane and perpendicular to the z axis of the CT system (Figure 1.12).

3.1.1 Imaging task I: Elliptical water phantom with central ROI

In this imaging task, a water phantom with elliptical cross-section (semi-axes: 200 mm × 100 mm) was considered. The phantom was located at the isocenter ($u = v = 0$ mm) of the CT system. The elliptical ROI (semi-axes: 100 mm × 50 mm) was centered inside the phantom ($u = v = 0$ mm), as indicated by a purple line in Figure 3.1(a).

3.1.2 Imaging task II: Female thorax with off-centered heart ROI

This imaging task describes a more complex phantom: a model of a female thorax composed of breast, heart, lung, ribs, spine, and sternum was studied. The rib cage of the body is circumscribed by an ellipse (semi-axes: 200 mm × 100 mm) placed at the isocenter ($u = v = 0$ mm). The heart of the phantom, located off-centered, defined the ROI ($u = 0$ mm, $v = 40$ mm, radius: 35 mm), see Figure 3.1(b). The female thorax phantom is a modification of the thorax phantom provided by the *FORBILD* project.[160]

3.1.3 Imaging task III: Off-centered female thorax with centered heart ROI

This imaging task is a variation of imaging task II. It was motivated by the limited FFM flexibility provided by the z-sbDBA. In contrast to the more flexible sbDBA, that allows to vary the width *and* the location of the transmission profile, the z-sbDBA only modifies the profile width, compare Section 2.1. To compensate for this limitation, the situation was investigated where the heart ROI was positioned at the CT isocenter by adjusting the patient table height accordingly. Hence, the same phantom geometry as in imaging task II was used. However, the entire thorax was slightly moved (rib cage: $u = 0$ mm, $v = -40$ mm) in order to position the heart ROI at the isocenter ($u = v = 0$ mm), compare Figure 3.1(c).

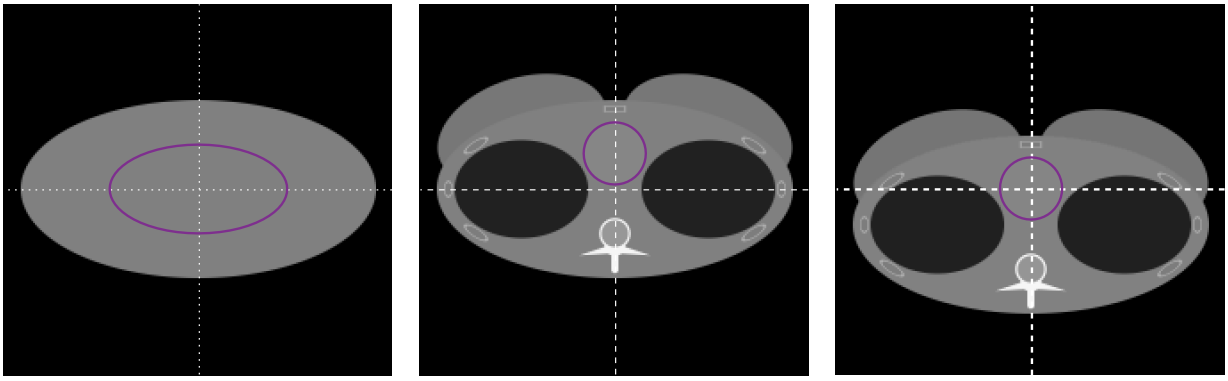

(a) (b) (c)

Figure 3.1: Phantom geometries of imaging tasks I-III. (a) The elliptical water phantom with a central ROI. (b) The female thorax phantom located at the isocenter with the off-centered heart ROI. (c) The female thorax phantom moved such that the heart ROI is positioned at the isocenter. The ROIs are circumscribed by a purple line. The intersection of the white dotted lines indicates the isocenter of the CT system. The uv plane describes the transverse plane of the phantom. Horizontal: u axis; vertical: v axis. Reproduced with permission from Huck et al. (2021).[158]

3.2 Configurations for fluence field modulation

The potential of ROI imaging was compared among seven different FFM configurations. The FFM configurations differed by the x-ray fluence filter employed and whether TCM was used, as summarized in Table 3.1.

In the first FFM configuration, *noAtt_tcm0* (no. 1), no in-beam filtration (no fluence filter) and no TCM were employed. Accordingly, the emitted fluence was constant across all projection α and all fan beam β angles. This FFM configuration was considered as the reference scenario as it describes a native CT system without any kind of fluence modulation and thus constitutes an explicit, reproducible reference.

In all the other configurations (no. 2 to no. 7), a method for TCM – here denoted as heuristic square root TCM (hsqTCM) method – was applied. This TCM method modulates the tube current factor $\kappa(\alpha)$ proportional to the square root of the maximum object attenuation $L_{\text{obj}}(\alpha)$ in each projection α, given by:

$$\kappa(\alpha) \propto \sqrt{\max_{\beta} L_{\text{obj}}(\alpha)}. \tag{3.1}$$

The object attenuation $L_{\text{obj}} = s_0/s$ was calculated from the ratio of the primary (s_0) and the detected photon count (s). This TCM calculation method is a modification of the so-called "central ray approximation" method proposed in Gies et al. (1999)[89] and Kalender et al. (1999).[90] While the modulation of the tube current according to the "central ray approximation" exclusively considers the attenuation occurring in the *central ray* per projection, the hsqTCM method employed in this thesis (Eq. 3.1) accounts for the *maximum*

Table 3.1: Overview of the FFM configurations considered for the comparison on ROI imaging. TCM is realized according to Eq. 3.1.

no.	key	fluence filter (τ)	TCM (κ)	filter type
1	*noAtt_tcm0*	no[j]	off[k]	n/a
2	*noAtt_tcm1*	no[j]	on	n/a
3	*reg_bowtie_tcm1*	regular bowtie	on	static
4	*nar_bowtie_tcm1*	narrow bowtie	on	static
5	*sbDBA_tcm1*	sbDBA	on	dynamic in G, H
6	*zsbDBA_tcm1*	z-sbDBA	on	dynamic in ϑ
7	*as_zsbDBA_tcm1*	adjustable static z-sbDBA	on	adjustable in ϑ

attenuation per projection. The modified hsqTCM method was motivated by the fact that the strongest x-ray attenuation does not necessarily occur at the central ray per projection in an inhomogeneous object. In the case of the female thorax, for example, the attenuation of lateral projections can be higher for non-central rays than for the central ray that passes two low-attenuating lung volumes. The hsqTCM method was similarly implemented in a study by Fu et al. (2017).[161]

In the second configuration, *noAtt_tcm1* (no. 2), the propagated fluence was only modulated across the projection angle α following the hsqTCM method. No in-beam filtration (no fluence filter) was used in this configuration. The configurations no. 3 and no. 4 imitated a modern clinical CT scanner (*SOMATOM Force*, Siemens Healthcare GmbH, Erlangen, Germany).[150] Therefore, the regular (*reg_bowtie_tcm1*) or the narrow (*nar_bowtie_tcm1*) bowtie filter were employed in addition to TCM, compare Section 2.2.4. The inclusion of the bowtie filters allows for a comparison between current CT technology and a (fictitious) CT system equipped with one of the DBA prototypes. A CT system equipped with the sbDBA is described by configuration no. 5 (*sbDBA_tcm1*). A system incorporating the z-sbDBA in the fully dynamic operation mode is represented by configuration no. 6 (*zsbDBA_tcm1*), while a system with the z-sbDBA in the adjustable static mode is given by configuration no. 7 (*as_zsbDBA_tcm1*). The respective transmission profiles τ of the bowtie filters and the z-sbDBA (applicable also for the adjustable static z-sbDBA) were adopted from the measurements on a real CT system as described in Section 2.2. Only the transmission profiles of the sbDBA were based on MC simulations, as detailed and justified in the subsequent part ("Extending the set of sbDBA transmission profiles").

Each FFM configuration resulted in an individual primary x-ray distribution $\Gamma(\alpha, \beta)$, determined as the product of the tube current factor $\kappa(\alpha)$ (see Eq. 3.1) and the attenuator specific transmission $\tau(\alpha, \beta)$ (see Eq. 2.1):

$$\Gamma(\alpha, \beta) = \kappa(\alpha) \times \tau(\alpha, \beta), \text{ where } \Gamma > 0. \tag{3.2}$$

Accordingly, the primary x-ray distribution $\Gamma(\alpha, \beta)$ quantifies the total photon number, emitted toward the object under investigation.

[j]The setting "no" fluence filter corresponds to: $\tau(\alpha, \beta) = \text{const.}\ \forall \alpha, \beta$

[k]The setting TCM "off" corresponds to: $\kappa(\alpha) = \text{const.}\ \forall \alpha$

Extending the set of sbDBA transmission profiles

The transmissions τ achievable with the sbDBA prototype were measured only at a few representative angular combinations of G and H on the CT system because of the extensive effort associated with the experimental measurements. Sections 2.2.2 and 2.3.1 describe the acquisition and the modulation of the x-ray transmissions through the sbDBA prototype when being mounted on a real CT system. However, a much larger set of transmission profiles that describes the fluence modulation achievable with the sbDBA was vital for optimizing the trajectory of the sbDBA regarding a given imaging task, as explored in Section 3.3.4. In order to extend the data provided by the measurements, a model of the sbDBA prototype was implemented in *MOCASSIM*. Relevant properties of the clinical CT system used in the DBA measurements (distances of components, focal spot size, detector geometry, spectral pre-filtration etc.)[150] were considered in the simulations, compare Section 2.2.1. In all simulations, 10^7 individual photon histories were simulated, emitted from an extended focal spot (area: about $1\,\mathrm{mm}^2$) toward the detector. The photons were sampled from a typical CT spectrum (tungsten anode, 120 kVp) including a spectral pre-filtration for low-energy photon absorption. Using *MOCASSIM*, the transmissions $\tau(G, H)$ produced at the attenuation angles $G \in [15°, 59°]$ in steps of $\Delta G = 1°$ were simulated, each combined with the set of shift angles covering $H \in \{0.0°, \pm0.2°, \pm0.4°, \pm0.6°, \pm0.8°, \pm1.0°, \pm1.2°, \pm1.5°, \pm2.0°, \pm2.5°, \pm3.0°\}$. Accordingly, numerous transmission profiles (945 possible angular combinations) of the sbDBA were obtained from the *MOCASSIM* simulations, covering a broad range of attenuation and shift angles. This would not have been practicably achievable with experimental measurements using the sbDBA prototype on the CT system. Yet, the experimental measurements that reveal the transmission at some angular combinations (Section 2.2.2), were used to validate the corresponding transmission obtained from the *MOCASSIM* simulations. Further references validating the *MOCASSIM* software package are given in Section 2.4.1.

3.3 Fluence optimization

This section describes how the DBA trajectory was optimized. The DBA trajectory determines the x-ray transmission $\tau(\alpha, \beta)$ through the DBA, and thus affects the primary x-ray distribution $\Gamma(\alpha, \beta)$, compare Eq. 3.2. An entire DBA trajectory is composed of a single transmission profile (feasible with the respective DBA) determined for every projection angle α. To account for the characteristics of the individual imaging task an optimization objective was introduced. The optimization objective incorporates the patient dose and the image quality in the ROI. These quantities and the process of trajectory determination are explained in the following sections.

3.3.1 Optimization objective for dose efficiency enhancement

The method used to optimize the propagated primary photon distribution Γ is intended to enhance the dose efficiency by minimizing the dose per image quality in the ROI. Ac-

cordingly, the optimization objective aims at i) maximizing the image quality inside the ROI and ii) minimizing the patient radiation dose. Therefore, the inverse of the mean pixel variance inside the ROI, $1/\sigma^2_{\mathrm{ROI}}$, was determined as the measure for image quality inside the ROI. The patient radiation dose δ was calculated by estimating the effective dose. Hence, the optimization objective is described by

$$\arg\min_{\Gamma(\alpha,\beta)} \delta \cdot \sigma^2_{\mathrm{ROI}}. \tag{3.3}$$

The calculation of the two factors determining the optimization objective, the radiation dose and the image quality, are detailed in Section 3.3.2 and Section 3.3.3. This criterion assumes that radiation dose and image variance are inversely related, as given by the Brooks' relation[63,64] (Eq. 1.29). This assumption is valid under the condition that the detector signal is not too low such that, e.g., electronic noise can be neglected, and is common practice.[63,127,162–164]

The optimization objective was applied to identify the transmission profiles that optimize the primary fluence and eventually to determine the final DBA trajectory, compare Section 3.3.4. Furthermore, the optimization objective was considered to quantitatively compare different FFM configurations (Table 3.1) regarding their dose efficiency in ROI imaging, as elaborated in Section 3.4.

3.3.2 Dose calculation

The effective dose δ caused by an arbitrary photon distribution Γ is one out of two factors determining the optimization objective (Eq. 3.3). In order to estimate the dose allocation of a photon distribution Γ, initially, MC simulations were conducted using *MOCASSIM* for each imaging task. The MC simulation software is further detailed in Section 2.4. In the simulations, a CT scan was divided into 72 projection angles $\alpha \in [0°, 355°]$ with $\Delta\alpha = 5°$. At each projection angle, the fan beam was composed of 49 adjacent beamlets b. In this thesis, a beamlet $b(\alpha, \beta)$ denotes a section of the entire fan beam and is specified by a projection angle α and a fan beam angle β. Each beamlet b covered $\Delta\beta = 1°$ such that the entire fan beam spanned the angular range of $\beta \in [-24°, 24°]$. This allows to describe any primary photon distribution $\Gamma(\alpha, \beta)$ as a linear superposition of the individual beamlets. The extension of the fan beam in z direction was neglected.

The CT geometry of these simulations resembled the geometry of the CT system used in the measurements to obtain the DBA transmission profiles, compare Section 2.2. An individual MC simulation was conducted for every beamlet b at a specific fan beam and projection angle. In every simulation, a total of 10^6 photons were emitted along the beamlet according to a typical CT spectrum (120 kVp tungsten anode, spectral pre-filtration) toward the detector area. The phantom volumes, see Section 3.1, were divided into dose voxels $\nu(u, v, z)$, each spanning a volume of 2 mm × 2 mm in u and v direction and 100 mm along the z axis. The energy loss when a photon interacted with the object was attributed to the respective voxel ν of the phantom. The local mass densities $\rho(u, v, z)$ of an object were obtained from the phantom geometries constructed with *MOCASSIM* and assigned

to the corresponding phantom dose voxels $\nu(u, v, z)$. Hence, the absorbed dose per photon caused by a specific beamlet $b(\alpha, \beta)$ was calculated for every dose voxel of the phantom. In this manner, a comprehensive 5D dose allocation matrix $M(\alpha, \beta, u, v, z)$ was generated that quantifies the dose allocation caused by a beamlet $b(\alpha, \beta)$ per photon in every voxel $\nu(u, v, z)$. The corresponding 4D dose allocation matrix $\bar{M}(\alpha, \beta, u, v)$ was calculated by summing up the (scatter) contributions along the z direction:

$$\bar{M}(\alpha, \beta, u, v) = \sum_{z} M(\alpha, \beta, u, v, z). \tag{3.4}$$

Once this dose allocation matrix was calculated, it was used to determine the spatial dose deposition D in the object for any primary photon distribution Γ. Therefore, a matrix multiplication of the 4D dose allocation matrix $\bar{M}(\alpha, \beta, u, v)$ and the photon distribution $\Gamma(\alpha, \beta)$ was performed. The calculation returned the spatial dose deposition $D(u, v)$ per voxel volume:

$$D(u, v) = \sum_{\alpha,\beta} \bar{M}(\alpha, \beta, u, v) \times \Gamma(\alpha, \beta). \tag{3.5}$$

By virtue of this method, the spatial dose deposition, in terms of absorbed dose, caused by any photon distribution Γ can be calculated fast and accurately, and eventually, be visualized in a 2D dose map $D(u, v)$, compare Section 3.4.2.

Effective dose

The dose quantity subject to the optimization objective in Eq. 3.3 is denoted as effective dose δ. Hence, the dose measure used in this work accounts for the biological effectiveness of the type of radiation and for the (stochastic) sensitivity of tissue to ionizing radiation, compare Section 1.2.5.

For the calculation of the effective dose δ, first, the phantom was segmented into its relevant tissue types, see Table 3.2. The reference values of the organ and tissue masses were adopted from the data proposed by the ICRP.[165] The segmentation was performed based on the local mass density $\rho(u, v, z)$ in every voxel of the phantom. Consequently, a tissue type was assigned to each voxel $\nu(u, v, z)$ of the phantom, as depicted in Figure 3.2. The segmentation and tissue-specific weighting was only relevant for the female thorax phantom because of the heterogeneous tissue composition. In contrast, "residual tissue" was assumed throughout the homogeneous water phantom. In the next step, the absorbed dose in each type of tissue, the organ dose D_T, and the equivalent dose H_T (radiation weighting factor w_R for x-rays: $w_R(\text{x-ray}) = 1$) were calculated from the fluence-specific spatial dose deposition $D(u, v)$ determined in Eq. 3.5. Eventually, the effective dose δ, caused by the specific radiation exposure Γ, was approximated according to Eq. 1.36. The resulting approximation of the effective dose additionally accounts for the tissue-specific weighting factors w_T as listed in Table 3.2.

It should be noted that the calculation of this dose metric represents an approximation of the effective dose suggested by the recommendations of the ICRP.[70] Minor deviations

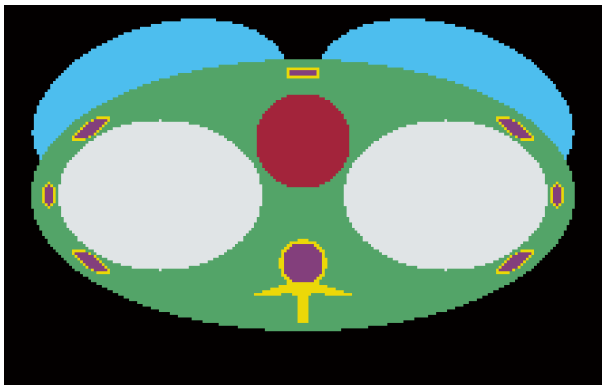

Figure 3.2: Phantom segmentation of the female thorax phantom. Blue: breast; gray: lung; dark red: heart; yellow: bone surface; purple: bone marrow; green: residual tissue; black: air. The image pixel size represents the dose voxel size. Reproduced with permission from Huck et al. (2021).[158]

Table 3.2: Overview of the tissue-specific weighting factors according to the ICRP recommendations.[70]

tissue / organ	weighting factor w_T
breast	0.12
lung	0.12
bone surface	0.01
bone marrow	0.12
residual tissue	0.12

arise due to the phantom geometry, which is homogeneously extended and limited in z direction. Hence, the radiation exposure of other organs (e.g., liver, bladder, colon etc.) was not included. Nevertheless, this approximation seemed reasonable, as the deviations were assumed to be negligible: organs not included in the phantom description would be located outside the primary radiation where the radiation exposure is much lower and thus their contribution to the total dose is comparably small. Moreover, the evaluation of the effective dose was used to compare the different FFM configurations relatively, not in absolute values.

3.3.3 Image quality calculation

The second factor contributing to the optimization objective in Eq. 3.3 is the image quality. The image quality is characterized by the the mean image variance that is achieved inside a specific ROI, σ^2_{ROI}, by an arbitrary photon distribution Γ. Initially, the attenuation sinogram P of every imaging task was determined. The attenuation sinograms were generated by the so-called *DRASIM* simulation software. Further details are presented in Section 2.4.2. The relevant properties of the CT system used in the measurements were

mimicked, compare Section 2.2.1, in order to match the geometries and the acquisition settings. Accordingly, the attenuation sinograms $P(\alpha, \beta)$ were composed of 920 detector signals at 1152 projections. Comparable to the role of the dose allocation matrix $\bar{M}$ in the dose calculation (Section 3.3.2), the attenuation sinogram P constitutes the basis for simulating the effect of an arbitrary photon distribution Γ on the image quality. In every fluence simulation, noise was added to the (raw) attenuation sinogram P, returning the noise-adapted attenuation sinogram P_{noise}. In accordance with photon statistics (Section 1.2.3), the noise was Poisson distributed based on the detector photon count, which depends on the individual photon distribution Γ and the object attenuation L_{obj}. Afterwards, the noise-adapted attenuation sinogram P_{noise} was reconstructed by FBP[1]. Images based on two independent noise realizations were reconstructed for each simulation of a specific photon distribution. This additional step was necessary to calculate difference images featuring exclusively the noise characteristics, not the anatomy of a heterogeneous phantom, e.g., the female thorax. Eventually, the mean image variance inside the specific ROI, σ^2_{ROI}, was determined from the difference image. The regions from which the image variance was calculated, the ROI, was assumed to be sufficiently large to obtain reliable statistics from two individual noise realizations. The mean image variance was selected as an appropriate choice for optimizing the primary fluence in FFM. This choice is justified by the findings reported in a fundamental work on fluence optimization by Harpen (1999).[166] The study demonstrates that the minimization of the total image variance, which can be replaced with the mean image variance, is proven to be the most dose efficient method for FFM.

Beyond that, the final image reconstructions obtained in the ROI imaging comparison were additionally evaluated in terms of their noise texture. To this end, the isotropy of the NPS calculated from 100 difference images was considered to evaluate the image quality more comprehensively, as detailed in Section 3.4.3.

3.3.4 DBA trajectory determination for optimized FFM

The overall aim of the trajectory determination was to find a DBA trajectory such that the corresponding fluence maximized the dose efficiency according to the optimization objective (Eq. 3.3). Hence, the algorithm employed for determining a discrete DBA trajectory accounted for the given imaging task, the transmission profiles feasible with the respective DBA, and the optimization objective, which incorporates the effective dose and the image quality. It considered TCM according to Eq. 3.1.

The trajectory determination algorithm subsequently identified the optimal DBA angles $G(\alpha)$ and $H(\alpha)$, or $\vartheta(\alpha)$ for each projection angle α in an iterative manner, as illustrated in Figure 3.3. The optimization resembles a coordinate descent method with discretized coordinates.

[1]Reconstruction kernel: *Qr36f*, according to the notation used for Siemens Healthcare systems. A soft reconstruction kernel was applied as no small-feature detection but an impression of the overall image quality was intended.

Initially, a moderate fluence filtration, i.e., $G(\alpha) = 15°$ and $H(\alpha) = 0.0°$, or $\vartheta(\alpha) = 0.3°$, respectively, was employed for all projection angles not yet optimized (gray in Figure 3.3). It was necessary to choose some fluence at every projection to enable a proper image reconstruction. The trajectory optimization was initiated at the projection angle α_0, optimizing $G(\alpha_0)$ and $H(\alpha_0)$, or $\vartheta(\alpha_0)$. At the projection angle currently being optimized (green in Figure 3.3), each transmission profile $\tau(\beta)$ from a set of potential transmission profiles was evaluated one after the other. During this process, the fluence at the remaining 71 projection angles was kept unchanged, compare Figure 3.3(a). Then, the transmission profile delivering the best (i.e., the lowest) optimization objective, was chosen for the current projection angle and kept during the evaluation of the remaining projection angles in this iteration (orange in Figure 3.3).

Subsequently, a tube position about 90° further was considered to evaluate the next projection angle according to the described evaluation process. The evaluation of the tube positions was performed following a skipping sequence to avoid an imbalance of the superimposed fluence, which could have led to inappropriate trajectories when processing adjacent tube positions instead. The sequence of projection angles α was 0°, 90°, 180°, and 270°, followed by 5°, 95°, 185°, and 275° and so on, compare Figure 3.3(b). The lateral projections corresponded to $\alpha \in \{0°, 180°\}$, the anterior projection to $\alpha = 90°$ and the posterior projection to $\alpha = 270°$. Accordingly, the best transmission profile and its associated DBA angle were identified at each projection angle. After having evaluated all 72 projection angles that constitute an entire rotation, the first iteration was completed, see Figure 3.3(c).

The trajectory optimization of the second iteration was initiated from the trajectory identified in the first iteration. In analogy to the first iteration, the projection angles were evaluated consecutively per projection angle until the optimal transmission profiles were identified. Afterwards, the trajectory resulting from the second iteration was smoothed in order to avoid inappropriate wide (angular) steps between adjacent tube positions. Furthermore, this step mitigated fluctuations of the trajectory.

From the third iteration on, the number of DBA angles considered in the evaluation per projection was limited to accelerate computational time and to omit inappropriate angles, as detailed later in this section ("DBA specific adaptations"). The set of potential transmission profiles was restricted to the latest trajectory point plus / minus one angular increment (ΔG, ΔH, $\Delta\vartheta$), as given in Section 3.2 (ΔG, ΔH) and in Section 2.3.1 ($\Delta\vartheta$). The presented algorithm was proceeded iteratively aiming to further minimize the optimization objective by optimizing the primary photon distribution Γ. The optimization process was terminated when the trajectory remained constant between two consecutive iterations or when the improvement of the optimization objective was less than 2 ‰. The described trajectory optimization algorithm was realized in a customized script executed in MATLAB (Mathworks Inc., Natick, MA, USA).

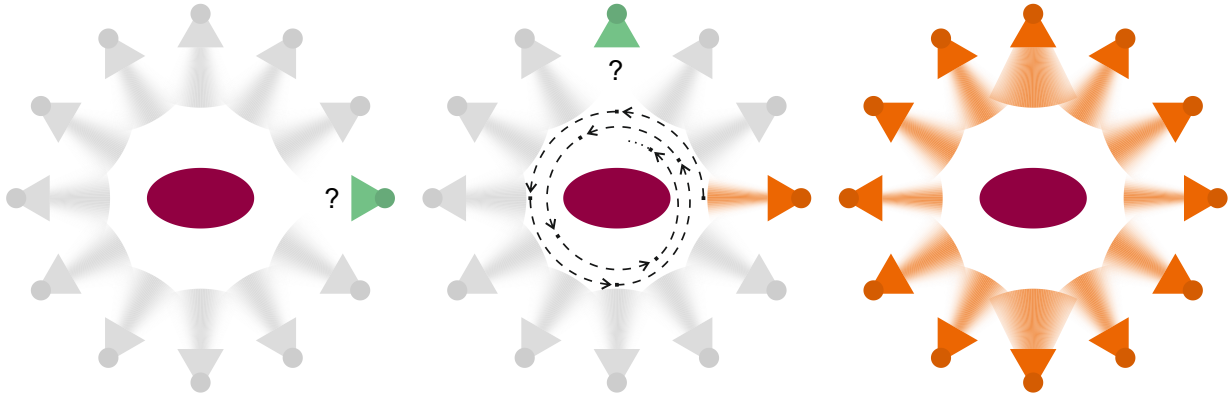

Figure 3.3: Scheme for sequentially determining and optimizing the DBA trajectory. A task-specific object (purple) is imaged from multiple perspectives, corresponding to multiple positions of the x-ray tube. The tube position currently under evaluation in the respective step is colored in green. A tube position that has already been optimized is colored in orange. The gray tube positions indicate projection angles not yet optimized. (a) The optimization process is initiated at projection angle $\alpha_0 = 0°$, corresponding to the lateral projection. (b) Having the first projection optimized, the next tube position (anterior: $\alpha = 90°$) is evaluated. The dashed arrows indicate the alternated sequence (in steps of about 90°) considered for the optimization. (c) An iteration is completed when all projections are optimized. Note the varying width of the single fan beams in (c) representing different transmission profiles of the DBA. For better illustration, only a few exemplary tube positions (12 instead of 72) are shown in this figure. Adapted with permission from Huck et al. (2020).[159]

DBA specific adaptations

In principle, the same trajectory optimization algorithm was used for the three DBAs. Some individual deviations, owed to the concept of the respective filters, are explained in the following.

sbDBA

As the sbDBA is rotatable about two axes simultaneously, a larger number of possible combinations of attenuation angles ($G \in [15°, 59°]$) and shift angles ($H \in [-3.0°, 3.0°]$) was available (945 in total), as described in Section 3.2. In order to reduce computational time, a scheme was implemented for pre-selecting reasonable angular combinations while rejecting others. The heuristic approach considered angular combinations that propagate the peak transmission toward the ROI as appropriate. This approach assumed that a higher fluence is necessary at regions where high image quality is required and lower fluence where dose deposition is penalized with respect to the optimization objective. The pre-selection scheme is detailed in the following step by step.

Independent of any optimization, the detector channel $d_{\max}(G, H)$ exposed to the peak transmission at each angular combination of G and H was retrieved from the transmission profiles $\tau(G, H)$ and stored in a look-up table. At the beginning of a trajectory optimization, the detector channel $d_{\mathrm{ROI}}(\alpha)$ onto which the ROI center is projected at each tube position was calculated as a function of the projection angle α. By matching the location of the peak transmission ($d_{\max}$) with the ROI center (d_{ROI}), only transmission profiles τ were derived per projection angle that propagate their peak transmission toward the ROI center. Thereby, a small margin around the detector channel d_{ROI} was permitted in order not to be unnecessarily restrictive in the selection. Hence, the target detector channel was extended by the ± 37 detector channels adjoining the detector channel d_{ROI} (corresponding to approximately $\pm 22\,\mathrm{mm}$ at the isocenter). Accordingly, the pre-selected set of angular combinations encompassed only trajectory profiles whose peak intensity was propagated toward the ROI center (including the small margin). This set of angular combinations was considered in the ensuing trajectory optimization process.

This pre-selection process was applied in the first and second iteration, only. As of the third iteration, only the trajectory points of the latest iteration and combinations with the adjacent trajectory points ($\pm\Delta G$ and $\pm\Delta H$) were regarded for the optimization, as aforementioned in the general description.

z-sbDBA

Various transmission profiles, corresponding to the attenuation angles $\vartheta \in [0.0°, 2.2°]$, have been acquired by measurements, as detailed in Section 2.3.1. All transmission profiles $\tau(\vartheta)$ were considered for the optimization in the first and the second iteration. In higher iterations, only the latest attenuation angle and the two neighbors ($\pm\Delta\vartheta$) were evaluated.

adjustable static z-sbDBA

Due to the operation mode of the adjustable static z-sbDBA, the same transmission profile was used at all projection angles ($\vartheta(\alpha) = \text{const.}\ \forall\,\alpha$). Accordingly, the optimization objective was evaluated for acquisitions where the attenuation angle was constant across the projections. This evaluation was conducted for every transmission profile available ($\vartheta \in [0.0°, 2.2°]$) within a single iteration.

3.4 Comparing the potential dose reduction by ROI imaging using different FFM configurations

This section elaborates the methodology used to investigate the potential of ROI imaging. Therefore, the dose efficiency was quantified and compared among the FFM configurations. The dose efficiency was assessed by the dose necessary to achieve a prescribed image variance inside the ROI (Section 3.4.1). For a visual validation, the associated 2D dose maps were calculated to show the resulting spatial dose deposition across the phantom (Section 3.4.2). Furthermore, a score to quantify the NPS isotropy was introduced. It describes the image quality more comprehensively and was used as an additional measure to ensure equal image quality (Section 3.4.3). The configuration-specific radiation exposures were further used to reconstruct images of the water phantom and to generate the corresponding variance maps that portray the image quality throughout the phantom cross-section (Section 3.4.4).

3.4.1 Dose efficiency

To determine the dose efficiency of a certain radiation exposure the formula describing the optimization objective (Eq. 3.3) was adopted. Accordingly, the dose efficiency realized by each FFM configuration (Table 3.1) was calculated for every imaging task. This allowed to compare the FFM configurations regarding their ability of efficiently modulating the propagated fluence in accordance with the aim of the imaging tasks (Section 3.1).

The configuration no. 1, *noAtt_tcm0*, that represented a CT system where no in-beam modulation and no TCM was employed, was selected as reference in this comparison. In order to conduct a fair comparison, the FFM configurations were compared at the same image quality, i.e., the mean ROI image variance σ^2_{ROI}. For this purpose, the image quality was calculated for every FFM configuration, incorporating the specific attenuator transmission $\tau(\alpha, \beta)$ and the tube current factor κ. In the case of evaluating a DBA (no. 5 to no. 7), the optimized DBA trajectories, determined by the presented trajectory determination method, were used. Then, the overall radiation exposure Γ was linearly scaled until the resulting image quality matched the reference image quality in terms of ROI image variance. This method was assumed eligible, as the image variance and the radiation dose are inversely related according to the approximation given by the Brooks' relation (Eq. 1.29). Based on the variance-equalized fluence determined for every FFM configuration, the ef-

fective patient dose δ was calculated. It described the radiation dose required to achieve the demanded level of image quality. Consequently, the effective patient dose, found for the specific FFM configuration, is a measure to assess the suitability of a FFM configuration regarding ROI imaging. This method allows for a quantitative comparison among the different FFM configurations.

In imaging tasks II and III, the organ dose D_T associated with breast tissue was calculated separately in addition to the effective patient dose δ.

3.4.2 Dose map

For each FFM configuration, an individual 2D dose map was obtained from the variance-adjusted fluence, revealing the spatial dose deposition in the phantom. The 2D dose maps visualize the spatial dose deposition $D(u, v)$ across the phantom cross-section in terms of absorbed dose, as described by Eq. 3.5. This allows to visually compare the dose deposition between the FFM configurations. The pixel size of the 2D dose map is $2\,\text{mm} \times 2\,\text{mm}$, compare Section 3.3.2.

3.4.3 NPS isotropy score

Image variance is a common but not all-encompassing indicator for image quality, as explained in Section 1.2.4. In particular, it does not describe the isotropy of noise in an image, which can disclose, e.g., streak artifacts. Due to pragmatic reasons (especially time consumption), however, the image variance was used to optimize the DBA trajectories and to adjust the image quality for the dose efficiency comparison.

Nevertheless, to obtain information about the noise isotropy in the examined ROI, an additional image quality metric was employed on the final, variance-adjusted image reconstructions obtained from the dose efficiency comparison: the NPS isotropy score ϵ_{NPS}. It is a measure taking into account the uniformity and the intensity of the image noise occurring in an image. The quantity is limited to $0 < \epsilon_{\text{NPS}} < 1$, where a low value implies highly anisotropic noise and a high value represents perfect noise isotropy. The essential steps to determine the NPS isotropy score ϵ_{NPS} are summarized in the following and are visualized in Figure 3.4. A more detailed description is presented in the work by Hayes et al. (2018)[167] who first described the isotropy score. Using the attenuator-specific primary photon distributions Γ employed in the dose efficiency comparison, 100 difference images (i.e., noise-only images) were calculated from a set of noise-independent image reconstructions. Then, the region circumscribed by the ROI was extracted from the 100 difference images to determine the corresponding two-dimensional NPSs nps_{2D} (Section 1.2.4) in the ROI.[66] Based on the 100 two-dimensional NPSs nps_{2D}, the average two-dimensional NPS $\overline{nps}_{\text{2D}}$ was calculated. In the next step, the one-dimensional NPSs – the radial NPS profiles nps_{1D} – were sampled along the polar angles $\varphi \in [0°, 359°]$ from the average two-dimensional $\overline{nps}_{\text{2D}}$,

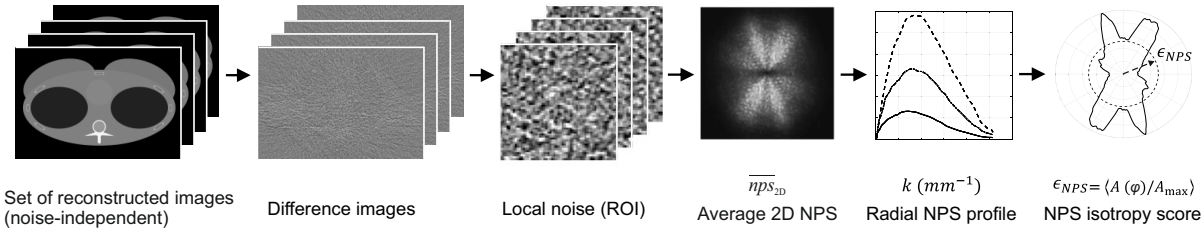

Figure 3.4: Calculation of the NPS isotropy score ϵ_{NPS}. Difference images are calculated from a set of noise-independent image acquisitions. Then, local noise images of the ROI were used to determine the averaged 2D NPS and the associated radial NPS profiles. Finally, the NPS isotropy score ϵ_{NPS} was obtained from the average of the normalized areas $A(\varphi)$ under the radial NPS profiles. Adapted from Hayes et al. (2018).[167]

where $\Delta\varphi = 1°$. The area $A(\varphi)$ under the radial NPS profiles $nps_{1\mathrm{D}}$ was determined for each polar angle, incorporating the spatial frequency k:

$$A(\varphi) = \int_0^\infty nps_{1\mathrm{D}}(\varphi)\, k\, dk \tag{3.6}$$

Normalized by the maximum area occurring among the radial NPS profiles, $A_{\max}$, the NPS isotropy score ϵ_{NPS} was obtained:

$$\epsilon_{\mathrm{NPS}} = \langle \frac{A(\varphi)}{A_{\max}} \rangle \tag{3.7}$$

Accordingly, this additional image quality metric describes the noise texture in a single quantity, which might not be adequately captured by the image variance alone. Hence, the NPS isotropy score ϵ_{NPS} was calculated for the final image reconstruction in the dose efficiency comparison to ensure that the image quality did not suffer from the usage of the DBAs or the potential dose reductions. Generally, the NPS represents the noise characteristics more comprehensively than the image variance and can be used as an indicator for predicting the performance of a CT system.[65,168–170]

3.4.4 Image reconstruction and variance map

According to the optimization method applied, the mean image variance inside the ROI was equalized in the reconstructed images. The image variance outside the ROI was not specified. It can, however, complement information retrieved from the 2D dose maps $D(u, v)$. Therefore, some exemplary image reconstructions and the corresponding image variance distributions were evaluated in the case of imaging task I.

The image reconstructions were taken from the results of the dose efficiency comparison, as described in Section 3.4.1. According to that methodology, the emitted, attenuator-specific fluence Γ was linearly scaled in order to equalize the image quality inside the ROI (σ^2_{ROI}) of the image reconstructions. The image quality outside, in contrast, was specific for the adaptation of the individual FFM configuration.

The variance maps characterize the spatial distribution of the variance in each pixel of a reconstructed image. Therefore, 100 noise-only difference images were calculated based on image reconstructions with random Poisson noise realizations. The attenuator-specific fluence Γ determined previously was applied to perform the image reconstructions. The determination of the set of difference images was comparable to the methodology to determine the NPS isotropy score. Eventually, the variance in each pixel across a set of 100 noise-only difference images was calculated.

Chapter 4

Results & Discussion – Part I: DBA concepts and physical properties

This chapter provides a proof-of-concept of the DBA prototypes and investigates their physical properties. First, the possibility of modulating the x-ray fluence using the DBA prototypes on a clinical CT system is demonstrated. A wide range of transmission profiles achievable is a vital aspect for realizing FFM. Besides the transmission along the fan beam width, changes along the z direction are analyzed (Section 4.1). The second part addresses the question of how the emission spectrum affects the transmission through the DBAs compared to the bowtie filters (Section 4.2). Generally, the spectral properties of an x-ray beam changes when penetrating matter due to photon interactions. Consequently, the transmission through the filters can differ between higher and lower tube voltages producing the x-ray beam. A closely related aspect is attenuator-induced scatter radiation, which typically occurs when x-ray radiation passes a fluence filter (Section 4.3). Attenuator-induced scatter is an adverse side effect when using fluence filters as it contributes to the patient dose and can deteriorate the image quality. To evaluate this effect, the scatter radiation induced in the DBAs is compared with that of the regular bowtie filter. Lastly, first-time image reconstructions of a phantom, acquired using the DBA prototypes mounted on a clinical CT system, are analyzed (Section 4.4). This is a crucial aspect because placing a movable and highly structured object in the beam path bears the risk of image artifacts. Hence, the reconstructed images give a first impression regarding the sensitivity of the DBA prototypes to mechanical inaccuracies.

In this chapter, some of the data related to the sbDBA have already been acquired during the master thesis of the author preceding this doctoral thesis. This concerns particularly the experimental measurements of the sbDBA transmission, which have been used for evaluations presented in the master thesis.[17] Some investigations on the sbDBA conducted for

this chapter rely, in parts, on the same raw data. Except for the image reconstruction (Figure 4.6(a)), however, different experiments were performed in the course of this doctoral thesis, which thus presents new original findings on the sbDBA.

Parts of the results presented in this chapter have been published in journal articles, Huck et al. (2019, 2020),[104,146] and have been presented at scientific conferences, Huck et al. (2018, 2020).[147,148] The content is reproduced with permission.

4.1 Modulating the x-ray transmission of the DBAs

Experimental measurements

In this section, first, the key function of a DBA – the variation of the x-ray transmission – is experimentally investigated using the sbDBA and the z-sbDBA prototypes. Therefore, the transmission $\tau(\beta)$ achievable at different angular adjustments (G, H, or ϑ) is shown as a function of the fan beam angle β. Furthermore, 2D transmissions $\tau(\beta, z)$ unveil potential variations along the z direction of the CT system.

It should be noted that a feature occurring at a particular fan beam angle is measured at the corresponding detector channel. In the following, the occurrence of a feature is therefore either specified by a detector channel or the corresponding fan beam angle.

Feasibility and versatility of FFM

The modulation of the x-ray transmission achieved in experimental measurements using the sbDBA prototype is depicted in Figure 4.1. In focused position ($G = 0°$, $H = 0°$), the transmission is almost constant across the fan beam width or the detector channels, respectively. Due to the presence of the sbDBA in the beam path, the maximum transmission achievable, described by the maximum x-ray transmissivity, is lowered to $\tau_{\max} \approx 0.75$ (normalized) compared to the absence of any fluence pre-filter. By increasing the attenuation angle G, the transmission substantially reduces toward the periphery of the fan beam while the maximum transmission in the center is maintained. At detector channel 220, for example, the remaining transmission is $\tau_{220}(G = 25°) \approx 0.45$ or $\tau_{220}(G = 35°) \approx 0.15$, respectively. The transmission decreases to a minimum of about $\tau \approx 1/1000$ at highly shielded, peripheral channels. Note that it is important that the mean photon count is not completely truncated. A complete x-ray shielding would cause photon starvation or even data truncation artifacts, which are difficult to account for in the image reconstruction process.[48,129,171–173] The fluence modulation in defocused alignments ($G \neq 0°$, $H = 0°$) results in triangular transmission profiles with the peak transmission in the center. As apparent from the curves in Figure 4.1, the location of the peak transmission is controlled by the shift angle H. A slight tilt influences the lateral occurrence of the triangular transmission profiles. At $H = 2°$, for example, the peak transmission is shifted by about 170 detector channels, corresponding to about 96 mm at the isocenter. The general shape of the transmission profiles is not considerably affected by the lateral shift. A leap of the remaining transmission τ can be observed at both edges of the detector in Figure 4.1. It

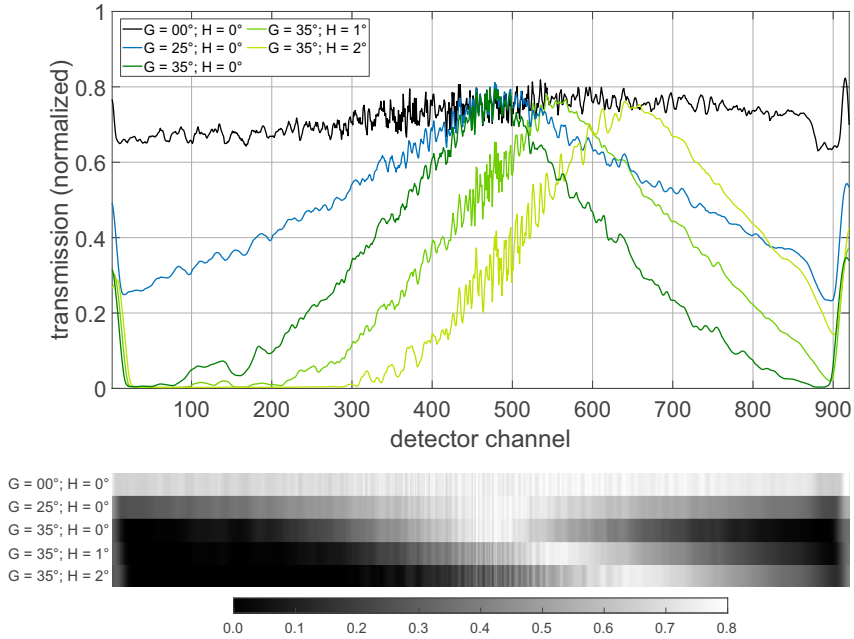

Figure 4.1: Transmission profiles of the sbDBA acquired in experimental measurements. The sbDBA transmission $\tau(\beta)$ is shown across the detector channels (fan beam width) for different angular settings of the attenuation angle G and the shift angle H. The transmission τ is normalized to the signal without any filter in the beam path, compare Eq. 2.1. The upper graph shows the transmission in a line plot, the lower on a gray scale. The horizontal axis (detector channel) is identical. Adapted with permission from Huck et al. (2019).[104]

was recognized that the approximately outermost 20 detector channels were not covered by the sbDBA attenuation sheets, which causes the increase in transmission. Furthermore, a slight asymmetry between both halves of the fan beam can be noticed. The remaining transmission evaluated 250 detector channels apart from each end of the detector, for example, is $\tau_{250}(G = 35°, H = 0°) \approx 0.22$ on the one side and $\tau_{670}(G = 35°, H = 0°) \approx 0.29$ on the other. Likewise, a slight tilt is apparent in the focused position ($G = 35°, H = 0°$). The asymmetry is most likely caused by imperfections of the prototype mounting and by the manual adjustment. Apparently, a high-frequency pattern arises especially at the center of the fan beam width, corresponding to central detector channels. This pattern is attributed to the structuring of the sbDBA along the fan beam width in combination with the geometry of the focal spot: for the central detector channels, the visual appearance of the focal spot is the smallest. Toward more peripheral channels or fan beam rays, respectively, the geometry of the focal spot visually appears larger and distorted due to the change in perspective. Consequently, the “shadow“ of the single attenuation sheets is rather sharply projected onto the detector at central rays whereas it is blurred at peripheral rays. This circumstance makes the calibration procedure and the adjustment more demanding and should be considered for future sbDBA prototype designs.

Figure 4.2 depicts multiple transmission profiles achievable by fluence modulation using the z-sbDBA prototype in experimental measurements. In addition, the transmission profiles acquired from the regular and the narrow bowtie filter are overlaid for comparison. In focused position ($\vartheta = 0°$), the transmission τ is maximum at the center of the fan beam and decreases slightly toward the periphery. This variation is a result of different aspects: first, due to the increasing height of the attenuation sheets toward the edges (max. 4.5 mm), photons can hardly penetrate the attenuation sheets (lead) at the periphery. Second, the transmission at the edges is more sensitive to deviations from perfect alignment and to imperfections of the attenuation sheets that may have occurred during the manufacturing. The higher sensitivity at the edges of the z-sbDBA is a consequence of the aspect ratio (see Section 2.1.2) that increases with higher sheets. Third, the distorted appearance of the focal spot as seen from peripheral detector channels entails a partial defocusing that lowers the transmission. In contrast, a photon propagating along central rays penetrates the minimum residual height (min. 0.5 mm) of an attenuation sheet more likely and is less affected by imperfections (lower aspect ratio). The maximum x-ray transmissivity of the z-sbDBA, corresponding to the maximum transmission achieved, is measured at the central fan beam angles where the attenuation sheets exhibit the minimum extent along the photon propagation direction. The (normalized) x-ray transmissivity is about $\tau_{\max} \approx 0.80$ at $\vartheta = 0.0$ and is hardly affected by the defocusing ($\vartheta \neq 0.0°$). Yet, a minor effect is noticeable due to the minimum residual height of the attenuation sheets. In contrast, the remaining transmission τ at non-central fan beam angles strongly depends on the attenuation angle ϑ and substantially decreases with increasing attenuation angle ϑ. For example at detector channel 220, the remaining transmission declines to $\tau_{220}(\vartheta = 0.6°) = 0.41$, $\tau_{220}(\vartheta = 1.2°) = 0.14$, and $\tau_{220}(\vartheta = 1.8°) = 0.06$, depending on the attenuation angle. Even with a strong attenuation (i.e. large attenuation angle ϑ), a minimum transmission of about $\tau = 0.05$ remains at the periphery and thus photons are not completely absorbed. As apparent from Figure 4.2, the transmission τ declines not exactly symmetrically toward the periphery. Higher detector channel numbers tend to higher transmissions compared to the corresponding detector channels on the other half of the detector. An example for this asymmetry can be seen in the transmission profile associated with $\vartheta = 0.6°$. This is probably due to irregularities of the prototype manufacturing and the mounting.

In comparison to the triangular transmission profiles produced by the sbDBA, the transmission profiles arising from fluence modulation with the z-sbDBA are bell-shaped. Furthermore, the transmissions obtained by the z-sbDBA are comparably smooth across the entire fan beam width, particularly at the center. Another remarkable feature concerns the angular range necessary to achieve the variations of the transmission (i.e., the dynamic range). The sbDBA was tilted by about $G \approx 30°$ while only a few degrees sufficed in the case of the z-sbDBA to achieve a similar attenuation. Considering rotation times of modern CT systems (1 s to 1/4 s),[150] a small angular range is desirable. These benefits are owed to the revised structuring and the design of the z-sbDBA attenuation sheets:

1. The modified alignment of the attenuation sheets along the z axis, as used for the z-sbDBA, virtually circumvents the error-prone structure along the fan beam width,

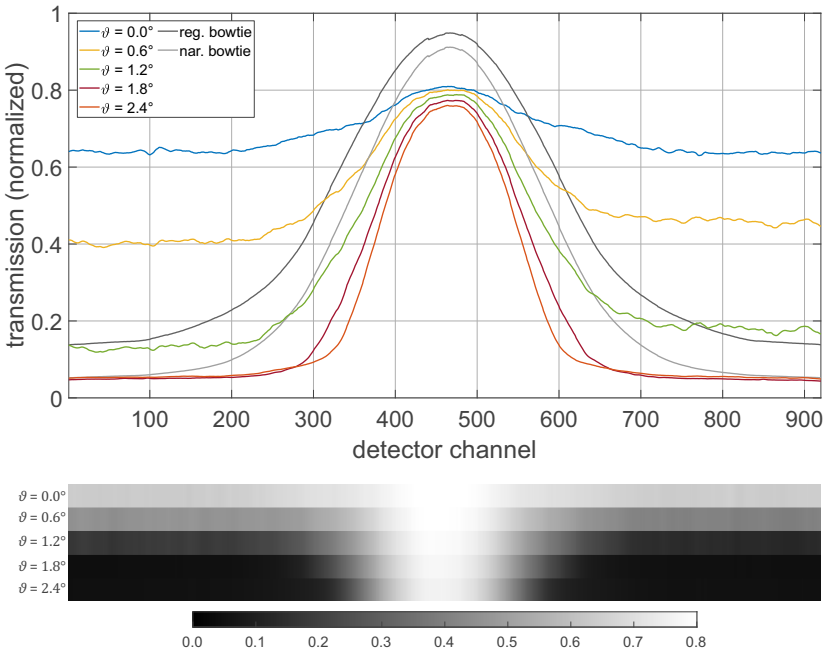

Figure 4.2: Transmission profiles of the z-sbDBA acquired in experimental measurements. The z-sbDBA transmission $\tau(\beta)$ is shown across the detector channels (fan beam width) for different angular settings of the attenuation angle ϑ. The transmission τ is normalized to the signal without any filter in the beam path, compare Eq. 2.1. The upper graph shows the transmission in a line plot, the lower on a gray scale. The horizontal axis (detector channel) is identical. For comparison, the transmission profiles of the regular and the narrow bowtie filter are shown in the line plot. Adapted with permission from Huck et al. (2020).[146]

as represented by the sbDBA. As a result, high-frequency fluctuations of the signal are avoided and the risk of ring artifacts due to mechanical imperfections is mitigated.

2. Furthermore, the shape of the z-sbDBA attenuation sheets allows for smoothly curved transmission profiles that are generally more appropriate for typical CT examinations than triangular profiles (sbDBA).

However, the main limitation of the z-sbDBA in comparison with the sbDBA is its restriction to symmetrical transmission profiles. An increased versatility in transmission profiles might be beneficial depending on the clinical task, as explored in Section 5.2.

Variations along the z axis (off-center fan beam planes)

Figure 4.3 visualizes the transmission τ of the sbDBA and the z-sbDBA at different detector rows (row numbers: 15, 48, and 81) corresponding to different fan beam planes (or image planes) in z direction. Apparently, the transmission slightly changes depending on the z position where the signals are measured. According to Figure 4.3(a), showing the transmission obtained from the sbDBA, the width of the transmission profile is wider at higher detector row numbers. Especially in the 2D plot, one can observe that the transmission varies along the z direction. The leaps in transmission at the edges of the detector are caused by the larger coverage of the fan beam compared to the sbDBA width.

Likewise, the z-sbDBA transmission increases a little toward higher detector row numbers, compare Figure 4.3(b). This effect is more pronounced at the periphery of the fan beam. For example, the remaining transmission at detector channel 200 is about $\tau_{200}(\text{row } 15) = 0.05$ at a lower detector row number, $\tau_{200}(\text{row } 48) = 0.07$ at the central detector row, and $\tau_{200}(\text{row } 81) = 0.10$ at a higher detector row number.

The reason in both DBA cases is that the distance between a specific location on the attenuation sheet and the focus changes when the DBA is tilted around the y axis. In the setups employed, the part of the DBA covering detector rows with higher numbers moves toward the focal spot whereas the other half of the DBA moves away. The described change in distance affects the actual defocusing of the attenuation sheets given by the tilt. The superimposition of both effects implies that depending on the z position one half of the DBA is more strongly defocused while the other half is less affected.

4.2 Spectral dependency of the x-ray transmission

Experimental measurements

The dependency of the transmission on the tube voltage and the associated emission spectrum is shown in Figure 4.4. It compares the relative deviation between the transmission $\tau(U_{low})$ experimentally measured at a lower tube voltage with the transmission $\tau(U_{high})$ that is achieved in the same detector channel when a higher tube voltage is used instead, see Eq. 2.2. This ratio is plotted as a function of the remaining transmission $\tau(U_{low})$, which is chosen as a surrogate for the “strength“ of the fluence modulation. A ratio close

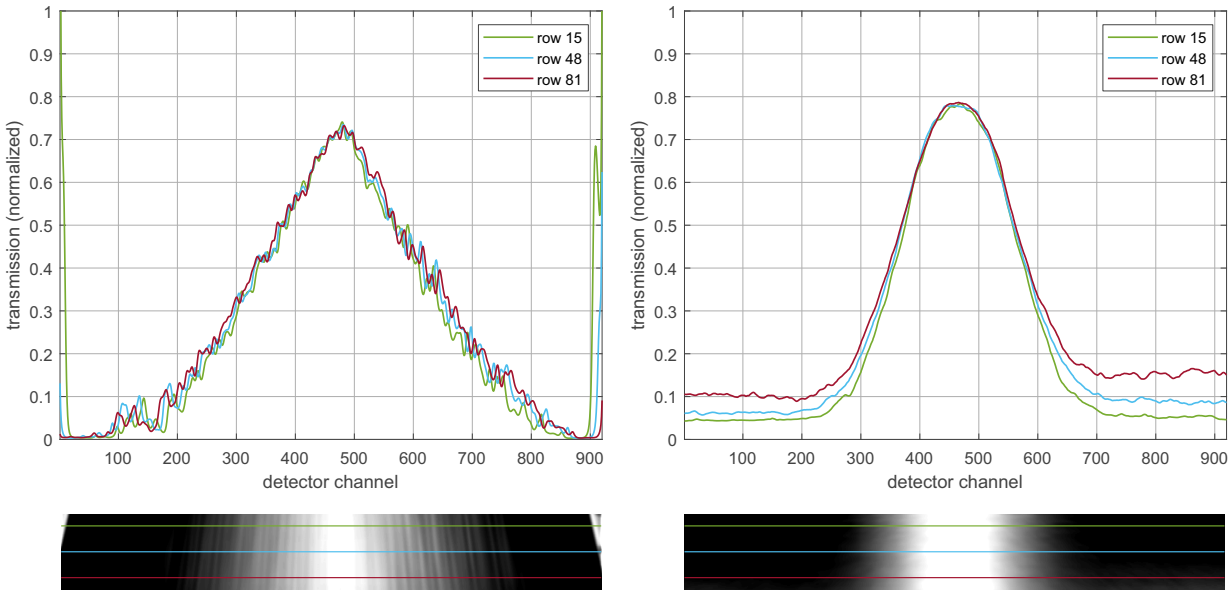

(a) sbDBA (b) z-sbDBA

Figure 4.3: Variations of the experimentally measured transmission τ along the z axis (off-center fan beam planes) for (a) the sbDBA and (b) the z-sbDBA. The upper graphs show the transmission $\tau(\beta)$ across the detector channels (fan beam width) at specific fan beam planes on the z axis, corresponding to the detector row numbers 15, 48, and 81. The lower graphs show the 2D transmission $\tau(\beta, z)$ across the entire detector area (920 channels, 96 rows) and indicate the location of the line plots. The sbDBA was adjusted at $G = 35°$ and $H = 0°$ and the z-sbDBA at $\vartheta = 1.5°$. Adapted with permission from Huck et al. (2019)[104] and Huck et al. (2020).[146]

to 0 represents perfect independence of the transmission from the emission spectrum. The transmissions τ accounted for different photon counts at different tube voltages, as the tube current was constant in all cases and the transmissions were normalized according to Eq. 2.1.

Generally, fluence filters achieve a higher transmissivity at higher tube voltages, which is a consequence of photon interactions with matter, as elaborated in Section 1.2.2. The ratios obtained for the regular and the narrow bowtie filter largely overlap. This is reasonable, as the two bowtie filters differ only in their accumulated thickness, not in their material composition. It is evident from Figure 4.4 that the transmission substantially differs between the emission spectra. Especially with increasing strength of fluence modulation, i.e., toward lower remaining transmission $\tau(U_{high})$, the difference becomes larger as the penetration length through the bowtie filters increases. The transmission $\tau(U_{high})$ at the higher tube voltage is about 100 % higher than at the lower tube voltage at a remaining transmission of $\tau(U_{low}) = 0.1$. At the lowest transmission achievable with the narrow bowtie filter, $\tau(U_{low}) \approx 0.02$, the high-voltage transmission exceeds the low-voltage transmission by 200 %. In comparison, the z-sbDBA reveals a much lower dependency on the emission spectrum although the transmission at the high and the low tube voltage also deviates with increasing strength of fluence modulation. At a remaining transmission of $\tau(U_{low}) = 0.1$, for example, the transmission at the high tube voltage is about 50 % higher. At the lowest transmission achievable with the z-sbDBA, $\tau(U_{low}) \approx 0.02$, the transmission varies by about 100 %. The transmission through the sbDBA appears to be nearly independent of the emission spectrum over a wide range. At a remaining transmission of $\tau(U_{low}) = 0.1$, the relative difference is only about 6 %. Even at a transmission of $\tau(U_{low}) = 0.02$, which represents the minimum transmission attainable with the other fluence filters, the difference is merely 16 %.

Transferring these results to a representation where the transmission is drawn as a function of the fan beam angle $\tau(\beta)$, as used in Figures 4.1 and 4.2, the results imply that the transmissions at low and high tube voltage are similar along central rays (high transmission) but increasingly differ toward larger fan beam angles (low transmission).

The findings show that the z-sbDBA and particularly the sbDBA feature a considerably lower spectral dependency of the transmission compared to state-of-the-art bowtie filters. One reason is that the DBAs are composed of highly x-ray absorbing materials (z-sbDBA: lead; sbDBA: tungsten), while aluminum, as used for the bowtie filters, exhibits a lower linear attenuation coefficient μ (Eq. 1.20). Hence, x-ray photons impinging on the highly attenuating sheets of the DBAs are largely absorbed – almost independent of the photon energy. In contrast, x-ray radiation can generally penetrate through the solid aluminum bowtie filters more easily. Furthermore, the probability of a high-energy photon to penetrate the filters is higher than for a low-energy photon, see Section 1.2.2 and Eq. 1.20. As a result, the deviations rise with stronger fluence modulation (lower remaining transmission $\tau(U_{low})$), an effect that is larger for the bowtie filters and least pronounced for the sbDBA. Another reason for the reduced spectral dependency of the DBAs is their design: the structure of the DBAs resembles the structure of an ASG, as conventionally being

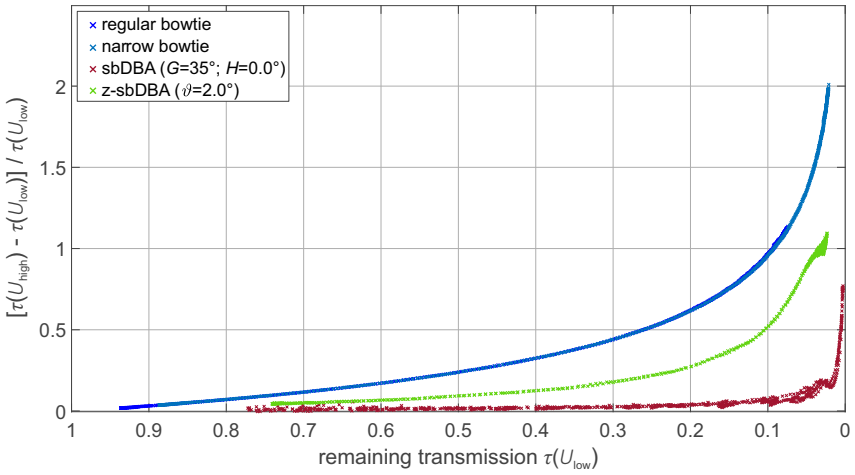

Figure 4.4: The spectral dependency of the transmission in experimental measurements. The (relative) deviation between the transmission measured at a low (U_{low}) and a high (U_{high}) tube voltage U is plotted as a function of the remaining transmission $\tau(U_{low})$ after passing the respective filter, compare Eq. 2.2. A ratio close to 0 indicates perfect independence of the transmission from the emission spectrum or tube voltage, respectively. The angular adjustments of the DBAs represent a strong x-ray attenuation in order to intensify potential differences. Note that the remaining transmission $\tau(U_{low})$, a surrogate for the "strength" of the fluence modulation, is depicted in reverse direction on the x axis.

attached on top of a CT detector, see Figure 1.12. An ASG is a grid whose septa are focused toward the focal spot in order to absorb scatter radiation. Scatter radiation typically deviates from the initial direction of the original primary radiation and thus can be absorbed by the focused septa of the ASG before being detected by the detector. Similarly, the DBAs represent an ASG with the difference that the DBAs are located pre-patient. As a consequence, scatter radiation caused by a scatter event in a DBA attenuation sheet is likely to be reabsorbed by the DBA itself before emanating toward the examination area. Hence, mainly primary photons pass the DBAs while secondary photons are rather absorbed. This ASG-like effect is more pronounced with the sbDBA than with the z-sbDBA, due to the different geometries and compositions. Such a favorable mechanism does not exist for the bowtie filters, though. Accordingly, a larger fraction of secondary photons pass the bowtie filter, resulting in a change of the beam spectrum and eventually of the transmission properties.

4.3 Attenuator-induced secondary radiation

MC-based simulations

As mentioned in the previous section, the interaction of primary x-ray radiation with the fluence filters can induce secondary radiation. The propagation of secondary radiation is an adverse side effect of fluence filtration as it contributes to the patient dose and potentially

impairs the image quality. Thus, the occurrence of secondary radiation emanating from the fluence filter toward the examination area is investigated in this section for the two DBAs and the regular bowtie filter. Therefore, a fan beam irradiating the attenuators was simulated using *MOCASSIM* and the attenuator-induced scatter was scored by an idealized detector located behind. The x-ray transmissions due to the angular adjustments of the DBAs are about the same as the transmission achieved with the regular bowtie filter, see Figures 4.1 and 4.2.

The left column in Figure 4.5 shows the 2D distributions of secondary radiation captured directly behind the respective fluence filter. In addition, the two plots in the right column feature the intensity of attenuator-induced scatter along the horizontal and the vertical axes (corresponding to the fan beam width and the z axis of the CT system), as indicated by the colored lines in the 2D distributions. Along the horizontal axis, the regular bowtie filter causes two prominent peaks close to the center where the intensity of secondary radiation is maximum. The intensity declines toward more peripheral parts of the detector or the fan beam, respectively. The distribution of secondary radiation along the vertical axis is symmetric and peaks in the middle. It is remarkable that by replacing the bowtie filter with one of the DBAs, the intensity of secondary radiation is reduced by about one order of magnitude. Note the different orders of magnitude associated with the gray scales in the 2D distributions. The scatter distribution of the sbDBA also shows a pronounced double peak close to the center. This feature is a result of two competing effects: scattering and self-absorption. At the center of the fluence filter (horizontal axis: 120 mm), there is hardly any material that could scatter at all. Thus, the simulated scatter signal is low. Approximately 30 mm to the sides, there is more material in the beam path so that the scattering increases rapidly and secondary radiation can exit the fluence filters toward the detector. At more peripheral positions, the number of scatter events increases further, but self-absorption by the fluence filter itself predominates in that region. The scatter intensity simulated for the sbDBA obviously differs between the upper an the lower half of the detector. This is a consequence of the large tilt ($G = 25°$) applied in this simulation. As mentioned in Section 4.1, the transmission through the sbDBA varies along the z axis due to the tilt. The z-sbDBA shows only a minor double peak near the center. Generally, the intensity of secondary radiation is comparably flat across large parts of the detector in horizontal direction and decreases slightly toward the periphery. Similar to the sbDBA, an asymmetrical modulation along the z direction is observed for the z-sbDBA because of the tilt ($\vartheta = 1.0°$). Primarily, the spatial distribution differs between both DBA concepts while the overall amount of scatter radiation is comparable and substantially lower than that of the bowtie filter.

These computational investigations on attenuator-induced scattering emphasize what has been experimentally deduced in the previous section on the spectral dependency of the transmission (Section 4.2). As elaborated in that section, the reasons for the improved properties of the DBAs can be found in the beneficial structuring and material composition of the DBAs. Compared to the aluminum bowtie filters, the ASG-like structure of the DBAs effectively reduces scatter radiation toward the examination area by about one

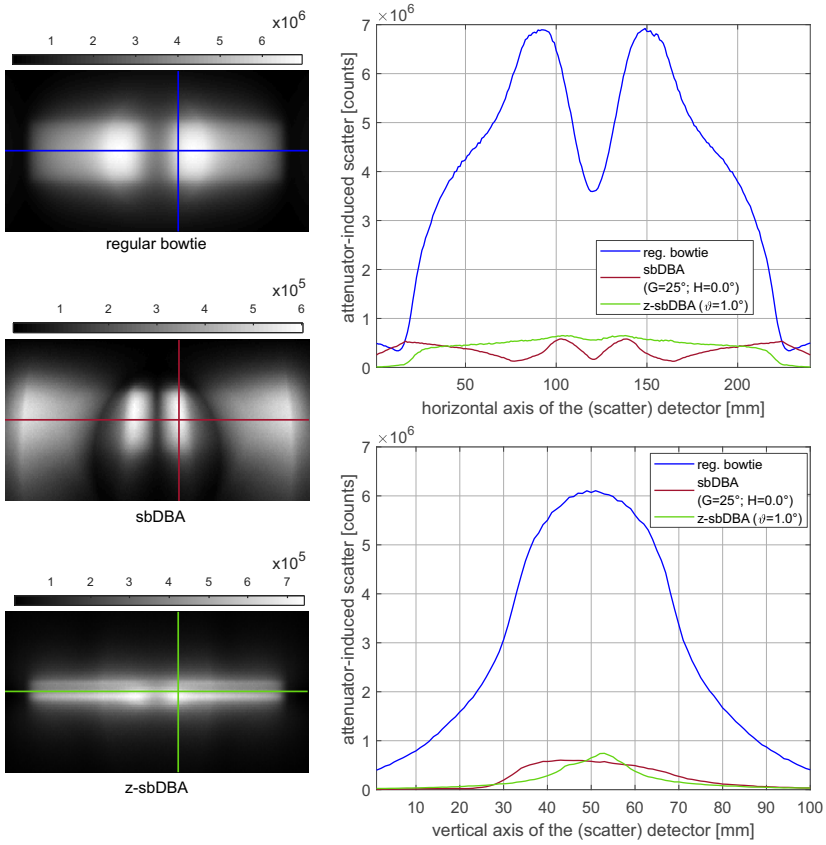

Figure 4.5: Attenuator-induced secondary radiation (MC-based simulations). The left column shows the 2D distributions of exclusively secondary radiation scored by an ideal detector directly behind the regular bowtie filter (top), the sbDBA at $G = 25°$ and $H = 0.0°$ (middle), and the z-sbDBA at $\vartheta = 1.0°$ (bottom). Note the different orders of magnitude associated with the gray scales. A total of 10^{10} photons were simulated in each case. To provide roughly the same conditions, the x-ray transmissions due to the DBA adjustments approximately match the transmission achieved with the regular bowtie filter. For comparison, the x-ray transmissions are depicted in Figures 4.1 and 4.2. The right column shows the intensity of the attenuator-induced scatter along the horizontal (top) and the vertical (bottom) lines, as indicated in the 2D distributions. The horizontal axis of the 2D (scatter) detector corresponds to the fan beam width and the vertical axis corresponds to the z axis of the CT system. Adapted and extended with permission from Huck et al. (2019).[104]

order of magnitude. Accordingly, the fraction of primary compared to secondary photons impinging on the examined object is considerably improved by using the DBAs. Hence, an examined patient is exposed to less scatter radiation when being imaged with a DBA, which eventually improves the patient radiation dose. Moreover, image quality (e.g., image contrast) can generally be enhanced when scatter radiation is diminished, especially in dual source CT imaging.[25,102,152,153] Even if not specifically investigated in this work, it can be assumed that also the adverse effect of extrafocal radiation can substantially be mitigated by using a DBA. Similar to scatter radiation, extrafocal radiation, which emanates from parts of the anode disk other than the focal spot, impairs image quality and patient dose.[48,174]

4.4 Image reconstruction

Experimental measurements

The mechanical robustness and the angular reproducibility of the DBA prototypes is a crucial aspect of a movable fluence filter as small discrepancies can cause image artifacts. Thus, the sensitivity to mechanical deviations is explored in first-time image reconstructions of a phantom using the DBA prototypes, as depicted in Figure 4.6.

The reconstructed image acquired with the sbDBA, Figure 4.6(a), shows a 30 cm water phantom. Although a reasonable image reconstruction of the object is obtained, some ring artifacts arise at the edges of the phantom. This indicates that the attenuation angle G adjusted in the calibration and the phantom measurement did not match exactly. An angular mismatch mainly affects the transmission at the periphery of the fan beam where the DBA's aspect ratio is higher in defocused alignments ($G \neq 0°$, $H = 0.0°$), corresponding to the outer part of the phantom in the reconstructed image. Alternatively, some peripheral attenuation sheets could have moved between the two measurements, which would cause the same effect. Given the method the angular adjustment was conducted, compare Section 2.2.2 and Section 2.3.4, the result is not surprising but rather encouraging: intentionally, there was a time gap of several hours between the calibration and the phantom measurement. In addition, the sbDBA was moved between both measurements to evoke potential mechanical deviations and assess the sensitivity to such effects. Moreover, the angular adjustment was performed manually.

Figure 4.6(b) depicts the reconstructed images obtained from the z-sbDBA prototype. It is composed of two partial images: the left half of the image shows one half of the reconstructed CTDI phantom (Section 2.3.4) at a slight fluence modulation ($\vartheta = 1.0°$). The right half of the image exhibits the measurement at a strong fluence modulation ($\vartheta = 2.0°$). The acquisition with slight fluence modulation returns a nearly artifact-free image of the CTDI phantom without strong textures. The measurement acquired with strong fluence modulation reveals some disturbances, though. Evaluations show that the mean HU value – averaged across the entire phantom (PMMA) – is roughly the same in both halves of the image (approx. 100 HU). While the left image is comparably flat, the HU values in the right image are higher at the center (approx. 135 HU) and lower at the edges (approx. 80 HU). Especially somewhat outside the 16 cm insert, the HU values decline (darker gray values).

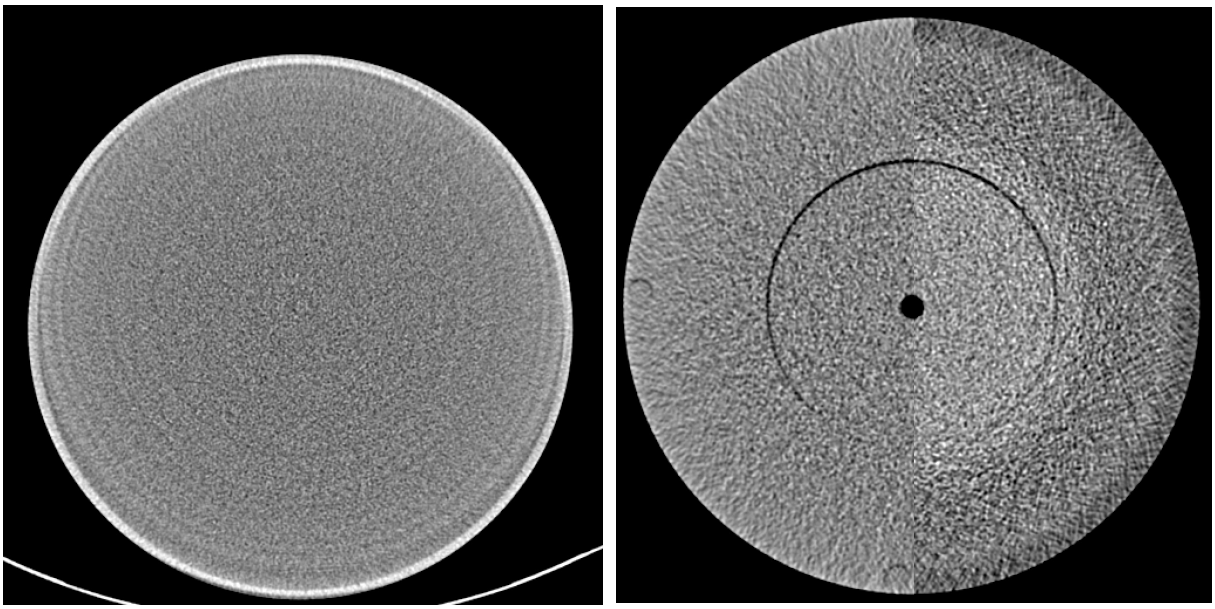

(a) (b)

Figure 4.6: Image reconstructions using the DBA prototypes in experimental measurements. (a) The reconstructed image of a 30 cm water phantom using the sbDBA adjusted at $G = 35°$ and $H = 0.0°$. Windowing: center = 0 / width = 400. This image reconstruction has previously been presented in Huck (2017).[17] (b) The (vertically splited) reconstructed image of a 32 cm CTDI phantom (PMMA) using the z-sbDBA adjusted at $\vartheta = 1.0°$ (left half) or at $\vartheta = 2.0°$ (right half). The black circle in the center represents an empty dose cavity and the black ring is due to a 16 cm insert. Windowing: center = 100 / width = 400. The image reconstructions used different FOVs. Modified or reproduced with permissions from Huck (2017),[17] Huck et al. (2019),[104] and Huck et al. (2020).[146]

Apparently, the attenuation measured in the phantom scan was slightly higher in the center and lower in the periphery compared to the calibration. As the properties of the CT system were unchanged, the results indicate that mechanical deviations of the z-sbDBA prototype caused different transmission properties. This seems most likely due to the acquisition process: deviations of the experimental setup had intentionally been provoked by the time gap and by changing the angular setting between the two measurements in order to evaluate the sensitivity of the prototypes.

The two image halves in Figure 4.6(b) feature another remarkable aspect of the z-sbDBA usage: the noise texture in the periphery of the phantom is less isotropic compared to the noise texture at the center. This is expected as the z-sbDBA strongly reduces the x-ray fluence toward the edges of the phantom. The ring where the texture is stronger – roughly matching with detector channels lower than 290 and higher than 630 in the sinogram – approximately corresponds to regions where the transmission is largely reduced, as shown in Figure 4.2. A similar, but less pronounced effect is observed in the case of the sbDBA, as well. The change in texture, however, does not necessarily represent an image artifact but

results from the fluence modulation. In ROI imaging, as explored in Chapter 5, one specifies diagnostically relevant regions where the image quality (e.g., image noise) is supposed to be maximized. In surrounding regions, in contrast, the image quality is not relevant but an attempt is made to minimize the radiation dose. As a result, one aims for image reconstructions as depicted in Figure 4.6, where only a specific part exhibits a high image quality and in turn radiation dose can be spared elsewhere.

Chapter conclusion This chapter demonstrated the general feasibility of FFM using the presented DBA concepts. The proof-of-concept was conducted using DBA prototypes mounted on a clinical CT system. The z-sbDBA prototype was particularly mature. After integration, it was possible to completely reassemble the CT system and close the front cover such that no visible modifications were recognizable from the outside. A wide range of transmission profiles – from almost constant across the fan beam width to highly dynamic – was achieved by both DBAs. While the sbDBA allowed to shape the transmission profiles more flexibly, in particular by laterally shifting the peak transmission, the z-sbDBA realized more appropriate shapes for CT imaging. The revised z-sbDBA structuring eliminated the high-frequency fluctuations of the sbDBA transmission effectively and produced much smoother profiles instead. A variation of the transmission along the z axis was noticed, which should be addressed by appropriate calibrations. Such variations are not unknown in CT: tube aging or the so-called heel effect are also known to alter the x-ray fluence along the z direction due to self-absorption.[19] The comparisons regarding the spectral dependency and the attenuator-induced scatter revealed that the z-sbDBA and in particular the sbDBA possess characteristics of an ASG. Accordingly, the transmission was considerably less dependent on the applied tube voltage compared to a conventional bowtie filter. Moreover, secondary radiation emanating from the attenuator toward the examination area was reduced by about one order of magnitude when using one of the DBAs instead of the bowtie filter while realizing a comparable x-ray transmission. Both features of the DBAs ease the image acquisition process and improve the image quality, eventually. First-time image reconstructions from data acquired with the DBA prototypes unveiled the major challenge of movable x-ray fluence filters: some ring artifacts in the reconstructed images were most likely related to mechanical imperfections during data acquisition. An intentional time gap and angular readjustments between the calibration and the measurement, however, were introduced to challenge such issues. Thus, considering the data acquisition method and that first DBA prototypes – representing highly structured objects – were placed in the beam path of a clinical CT system for the first time, the overall image quality was encouraging.

Chapter 5

Results & Discussion – Part II: Application and evaluation of DBAs in ROI imaging

In the previous Chapter 4, a proof-of-concept demonstrated that the proposed DBA prototypes allow for modulating the propagated x-ray fluence. As a natural next step, the question of how to optimally move the DBAs was pursued in order to provide the most dose efficient x-ray fluence for a given imaging task. Accordingly, this chapter focuses first on the optimized operation and second on the clinical benefit of the DBAs.

At the beginning of this chapter, Section 5.1, the proposed trajectory determination method is employed to optimize the x-ray fluence $\tau(\alpha, \beta)$ through the DBAs for a given imaging task. The method determines the optimal DBA angles (G and H, or ϑ) as a function of the projection angle α such that the dose efficiency is maximized. TCM according to Eq. 3.1 is included in the algorithm. The dose efficiency is described by the ROI image quality and the patient radiation dose, as represented by the introduced optimization criterion, see Eq. 3.3. The trajectory determination method is shown on three exemplary ROI imaging tasks, including a water phantom and a model of a heterogeneous female thorax.

In the second part, Section 5.2, the DBA concepts are compared with existing FFM technologies in terms of their potential for ROI imaging. The comparison includes TCM according to the hsqTCM method (Eq. 3.1) and two conventional bowtie filters as being part of a clinical CT system. In addition to a quantitative comparison assessing the dose efficiency (with respect to the optimization criterion), the comparison is extended by a qualitative evaluation visualizing the resulting 2D dose deposition maps (Eq. 3.5). Moreover, the NPS isotropy of the final image reconstructions is analyzed to ensure that the noise texture in the variance-equalized images does not suffer from FFM.

Parts of the results presented in this chapter have been published in a journal article, Huck et al. (2021),[158] and have been presented at a scientific conference, Huck et al. (2020).[159] The content is reproduced with permission.

5.1 DBA trajectory determination for optimized FFM

5.1.1 Imaging task I: Elliptical water phantom with central ROI

The proposed trajectory determination method is first applied on the comparably simple imaging task I: an elliptical water phantom (homogeneous), which accommodates an elliptical ROI at its center. Figure 5.1 shows the DBA angles obtained by the trajectory optimization method. As apparent from Figures 5.1(a) - 5.1(c), primarily the width of the sbDBA transmission profile is adapted during the rotation ($G \neq$ const.), while the peak transmission remains centered ($H \approx$ const.). The resulting transmission of the sbDBA reflects the geometry and location of the ROI: comparably narrow transmission profiles – corresponding to a larger attenuation angle G – are considered at the lateral projections (α about 0°, 180°, and 355°). In contrast, broader profiles – corresponding to a smaller attenuation angle G – are found at a/p projections (α about 90° and 270°). The shift angle H is largely unchanged due to the central location of the ROI. Only minor deviations from the centered adjustment ($H = 0.0°$) are noticed at a few projection angles, e.g., at $\alpha = \pm 200°$. These irregularities might result from imperfections of the MC-based transmission profiles (e.g., photon statistics, symmetry along the fan beam width) that were used for the sbDBA optimization.

The transmission optimized for the z-sbDBA shows similar characteristics, as depicted in Figures 5.1(d) and 5.1(e). In lateral directions, larger attenuation angles ϑ, resulting in narrower transmission profiles, are determined. At few lateral projections, the maximum available attenuation angle, $\vartheta_{max} = 2.2°$, is obtained. In a/p directions, in turn, smaller attenuation angles, causing broader transmission profiles, are returned by the trajectory optimization.

In the adjustable static mode of the z-sbDBA, which keeps the attenuation angle – and thus transmission through the z-sbDBA – constant during the acquisition, the optimization method determines $\vartheta = 1.9°$ as the most dose efficient adjustment, see Figure 5.1(e).

Generally, the optimization method returns smooth, cyclic trajectories (applicable to sbDBA and z-sbDBA) that account for the symmetry and the varying width of the ROI described by the imaging task.

5.1.2 Imaging task II: Female thorax with off-centered heart ROI

A more complex diagnostic aim is described by imaging task II: it considers the imaging of an off-centered heart ROI within a heterogeneous female thorax. The associated DBA trajectories determined are portrayed in Figure 5.2. Unlike the trajectory obtained for imaging task I, where primarily the width of the transmission profile is modulated, in this imaging task the sbDBA predominantly adapts the propagated fluence by laterally shifting the peak transmission. As evident from Figures 5.2(a) - 5.2(c), the peak transmission is far shifted across the fan beam width in order to "trace" the off-centered ROI ($H \neq$ const.). The width of the transmission profiles, in contrast, remains almost unchanged during the rotation ($G \approx$ const.) as the diameter of the ROI appears similar from different projections.

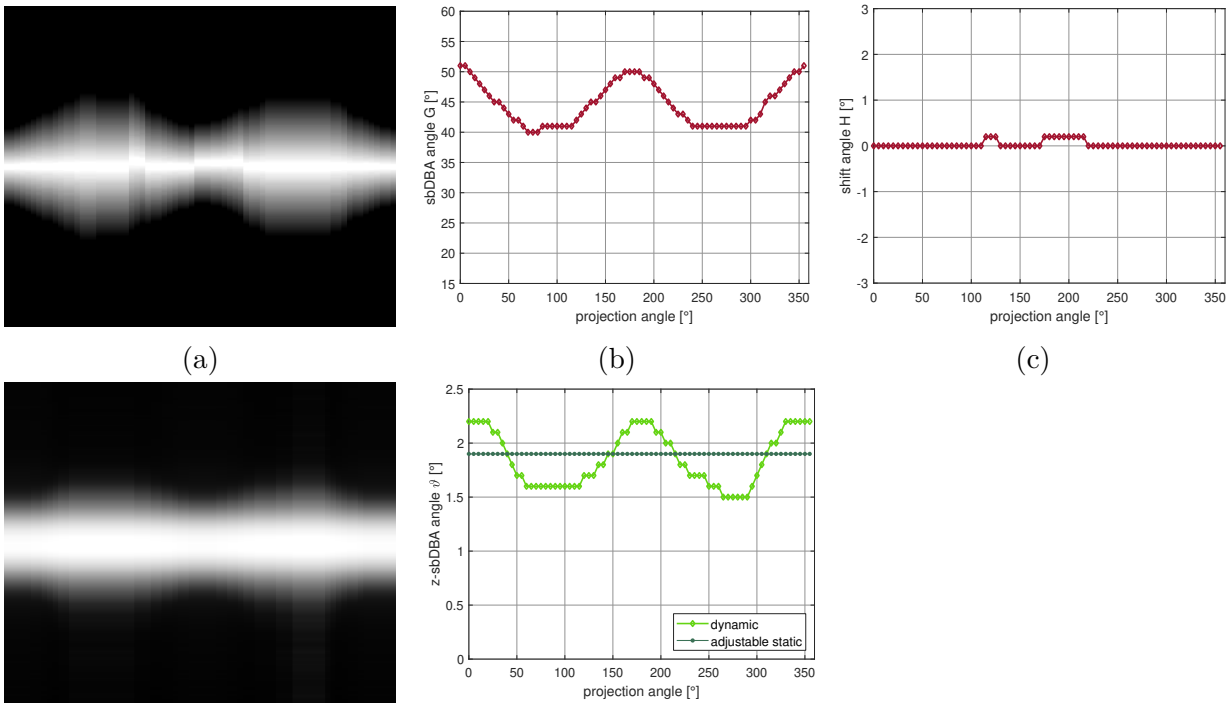

Figure 5.1: DBA transmission and trajectory obtained from the optimization method for imaging task I (elliptical water phantom with central ROI). The upper row shows the results for the sbDBA, the lower one for the z-sbDBA. Panels (a) and (d) visualize the optimized DBA transmission $\tau(\alpha, \beta)$ corresponding to the determined DBA trajectory. A brighter gray level corresponds to a higher photon count (windowing: center = 0.5 / width = 0.9). The contribution of TCM is not included in this visualization. Horizontal: projection angle α; vertical: fan beam angle β. Panels (b) and (e) depict the attenuation angles of the sbDBA (G) and the z-sbDBA (ϑ: for both operation modes). Panel (c) depicts the shift angle of the sbDBA (H). Reproduced with permission from Huck et al. (2021).[158]

The transmission through the z-sbDBA, depicted in Figures 5.2(d) and 5.2(e), differs substantially from the transmission obtained for the more flexible sbDBA. Unlike the sbDBA, the z-sbDBA cannot trace the off-centered location of the ROI during the gantry rotation because it is restricted to symmetrical transmission profiles by construction. Accordingly, for projections where the ROI appears at off-center fan beam angles, the z-sbDBA can only deliver sufficient photons toward the ROI by increasing the width of the transmission profile. This explains why broader transmission profiles (smaller attenuation angle ϑ) are determined in lateral directions (α about 0°, 180°, and 355°). At a/p projections, the heart ROI appears at the center of the fan beam. Therefore, it seems plausible that the optimization method yields narrow transmission profiles (larger attenuation angle ϑ) at these projection angles. At some projections from the back of the phantom, the maximum attenuation angle ϑ_{max} is reached. Consequently, only the heart ROI is imaged at a high fluence while non-ROI tissue (e.g., lung or breast tissue) is spared from unnecessary radiation.

The female thorax phantom features a symmetry axis along its a/p direction, see Figure 3.1(b). This characteristic is approximately reproduced by the DBA trajectories. However, some deviations occur if one regards the course of the z-sbDBA trajectory at $\vartheta = \pm 90°$ versus $\vartheta = \pm 270°$ in Figure 5.2(e).

In the case of the adjustable static z-sbDBA, the optimization method determines the attenuation angle $\vartheta = 1.9°$ as the angle that delivers the optimal fluence during the entire acquisition, see Figure 5.2(e).

The DBA trajectory optimization method addresses the requirements of the imaging task by adapting the lateral position (sbDBA) or the width (z-sbDBA and adjustable static z-sbDBA) of the transmission profile accordingly.

5.1.3 Imaging task III: Off-centered female thorax with centered heart ROI

This imaging task describes the same situation as in the previous imaging task II with the only difference that the entire thorax is moved up a little such that the heart ROI is located at the CT isocenter. This modification is readily visible from the transmission optimized for the sbDBA, compare Figures 5.2(a) - 5.2(c) with Figures 5.3(a) - 5.3(c). Unlike the varying shift angle H in imaging task II, the shift angle in this imaging task is hardly varied across the gantry rotation ($H \approx 0.0°$). The attenuation angle G that adapts the width of the transmission profile to the diameter of the ROI is almost constant during the acquisition in both imaging tasks. It fluctuates slightly around a highly collimating angle such that the heart ROI is exposed to a high x-ray fluence while the non-ROI tissue is spared. Consequently, the width of the transmission profiles (G) is similar in both imaging tasks, only the appearance of the peak transmission (H) is different in order to capture either the centered or the off-centered ROI, respectively.

Figures 5.3(d) and 5.3(e) portray the resulting trajectory obtained for the z-sbDBA. It is remarkable that the attenuation angle ϑ and thus the width of the transmission hardly

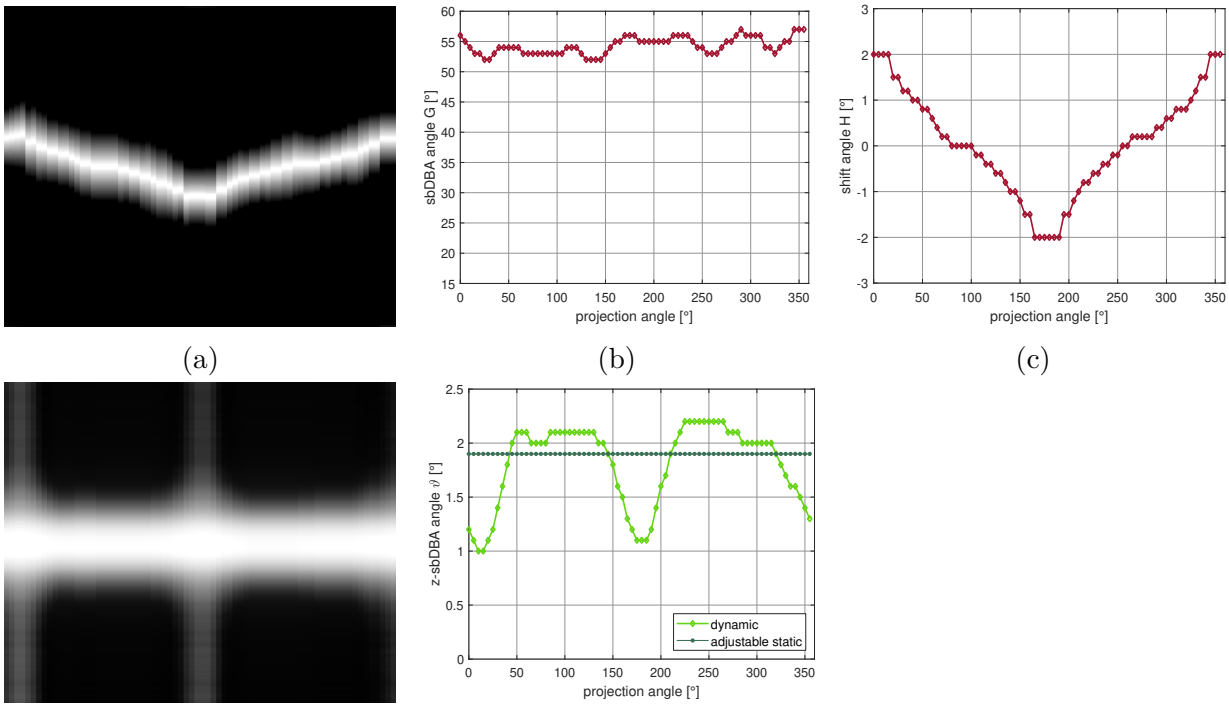

(a) (b) (c)

(d) (e)

Figure 5.2: DBA transmission and trajectory obtained from the optimization method for imaging task II (female thorax phantom with off-centered heart ROI). The upper row shows the results for the sbDBA, the lower one for the z-sbDBA. Panels (a) and (d) visualize the optimized DBA transmission $\tau(\alpha, \beta)$ corresponding to the determined DBA trajectory. A brighter gray level corresponds to a higher photon count (windowing: center = 0.5 / width = 0.9). The contribution of TCM is not included in this visualization. Horizontal: projection angle α; vertical: fan beam angle β. Panels (b) and (e) depict the attenuation angles of the sbDBA (G) and the z-sbDBA (ϑ: for both operation modes). Panel (c) depicts the shift angle of the sbDBA (H). Reproduced with permission from Huck et al. (2021).[158]

changes during the rotation. The attenuation angle fluctuates around $\vartheta \approx 2.1°$. These variations ($\Delta\vartheta \approx 0.3°$) are much smaller than the variations observed in the previous imaging task II ($\Delta\vartheta > 1.0°$) where the ROI appears also at off-center fan beam angles. The centering of the ROI allows the z-sbDBA to largely reduce the photon count toward peripheral non-ROI tissue while exposing the heart ROI to the peak transmission. When using the adjustable static z-sbDBA, the optimization method returns the maximum attenuation angle $\vartheta_{max} = 2.2°$ in this imaging task, see Figure 5.3(e).

Discussion & summary

Summarizing the results on the DBA fluence optimization, the discrete coordinate descent method, employed to determine and to optimize the DBA trajectories, delivers smooth and cyclic trajectories that are reasonable considering the geometries in the respective imaging tasks. It should be noted that the trajectory determination method is not applicable to clinical practice and was not designed for clinical purposes in the first place. First of all, the method assumed *a priori* knowledge about the attenuation properties of the phantoms that is, of course, not available in reality. Furthermore, the computational time of several hours to determine the trajectories would exceed the available time for CT examinations by far. Instead of the clinical suitability, the focus of this method was to combine a precise dose estimate with a reasonable measure for image quality in the DBA optimization. Algorithms for the future clinical application, in contrast, should enable the determination of the movement of a DBA in real-time. In literature, algorithms that are based on, e.g., the data of previous projections have been proposed in the context of alternative DBA concepts.[114,135,141,175] Another approach suitable in daily routine is to refer to a set of pre-defined trajectories, comparable to what has been suggested by Szczykutowicz and Hermus (2015).[176] The authors describe an atlas consisting of a finite number of filter configurations that practically cover all relevant fluence profiles required for divers imaging tasks (different patient anatomies, body regions, patient positions etc.). Moreover, a machine learning based approach is conceivable to determine the DBA trajectory. It could exploit the data of a 3D camera or localizer radiographs (also: CT topograms), which are acquired before the actual CT examination. Both sources of information are already part of modern CT systems and provide information about the patient position and the patient x-ray attenuation, which is used to support the CT examination planning.

Evidently, the sbDBA is able to precisely adjust the fluence transmission to the considered imaging task. The optimization method exploits the wide range of transmission profiles provided by the sbDBA. It is worthwhile to note that depending on the ROI geometry, the optimization method adapts the sbDBA transmission to i) a changing ROI cross-section by adjusting the attenuation angle G (e.g., imaging task I, Figure 5.1(b)) and ii) a changing ROI location by adjusting the shift angle H (e.g., imaging task II, Figure 5.2(c)). Thus, the transmitted fluence reflects the geometrical properties (i.e., the location and the cross-section) of the specified ROI.

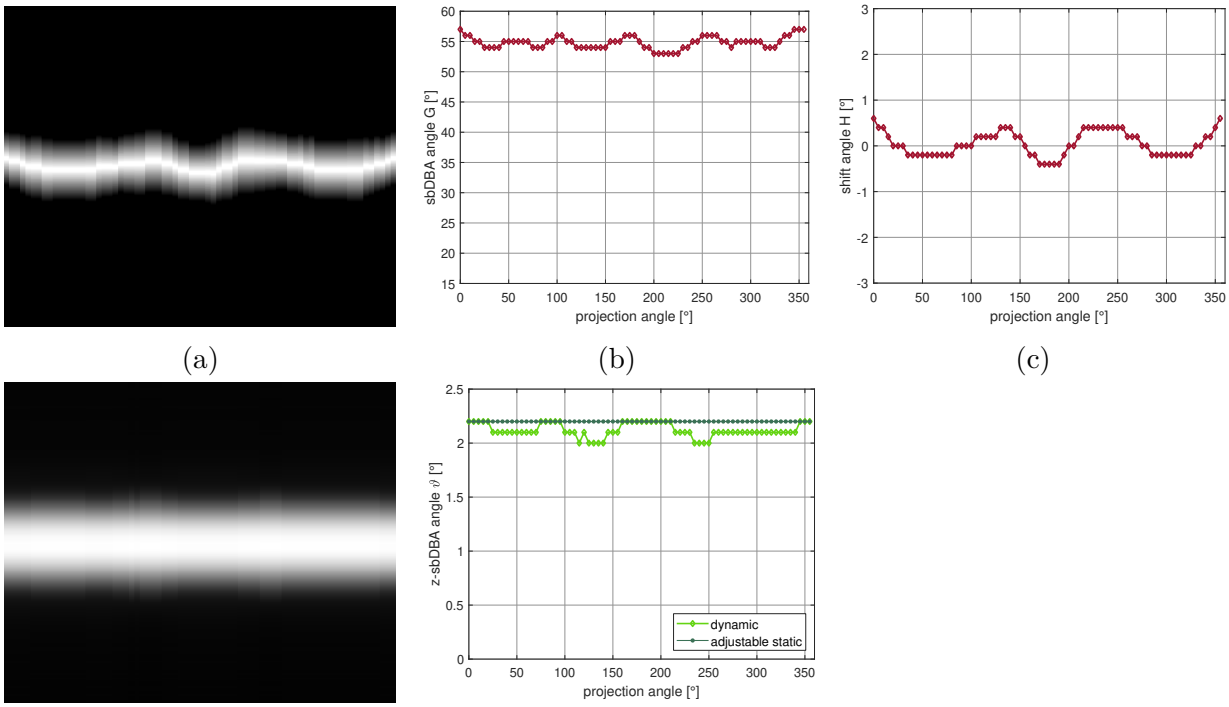

Figure 5.3: DBA transmission and trajectory obtained from the optimization method for imaging task III (off-centered female thorax phantom with centered heart ROI). The upper row shows the results for the sbDBA, the lower one for the z-sbDBA. Panels (a) and (d) visualize the optimized DBA transmission $\tau(\alpha, \beta)$ corresponding to the determined DBA trajectory. A brighter gray level corresponds to a higher photon count (windowing: center = 0.5 / width = 0.9). The contribution of TCM is not included in this visualization. Horizontal: projection angle α; vertical: fan beam angle β. Panels (b) and (e) depict the attenuation angles of the sbDBA (G) and the z-sbDBA (ϑ: for both operation modes). Panel (c) depicts the shift angle of the sbDBA (H). Reproduced with permission from Huck et al. (2021).[158]

Generally, the z-sbDBA trajectories correspond to the geometries of the considered imaging tasks. It is noticeable, however, that the adaptation of the fluence transmission by the z-sbDBA is not as precise as it can be achieved by the sbDBA. In particular when imaging off-centered ROIs (e.g., imaging task II, Figure 5.2), the limitation to exclusively symmetrical transmission profiles is disadvantageous compared to the higher flexibility of the sbDBA. In such cases, the trajectory optimization needs to balance between image quality inside the ROI and dose penalties from non-ROI tissue. Therefore, an increase in ROI image quality can only be realized by an excess of radiation dose in surrounding tissue. The trajectory obtained for the z-sbDBA in imaging task II does not exactly reflect the symmetry of the phantom, which is evident from the not perfectly cyclic trajectory depicted in Figures 5.2(d) and 5.2(e). These deviations are caused by the irregular shape of the z-sbDBA transmission profiles, which are shown not to be perfectly symmetrical, compare Figure 4.2. The transmission between both ends of the fan beam differs particularly toward peripheral fan beam angles. At only few projection angles, the maximum available attenuation angle ϑ_{max} is prescribed by the trajectory optimization. It seems neither necessary nor meaningful to consider even larger attenuation angles in the optimization. The measurements of the z-sbDBA transmission profiles revealed that the shape does not change considerably at even higher attenuation angles, see Figure 4.2. Rather, a change in the shape of the attenuation sheets might provide an advantage as suggested in Section 6.2. It is interesting to note that the attenuation angle identified for the adjustable static z-sbDBA approximately matches the arithmetic mean of the z-sbDBA attenuation angles $\langle\vartheta(\alpha)\rangle$ in the considered imaging tasks.

In conclusion, the trajectory optimization method allows to determine appropriate DBA trajectories that address the specific requirements of the imaging task. The trajectories obtained are the basis for the ROI comparison presented in the subsequent Section 5.2.

5.2 Comparing the potential dose reduction by ROI imaging using different FFM configurations

The potential of ROI imaging using different methods for FFM is investigated in this section. To this end, the feasibility of the considered FFM configurations to modulate the propagated x-ray fluence according to the given imaging tasks is compared. The FFM configurations regarded in this evaluation are described in Table 3.1, no.1 to no.7, and the imaging tasks are explained in Section 3.1. This comparison assesses the radiation exposures of the FFM configurations in terms of their dose efficiency, spatial dose distribution, and NPS isotropy at equalized image quality. The FFM configuration no. 1, emitting an unmodulated primary fluence (no fluence filtration, no TCM), is considered as the reference configuration.

5.2.1 Imaging task I: Elliptical water phantom with central ROI

The dose efficiency of the investigated FFM configurations obtained for imaging task I is listed in the third column of Table 5.1. It compares the effective dose δ deposited in the phantom to realize the same ROI image quality σ^2_{ROI}. In this imaging task, where an elliptical water phantom (homogeneous) with central ROI is employed, the radiation dose can be lowered to a level of 60 % (no. 2) relative to the reference dose (no. 1) by enabling TCM. The additional use of a bowtie filter can further reduce the phantom dose to 44 % with the regular (no. 3) or even 41 % with the narrow bowtie filter (no. 4). Employing the z-sbDBA instead achieves further dose reductions, 36 % (no. 6) or 38 % (no. 7). This corresponds to an improvement of about 1/6 compared to the state-of-the-art regular bowtie filter (no. 3). When using the sbDBA (no. 5), 32 % of the radiation dose required in the reference case is sufficient to achieve the same ROI image quality.

The NPS isotropy score ϵ_{NPS} is listed in the fourth column of Table 5.1. It is used as a measure to monitor that image noise texture is not impaired by FFM and the associated dose savings. The NPS isotropy score $\epsilon_{\mathrm{NPS}} = 1$ represents perfect noise isotropy, while a score close to $\epsilon_{\mathrm{NPS}} = 0$ reveals anisotropic noise. The NPS isotropy score of the reference FFM configuration (no. 1), when no fluence modulation is applied at all, is the lowest among the considered cases ($\epsilon_{\mathrm{NPS}} = 0.27$). The use of TCM (no. 2) can greatly enhance the noise isotropy ($\epsilon_{\mathrm{NPS}} = 0.43$). Although the investigated x-ray fluence filters are capable of further reducing the patient radiation dose, it is evident that the noise isotropy ($\epsilon_{\mathrm{NPS}} \approx 0.45$) does not suffer from the additional dose savings – irrespective of whether a bowtie filter or a DBA is used.

These findings are in accordance with the spatial dose depositions (absorbed dose) visualized in Figure 5.4. It should be noted that a logarithmic scale was used to visualize the 2D dose maps due to large differences in the local dose values between the FFM configurations. The peripheral non-ROI tissue (outside the dashed ellipses in the dose maps) is diagnostically not relevant in this imaging task and thus should be spared from unnecessary radiation. Nevertheless, the periphery of the object is exposed to a very high x-ray fluence in configurations without in-beam fluence filtration, i.e., configuration no. 1 and no. 2. Accordingly, the dose deposition in non-ROI tissue is comparably high, as shown in Figures 5.4(a) and 5.4(b). The fluence modulations facilitated by the bowtie filters, particularly the narrow bowtie filter, redistribute the radiation exposure and yield dose savings in peripheral tissue, see Figures 5.4(c) and 5.4(d). The z-sbDBAs adapt the propagated fluence even more effectively such that the dose deposition in non-ROI tissue further decreases, compare Figures 5.4(f) and 5.4(g). It is worth noting that the sbDBA is able to deposit a lower dose in peripheral tissue compared to the ROI, as apparent from Figure 5.4(e) and from the associated line plot in Figure 5.4(h). The line plots do not only demonstrate the spatial distribution of the local dose deposition, they further provide a visual and quantitative impression of the dose reductions achievable by the individual FFM configurations. Apparently, a large benefit is yielded by TCM, which is further enhanced by the usage of a fluence filter.

Table 5.1: Overview of the dose efficiency achieved by different FFM configurations for imaging task I (elliptical water phantom with central ROI). Third column: the effective dose δ caused in the homogeneous water phantom, necessary to achieve a prescribed level of image quality (ROI image variance σ^2_{ROI}). The dose values are normalized to the reference scenario no. 1. Fourth column: the NPS isotropy score ϵ_{NPS} calculated inside the ROI (perfect isotropy: $\epsilon_{\mathrm{NPS}} = 1.00$).[167]

no.	FFM configuration (key)	effective phantom dose δ (normalized)	NPS isotropy score ϵ_{NPS}
1	*noAtt_tcm0*	1.00	0.27
2	*noAtt_tcm1*	0.60	0.43
3	*reg_bowtie_tcm1*	0.44	0.44
4	*nar_bowtie_tcm1*	0.41	0.45
5	*sbDBA_tcm1*	0.32	0.44
6	*zsbDBA_tcm1*	0.36	0.45
7	*as_zsbDBA_tcm1*	0.38	0.46

Figure 5.5 visualizes the corresponding image reconstructions and variance maps produced with the FFM configurations. According to the methodology applied, the image variance inside the ROI σ^2_{ROI} is equalized between the configurations. Thus, the reconstructed images are very similar inside the ROI except for the case without any modulation (no. 1). In that configuration, a more intense pattern of horizontal streaks is visible inside the ROI. The more pronounced texture is also reflected by the low NPS isotropy score, as given in Table 5.1. This example emphasizes the importance of the NPS isotropy as an additional quantity for image quality. It can reveal image artifacts that are not represented by the mean image variance due to the equalization. By employing TCM, the noise pattern almost vanishes within the ROI, irrespective of any fluence filter. It is interesting to note that the image outside the ROI shows very strong artifacts when using the sbDBA, as shown in Figure 5.5(e). This is a result of the strong reduction in x-ray fluence at larger fan beam angles, as elaborated in Section 5.1.1. The pronounced image artifacts, however, are not critical because i) the peripheral part of the image is not diagnostically relevant in this imaging task and ii) the x-ray fluence is still sufficient so that the image reconstructions do not encounter data truncation issues. This characteristic is also revealed in the variance map associated with the sbDBA. While the image variance inside the ROI is similar to other FFM configurations, it rapidly raises outside. In configurations using the z-sbDBA, one can observe an increasing image variance close to the lateral edges of the phantom, which peaks somewhat outside the ROI. This indicates that both z-sbDBA modes allocate the propagated x-ray fluence efficiently regarding the given imaging task. In contrast, the image variance in the remaining FFM configurations (i.e., using a bowtie filter or no fluence filter at all) is higher inside the ROI than outside, which is an indicator for a low dose efficiency.

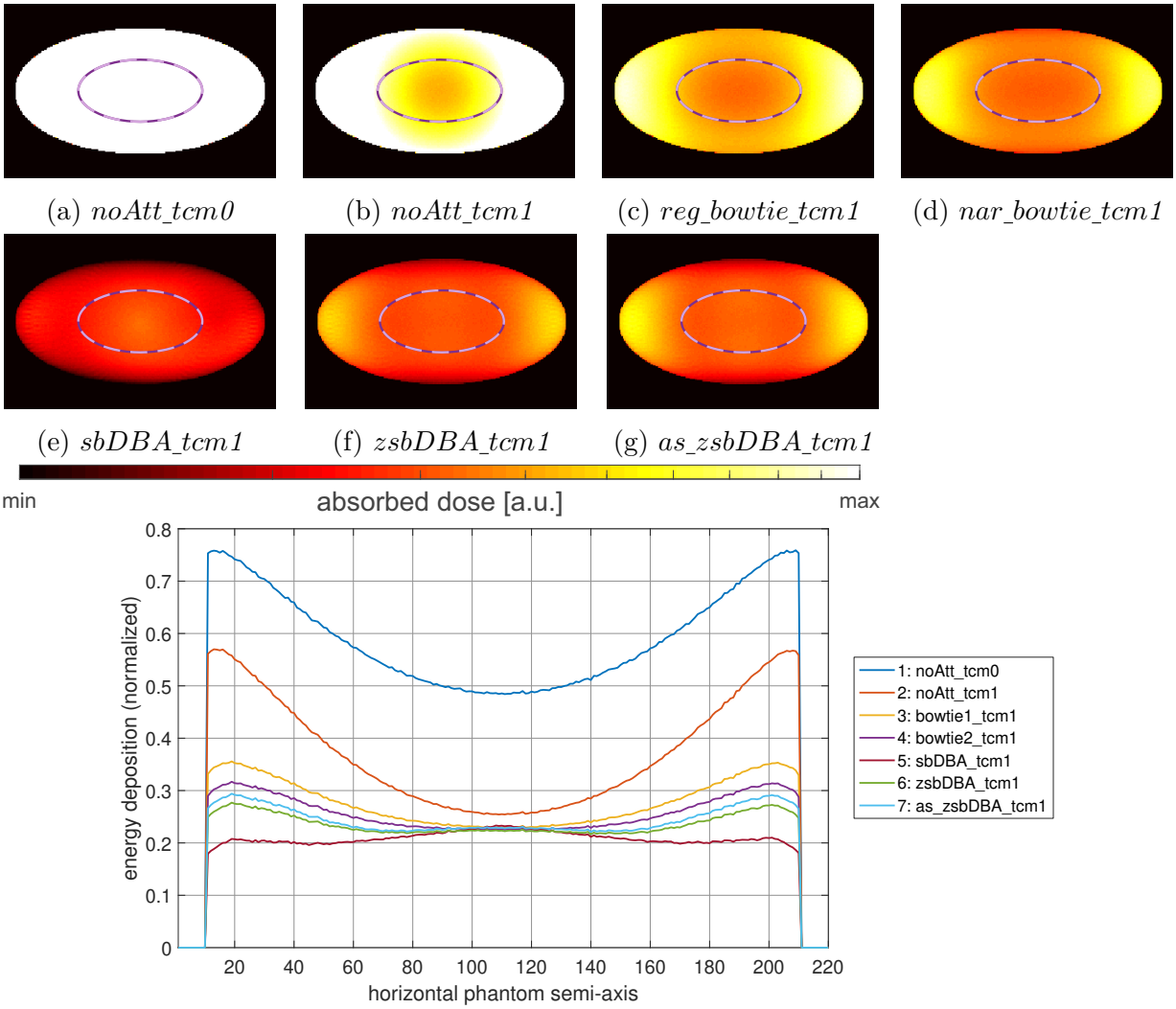

(a) *noAtt_tcm0* (b) *noAtt_tcm1* (c) *reg_bowtie_tcm1* (d) *nar_bowtie_tcm1*

(e) *sbDBA_tcm1* (f) *zsbDBA_tcm1* (g) *as_zsbDBA_tcm1*

(h) Line plots

Figure 5.4: The resulting 2D dose maps for ROI imaging task I (elliptical water phantom with central ROI). (a) - (g) The dose maps $D(u, v)$ visualize the spatial dose deposition (absorbed dose, Eq. 3.5) in the water phantom resulting from the specific radiation exposures of the FFM configurations. The 2D dose maps are matched to equal ROI image variance σ^2_{ROI}. Note that due to large differences in dose between the reference configuration (*noAtt_tcm0*) and the other FFM configurations, the dose map of the reference configuration (a) is visually in saturation with respect to the applied windowing. The same windowing on a logarithmic scale is used: center = 0.25 / width = 0.22. The dotted purple lines circumscribe the ROI. Panel (h) depicts the corresponding line plots along the horizontal axis of the phantom. The extension of the ROI is $x = [60, 160]$. Reproduced with permission from Huck et al. (2021).[158]

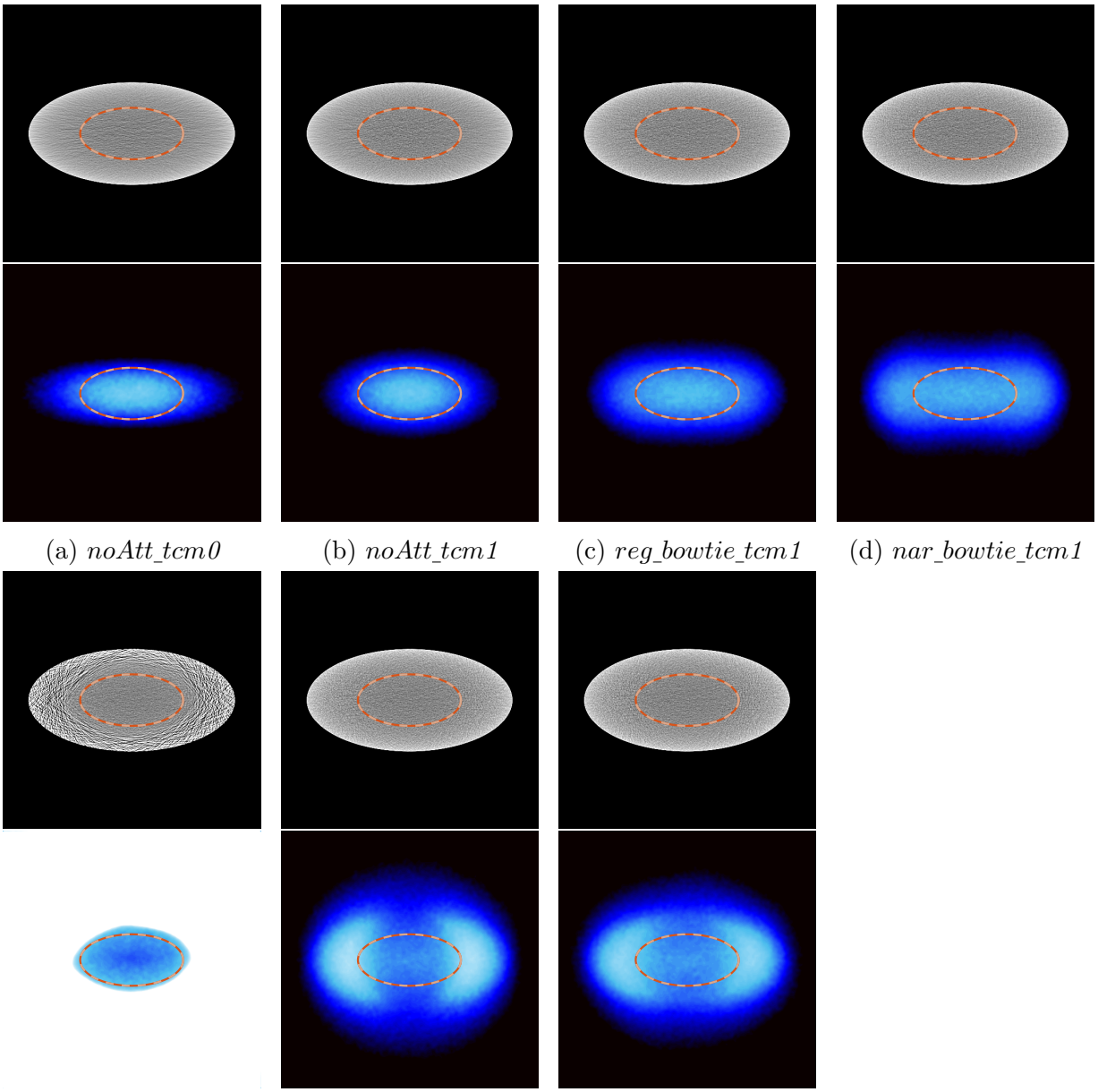

(a) *noAtt_tcm0* (b) *noAtt_tcm1* (c) *reg_bowtie_tcm1* (d) *nar_bowtie_tcm1*

(e) *sbDBA_tcm1* (f) *zsbDBA_tcm1* (g) *as_zsbDBA_tcm1*

Figure 5.5: Image reconstructions and variance maps obtained in ROI imaging task I. The resulting image reconstructions (upper rows) are matched to equal ROI image variance σ^2_{ROI}. The same windowing is applied: center = 0 / width = 150. The corresponding variance maps (lower rows) represent the variance in each pixel calculated from 100 difference images using the configuration-specific fluence. Note that the image variance in (e) is visually in saturation w.r.t. the applied scaling. A logarithmic windowing is used for all variance maps: center = 140 / width = 200. The dotted orange lines circumscribe the ROI. Adapted with permission from Huck et al. (2021).[158]

5.2.2 Imaging task II: Female thorax with off-centered heart ROI

Table 5.2 gives an overview of the effective phantom dose δ and the breast organ dose deposited in the female thorax phantom (heterogeneous) at equal ROI image quality. In this imaging task, the impact of the TCM (no. 2) is much less compared to the one in imaging task I. It allows to lower the dose only to 92 %. In turn, the fluence filters have a larger impact: the bowtie filters achieve a reduction in effective dose to 65 % (no. 3) and 60 % (no. 4) compared to the reference dose (no. 1). Both operation modes of the z-sbDBA reduce the radiation dose even further, 56 % (no. 6) and 57 % (no. 7), yielding a reduction by about 1/7 relative to the regular bowtie filter. Likewise, the organ dose associated with breast tissue is diminished by roughly 1/4 when using the z-sbDBA instead of the regular bowtie filter. The sbDBA (no. 5) is able to decrease the effective phantom dose and the breast organ dose to approximately 25 % of the reference dose. This dose deposition corresponds to less than half the dose necessary with the state-of-the-art regular bowtie filter.

In the fifth column in Table 5.2, the NPS isotropy score ϵ_{NPS} obtained for imaging task II is listed. It demonstrates that TCM is an effective measure to improve the noise isotropy inside the ROI from $\epsilon_{\mathrm{NPS}}(\text{no. } 1) = 0.59$ to $\epsilon_{\mathrm{NPS}}(\text{no. } 2) = 0.83$. It is worthwhile to note that the sbDBA achieves a similar level of NPS isotropy while requiring only about 1/4 of the radiation dose. Likewise, the NPS isotropy is at a comparably high level of about $\epsilon_{\mathrm{NPS}} \approx 0.79$ when using one of the bowtie filters or the z-sbDBA. Considering the dose savings reported in the third column, this demonstrates that the DBAs are capable of exploiting the x-ray radiation with higher dose efficiency than the reference configuration or state-of-the-art fluence filters.

Figure 5.6 depicts the spatial dose deposition in 2D dose maps. Without in-beam fluence filtration, the phantom edges (i.e., skin and breast tissue) are exposed to high doses, compare Figures 5.6(a) and 5.6(b). By additionally using the bowtie filters, the peak radiation exposure at the phantom edges is avoided, see Figures 5.6(c) and 5.6(d). In both operation modes of the z-sbDBA, non-ROI tissue can further be spared from radiation, particularly breast and lung tissue, as shown in Figures 5.6(f) and 5.6(g). The dose deposition within the heart ROI is virtually not affected by the fluence adaptation. The dose map associated with the sbDBA looks substantially different. It reveals that exclusively the heart ROI is exposed to high doses while surrounding non-ROI tissue is effectively shielded. Minor streaks along the radial direction can be observed in Figure 5.6(e), particularly at about 4 and 8 o'clock when looking at the dose map. This represents a noncritical artifact caused by the finite sampling of the projection angle ($\Delta\alpha = 5°$) in the MC simulation. It would disappear when using a higher sampling $\Delta\alpha$.

5.2.3 Imaging task III: Off-centered female thorax with centered heart ROI

In imaging task III, the table height is adjusted so that the heart ROI is moved to the isocenter of the CT system. Table 5.3 summarizes the results of the dose efficiency com-

Table 5.2: Overview of the dose efficiency achieved by different FFM configurations for imaging task II (female thorax phantom with off-centered heart ROI). Third column: the effective dose δ caused in the female thorax phantom, necessary to achieve a prescribed level of image quality (ROI image variance σ^2_{ROI}). Fourth column: the corresponding breast organ dose. The dose values are normalized to the reference scenario no. 1. Fifth column: the NPS isotropy score ϵ_{NPS} calculated inside the ROI (perfect isotropy: $\epsilon_{\mathrm{NPS}} = 1.00$).[167]

no.	FFM configuration (key)	effective phantom dose δ (normalized)	breast organ dose (normalized)	NPS isotropy score ϵ_{NPS}
1	*noAtt_tcm0*	1.00	1.00	0.59
2	*noAtt_tcm1*	0.92	0.93	0.83
3	*reg_bowtie_tcm1*	0.65	0.53	0.81
4	*nar_bowtie_tcm1*	0.60	0.45	0.78
5	*sbDBA_tcm1*	0.27	0.21	0.83
6	*zsbDBA_tcm1*	0.56	0.42	0.79
7	*as_zsbDBA_tcm1*	0.57	0.40	0.76

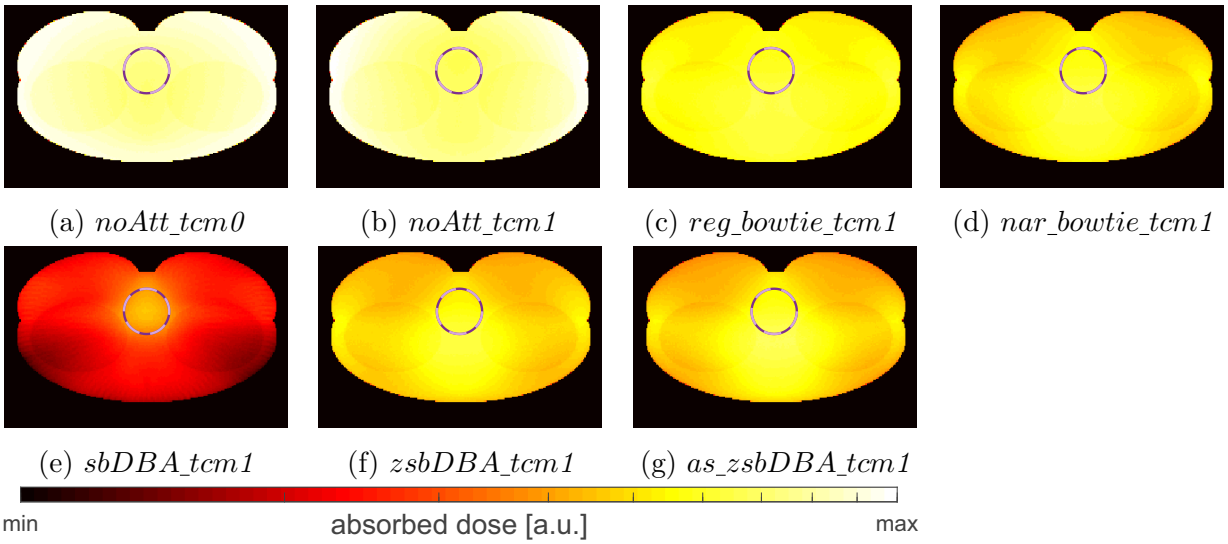

Figure 5.6: The resulting 2D dose maps for ROI imaging task II (female thorax phantom with off-centered heart ROI). The dose maps $D(u, v)$ depict the spatial dose deposition (absorbed dose, Eq. 3.5) in the female thorax resulting from the specific radiation exposures of the FFM configurations. The 2D dose maps are matched to equal ROI image variance σ^2_{ROI}. The same windowing on a logarithmic scale is used: center = 0.40 / width = 0.70. The dotted purple lines circumscribe the ROI. Reproduced with permission from Huck et al. (2021).[158]

parison for the effective patient dose and the breast organ dose. The data reveal that TCM alone (no. 2) lowers the radiation dose to 91 % of the reference dose. A substantial reduction in radiation dose is yielded by the usage of a fluence filter: the regular and the narrow bowtie filter lower the radiation dose to 59 % (no. 3) and 52 % (no. 4), respectively. The dose efficiency is further enhanced by using the z-sbDBA (no. 6 and no. 7). Both operation modes of the z-sbDBA facilitate an improvement in overall as well as in breast dose of about 1/3 compared to the conventional bowtie filter (no. 3) while preserving the reference image quality. The sbDBA (no. 5) requires only 26 % of the phantom dose used in the reference configuration to realize the prescribed level of image quality. The breast organ dose is even reduced to 21 %. Correspondingly, the sbDBA achieves the same ROI image quality at only half the dose with respect to the state-of-the-art bowtie filter (no. 3).

According to the fifth column in Table 5.3, TCM can considerably improve the isotropy inside the ROI from $\epsilon_{\mathrm{NPS}}(\text{no. } 1) = 0.60$ to $\epsilon_{\mathrm{NPS}}(\text{no. } 2) = 0.84$. Furthermore, the results show that in all FFM configurations where TCM is enabled, the NPS isotropy score is similar ($\epsilon_{\mathrm{NPS}} \approx 0.84$). Hence, the different radiation exposures produced by the fluence filters do not impair the image quality but allow for substantial dose reductions.

For a visual validation, 2D dose maps show the resulting spatial distribution of the dose deposition across the phantom cross-section in Figure 5.7. Similar to the previous imaging task II, the phantom edges, i.e., skin and breast tissue, are exposed to very high doses when being irradiated without in-beam fluence filtration, compare Figures 5.7(a) and 5.7(b). The usage of the regular bowtie filter can mitigate this issue at the phantom edges, see Figure 5.7(c). As shown in Figure 5.7(d), the narrow bowtie filter can further reduce the peripheral dose deposition. Consequently, the dose deposition at the actual ROI is higher than in peripheral non-ROI tissue, particularly at the back of the phantom. The target dose allocation – low in non-ROI tissue and high inside the ROI – is further approached when using the z-sbDBA or the adjustable static z-sbDBA, Figures 5.7(f) and 5.7(g), and especially when using the sbDBA, Figure 5.7(e).

Discussion & summary

The evaluation of the potential of ROI imaging reveals substantial dose savings when using appropriate FFM techniques. The results demonstrate that TCM can reduce the effective patient dose in all imaging tasks analyzed. Not only the dose efficiency can be enhanced by TCM, but also the noise characteristics (i.e., NPS isotropy) benefits from the adaptation. The impact of TCM, however, strongly depends on the geometry employed in the imaging task. In the first imaging task, considering an elliptical water phantom with central ROI, TCM can yield a substantial enhancement in dose efficiency (approx. 40 % dose reduction) compared to the reference configuration. The dominant role of TCM when imaging an elliptical water phantom is in accordance to what is reported in related studies, e.g., in Huck et al. (2019)[177] or in Gies et al. (1999).[89] In contrast, the impact of TCM is minor – compared to the contributions by in-beam fluence filtration – in the imaging tasks employing the heterogeneous thorax phantom (< 10 % dose reduction). The varying influence of TCM (Eq. 3.1) mainly depends on the different phantom attenuation

Table 5.3: Overview of the dose efficiency achieved by different FFM configurations for imaging task III (off-centered female thorax phantom with centered heart ROI). Third column: the effective dose δ caused in the female thorax phantom, necessary to achieve a prescribed level of image quality (ROI image variance σ^2_{ROI}). Fourth column: the corresponding breast organ dose. The dose values are normalized to the reference scenario no. 1. Fifth column: the NPS isotropy score ϵ_{NPS} calculated inside the ROI (perfect isotropy: $\epsilon_{\mathrm{NPS}} = 1.00$).[167]

no.	FFM configuration (key)	effective phantom dose δ (normalized)	breast organ dose (normalized)	NPS isotropy score ϵ_{NPS}
1	*noAtt_tcm0*	1.00	1.00	0.60
2	*noAtt_tcm1*	0.91	0.92	0.84
3	*reg_bowtie_tcm1*	0.59	0.55	0.84
4	*nar_bowtie_tcm1*	0.52	0.47	0.84
5	*sbDBA_tcm1*	0.26	0.21	0.82
6	*zsbDBA_tcm1*	0.42	0.36	0.84
7	*as_zsbDBA_tcm1*	0.42	0.36	0.85

properties L_{pha}. The attenuation is much stronger along the lateral projections in the case of the homogeneous water phantom compared to the thorax case where the x-rays cross two low-attenuation lung volumes, see Eq. 1.23. Hence, the difference in attenuation between a/p and lateral projections is smaller in the case of the heterogeneous female thorax. As a consequence, the impact of TCM is lower in imaging tasks using the female thorax phantom compared to the imaging task with the water phantom. In turn, the influence of the fluence filters (bowtie filters or DBAs) is dominant in the imaging tasks involving the female thorax. This, however, is not generally valid for all heterogeneous phantoms and eventually depends on the specifications (geometry and location of the phantom and the ROI) of the imaging task.

The advanced flexibility provided by the considered DBAs enhances the dose efficiency by appropriately redistributing the x-rays emanating from the x-ray tube. The z-sbDBA and the adjustable static z-sbDBA are shown to adapt the x-ray fluence with higher dose efficiency regarding the requirements of the imaging tasks than the bowtie filters. Compared to the state-of-the-art FFM configuration (no. 3), both z-sbDBA operation modes facilitate a dose reduction of about 15 % in imaging task I and II. The dose benefit reported in imaging task II (off-centered heart ROI) can even be increased by adapting the patient table height so that the heart ROI is moved to the CT isocenter, as described by the imaging task III. In this patient position, the dose savings enabled by the z-sbDBA modes raise to about 30 % compared to the regular bowtie filter (no. 3) and to about 20 % compared to the narrow one (no. 4), which is dedicated to cardiac imaging applications.

The actuation of a movable fluence filter during a CT acquisition is a critical issue as unveiled in the findings in Section 4.4 and in the research of alternative DBA approaches.[112,113,117,120] The results on the dose efficiency demonstrate that the improve-

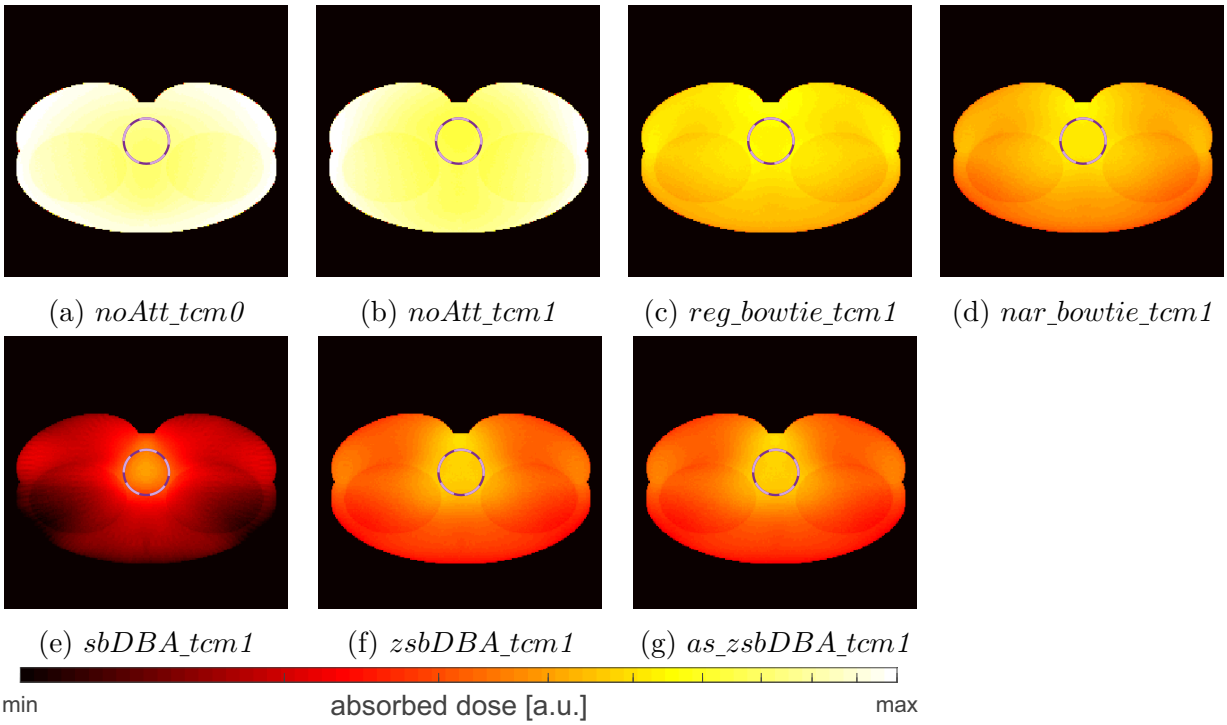

Figure 5.7: The resulting 2D dose maps for ROI imaging task III (off-centered female thorax phantom with centered heart ROI). The dose maps $D(u, v)$ depict the spatial dose deposition (absorbed dose, Eq. 3.5) in the female thorax resulting from the specific radiation exposures of the FFM configurations. The 2D dose maps are matched to equal ROI image variance σ^2_{ROI}. The same windowing on a logarithmic scale is used: center = 0.40 / width = 0.65. The dotted purple lines circumscribe the ROI. Reproduced with permission from Huck et al. (2021).[158]

ments are quite similar between both operation modes of the z-sbDBA (no. 6 and no. 7). Particularly in imaging task III, where the attenuation angle and thus the propagated fluence of the z-sbDBA are almost constant across the projections (Figures 5.3(d) and 5.3(e)), no advantage can be obtained from the dynamic adjustment (no. 6). In contrast, the adjustable static operation mode (no. 7) provides evident mechanical advantages regarding actuation and calibration over the fully dynamic z-sbDBA (no. 6). Therefore, the mechanical advantages of the adjustable static z-sbDBA might prevail the minor dose benefit of the z-sbDBA when considering the overall performance. Certainly, this assessment also depends on the specific imaging task. Especially for imaging tasks where the ROI is located at the isocenter of the CT system, the adjustable static z-sbDBA is suitable.

The sbDBA offers the most versatile transmission profiles due to two possibilities (G and H) to modulate the fluence. Consequently, the sbDBA adapts the x-ray fluence more precisely to the given imaging tasks and eventually exploits the emitted x-rays with superior dose efficiency compared to the other FFM configurations. As a consequence, the sbDBA yields the largest dose savings. Compared to the state-of-the-art FFM configuration (no. 3),

dose reductions of up to 60 % are achieved. The dose efficiency enhancement is less in imaging task I – about 30 % – because the ROI is relatively wide compared to the width of the sbDBA transmission profiles. The number of photons emanating toward the ROI needs to be sufficient in order to realize the prescribed image quality. Due to the triangular shape of the transmission profiles, however, the fluence at the edges of the wide ROI cannot decrease strong enough, which would be favorable for the protection of the surrounding tissue. Hence, the non-ROI tissue is exposed to a high x-ray fluence. A bell-shaped, steeper transmission profile might be more suitable in this situation. In the case of the small heart ROI, instead, the width of the fluence profile is much narrower and thus more suitable, exposing the tissue outside the ROI to only a small dose compared to the other FFM configurations.

In a first attempt to reduce the mechanical complexity of the sbDBA actuation, one could consider an adjustable static sbDBA – similar to the adjustable static z-sbDBA – where the attenuation angle G and the shift angle H are adjusted at an optimized angle during the acquisition ($G = \text{const.}$ and $H = \text{const.}$). Such an operation mode is not assumed to be an adequate compromise to mitigate the complexity, though. The high flexibility to adapt the transmission during the acquisition would be sacrificed and the benefit in dose efficiency be lower. Particularly, the lateral adaptation of the peak fluence, enabled by adapting the shift angle, allows to track off-centered ROIs and to yield high dose savings. In contrast, in a scenario where the DBA does not need to move at all (e.g., imaging task III), the adjustable static z-sbDBA might instead be the better option, due to its smoother, bell-shaped transmission and reduced mechanical complexity. Arguably, an intermediate level of flexibility where only one axis is rotatable and the other remains adjusted at an optimized angle is conceivable. In one mode, where only the attenuation angle is adjusted ($G = \text{const.}$ and $H \neq \text{const.}$), the ability to accommodate off-centered ROIs (e.g., imaging task II) would be retained and mechanical effort would be reduced. The opposite mode, where the attenuation angle is dynamic and the shift angle is adjusted ($G \neq \text{const.}$ and $H = \text{const.}$), might be suitable for tasks featuring a centered ROI (e.g., imaging task I). In the end, the optimum operation mode depends on the requirements of the specific imaging task and reduced mechanical complexity would be attained at the expense of loss in dose efficiency.

In any case, a sophisticated, reliable motion control is vital to avoid mechanical inaccuracies regarding the DBA motion (e.g., position reproducibility, position accuracy, trajectory perturbations etc.). Admittedly, such disturbances on the DBA trajectory that may occur during the acquisition with a CT system have not been accounted for in this dose efficiency evaluation. However, a systematic analysis of the influence of trajectory perturbations is suggested for future research, see Section 6.2.

Arguably, also other dose metrics than the effective dose might be conceivable for the optimization objective. Yet, the strength of the effective dose is to assess the stochastic health risk of a radiation-induced tissue damage by additionally considering the tissue-specific sensitivity to ionizing radiation. Alternative, the sum of energy impinging on the object[117,127] or – even more simplified – the number of impinging photons[166] are common dose estimations. Both metrics, however, ignore photons that pass the object or that are backscattered from the surface of the object. The absorbed dose neglects the varying sen-

sitivity to radiation of tissue and describes the severity of deterministic effects. A detailed description of the different dose metrics is presented in Section 1.2.5.

The optimization method presented uses *a priori* knowledge about the patient anatomy and particularly about the ROI location. In a clinical environment these data are not available and need to be obtained elsewhere. Thus, an easy-to-use method that provides additional anatomic information is required. Such a method might be based, for example, on the data of low-dose localizer radiographs or of 3D cameras, which are mounted on top of modern CT systems, and can be combined with, e.g., a machine learning method or an anatomy atlas.[176] Localizer radiographs and 3D cameras are commonly used to control the patient position and to estimate the x-ray attenuation (TCM determination) to prepare the CT examination. In treatment planning, for example, image data from previous diagnostic examinations could be exploited to localize the ROI for follow-up imaging.

In conclusion, the investigations on ROI imaging demonstrate that the proposed DBA concepts reveal considerable dose savings compared to existing FFM technology. The DBAs are shown to adapt the width of the emitted x-ray fan beam to width of the ROI. The sbDBA takes additional advantage of adjusting also the lateral position of the peak transmission that allows to "trace" off-centered ROIs. As illustrated by the respective dose maps, the DBAs spare non-ROI tissue while maintaining the same image quality inside the ROI. As a result, the DBAs exploit the radiation exposure at higher dose efficiency than state-of-the-art fluence modulation (no. 3 and no. 4). Due to the adaptation of the emitted x-ray beam to the object under investigation, the z-sbDBA realizes dose reductions of up to 30 % and the sbDBA of up to 60 % compared to a conventional bowtie filter with TCM.

5.3 Assessment and comparison of the sbDBA and the z-sbDBA concepts

Dose efficiency A major aim of CT ROI imaging is to enhance the dose efficiency in CT examinations by reducing the overall patient radiation dose while maintaining a high image quality in a specified ROI, as explored in Section 5.2. The sbDBA was shown to achieve a higher dose efficiency compared to the two z-sbDBA operation modes. Depending on the imaging task considered in this work, the dose efficiency of the sbDBA is about 15 % to 50 % better than that of the z-sbDBA. Nonetheless, the z-sbDBA is able to markedly outperform the dose efficiency of the conventional bowtie filter. The findings further indicate that a single pre-selected, task-specific transmission profile can yield a similar dose efficiency as a dynamically adapted fluence (adjustable static z-sbDBA vs. z-sbDBA). However, the success of such a strategy, where the DBA is fixed during the acquisition, strongly depends on the imaging task. When exclusively considering the dose efficiency, one might conclude that the sbDBA is the most suitable fluence filter to perform ROI imaging in CT. Such a consideration, however, would disregard challenges related to the mechanical realization in a CT system, as discussed in the subsequent paragraph. The assessment of the overall performance of a DBA concept should not only focus on the benefit of dose savings. Also,

the technical obstacles and the practical implementation of a DBA concept should be considered for a reasonable assessment.

Mechanical complexity and actuation system The precise actuation of the DBA mechanics is not trivial and a central aspect of a DBA concept regarding its realization. Both DBAs bear the risk of image artifacts due to mechanical imperfections, as mentioned in the investigations on the phantom reconstruction, see Section 4.4. During the experimental measurements, some challenges regarding the precise alignment of the DBA prototypes arose: for example, the execution of a pre-defined, complex z-sbDBA trajectory did not yet work reliably. Deviations from the prescribed trajectory were observed in some cases. In contrast, the angular adjustment at a specific angle worked precisely in general. These experiences emphasize that there is still some more engineering work to be done to enable a more resilient and more reliable z-sbDBA prototype. Nevertheless, the first attempt to realize a z-sbDBA prototype was sufficiently stable to acquire various transmission profiles at different angles (Section 2.3.1). These measurements allowed to evaluate the z-sbDBA performance on the basis of transmission profiles measured on a clinical CT system. The realization of an automated, reliable actuation of the sbDBA would have been too extensive for the scope of this work. Conclusively, the mechanical implementation of the z-sbDBA is less complex compared to the sbDBA because it only rotates about one axis, which is easier to realize. Hence, the mechanical effort to perform FFM with the z-sbDBA is less than that required for the sbDBA. Especially the simultaneous rotation of the sbDBA about two axes and the calibration of the high-frequency transmission are challenging. Also, the number of components involved is reduced in the case of the z-sbDBA, which is favorable in terms of error rates and precision.

Space requirements Another important characteristic of a DBA concept is the space required to accommodate the DBA in a CT system, which is closely related to the aforementioned aspect. In this regard, the z-sbDBA is more suitable than the sbDBA as it is more compact. The rotation about a single axis requires only a single actuation system and a smaller suspension to tilt the z-sbDBA. Furthermore, the first z-sbDBA prototype has already been shown to fit into a conventional collimator box, compare Figures 2.2(d) and 2.3. The Cardan suspension (gimbal) and the second actuation system, as necessary for the sbDBA, requires more space in the CT gantry, where space is limited. Commonly, a CT gantry is packed with various components necessary for the proper operation of a CT system and the clearance radius (bore radius) is attempted to be increased. This aspect is also discussed in Section 6.1 with respect to alternative DBA concepts.

Shape of the transmission profiles Great importance is attributed to the details of the transmission profiles obtained when an x-ray beam passes the fluence filter. The investigations identified the shape of the x-ray transmission as a major shortcoming of the sbDBA as it i) produces high-frequency transmission profiles along the fan beam width and ii) enables only triangular transmission profiles. The first aspect relates to the impact of inaccuracies: the alignment of the attenuation sheets along the fan beam width causes high-frequency fluctuations on the transmission profile, compare Figure 4.1. Hence,

an unintended, small displacement of an attenuation sheet or the setup strongly affects the transmission measured at the corresponding detector channel. An incorrect detector signal causes severe ring artifacts in the reconstructed image and prevents quantitative CT imaging, as unveiled in Figure 4.6(a). In contrast, the revised structuring of the z-sbDBA eliminates the high-frequency fluctuations due to the alignment parallel to the fan beam plane (z axis). The resulting z-sbDBA transmission profiles are shown to be smooth across the width of the fan beam, compare Figure 4.2, which reduces the severity of inaccuracies. As a result, the z-sbDBA is less prone to mechanical deviations and the risk of ring artifacts is diminished compared to the sbDBA design. The second aspect is related to the suitability of transmissions achievable: considering common attenuation profiles present in CT imaging, e.g., from an elliptical patient cross-section, a bell-shaped transmission profile (z-sbDBA) is more appropriate to compensate for the patient attenuation than a triangular transmission profile (sbDBA). This is justified by the x-ray attenuation in matter, see Eq. 1.23, and the geometry of typical objects under investigation. Also alternative DBA approaches,[107,110,119,120,178] pursue the aim to obtain bell-shaped transmission profiles from the respective fluence filters.

Versatility and ROI applications A key advantage of the sbDBA is its superior flexibility to shape the transmission profiles. In particular the possibility to laterally shift the peak transmission, which cannot be realized by the z-sbDBA, is beneficial in terms of dose efficiency. This feature allows the sbDBA to "track" also ROIs, which are not located at the isocenter of a CT system. Consequently, a variety of ROI imaging applications can be covered by using the sbDBA, including off-centered organs such as the inner and middle ear, the kidneys, lung, or breast tissue. The main drawback of the z-sbDBA concept is that it is limited to symmetrical transmission profiles with the peak transmission at the center. This restricts the scope of possible ROI imaging applications, though. Only in suitable scenarios, this shortcoming can be circumvented by moving the off-centered ROI to the CT isocenter, as exemplified in imaging task III. This, however, is not possible in all scenarios due to, e.g., the limited bore radius given by a CT system. Furthermore, most CT patient tables cannot translate sideways, which would be required to shift a laterally off-centered ROI to the CT isocenter. The application of ROI imaging to other organs as well as additional considerations on centering off-centered ROIs are suggested in Section 6.2.

Achievable dynamic of transmission As demonstrated in Section 4.1 and 4.2, the sbDBA provides a larger dynamic of achievable transmissions than the z-sbDBA. While the transmissivity τ_{max} is comparable between both designs, the sbDBA can decrease the remaining transmission much more strongly, see Figures 4.1, 4.2, or 4.4. A low remaining transmission at non-ROI tissue contributes to effectively reducing the patient radiation dose and thus to improve the overall dose efficiency, compare Section 5.2. However, the x-ray fluence should not be cut to zero outside the ROI due to restrictions of the image reconstruction process (e.g., data truncation artifacts). To enable a reasonable image reconstruction, at least some detector signal for rays passing the patient outside the ROI is necessary, which should not be too noisy.

Scattering and spectral dependency The total amount of scatter radiation produced by the sbDBA and the z-sbDBA when the x-ray beam passes these filters is similar and considerably lower compared to a conventional bowtie filter at about the same x-ray transmission, see Figure 4.5. Regarding the spectral dependency of the x-ray transmission on the emission spectrum, the sbDBA outperforms the z-sbDBA. While the transmission of the sbDBA is almost independent of the applied tube voltage, the transmission increases for higher tube voltages when using the z-sbDBA instead. Nevertheless, the z-sbDBA exhibits a considerably lower spectral dependency than the bowtie filters, compare Figure 4.4. Both aspects, less scatter radiation and a lower spectral dependency, are desirable to ease the image acquisition and image reconstruction process and eventually enhance the resulting image quality.

DBA assessment: proposed strategy to foster CT ROI imaging

Personal opinion

Taking into account the strengths and the challenges of the DBA concepts proposed in this thesis, it is recommended to first consider the z-sbDBA concept for further investigations on ROI imaging in CT. As elaborated, the z-sbDBA achieves substantial dose benefits over conventional static bowtie filters. Other benefits relate to scatter propagation, spectral changes, and the use in the upcoming photon counting CT (PCCT) technology. For aspects regarding PCCT – also referred to as spectral CT – the reader is referred to Section 6.1. Although the z-sbDBA cannot change the lateral position of the peak fluence as facilitated by the sbDBA, the advantages regarding a resilient technical realization of the z-sbDBA are likely to prevail the advanced functionality of the sbDBA. The precise mechanical integration and the reliable actuation are demanding but at the same time vital to foster this novel technology. Hence, first the less complex z-sbDBA system, which exhibits addressable mechanical challenges, should be pursued to collect further experiences in the field of CT ROI imaging – starting with the adjustable static mode and focus on centered ROIs. Afterwards, at a more experienced stage, the z-sbDBA can be operated in the fully dynamic mode. An overview of suggested future investigations and measures is given in Chapter 6, particularly in Section 6.2.

Chapter conclusion In this chapter different FFM configurations were compared regarding their dose efficiency in CT ROI imaging. For this purpose, three different imaging tasks were defined, encompassing an elliptical water phantom and a heterogeneous female thorax model. In addition to the sbDBA and the z-sbDBA in its original conception, an adjustable static operation mode of the z-sbDBA, where the angular adjustment remains fixed at a pre-defined angle during the data acquisition, was investigated.

First, the DBA movements were determined using a trajectory optimization method, which was developed in this thesis. It aimed at minimizing the dose deposition in the phantom and maximizing the image quality inside the ROI for a given imaging task.

Reasonable trajectories were obtained from the optimization method, adapting the emitted x-ray fluence to the width of the ROI cross-section and – in the case of the sbDBA – additionally to the lateral occurrence of the ROI. The x-ray fluences associated with the optimized DBA trajectories reflect the phantom and ROI geometry.

In the second part, the DBA dose efficiencies achieved with the trajectories determined were compared with the dose efficiency of other FFM configurations – including TCM and two different shapes of a bowtie filter. The comparison revealed that due to the adaptable x-ray redistribution, the DBAs facilitate to image a specific ROI at high image quality while sparing surrounding non-ROI tissue. Thus, substantial dose reductions are possible: depending on the imaging task, the z-sbDBA realized a dose reduction of 15 % to 30 % as compared to the regular bowtie filter of a modern CT system. It is notable that the adjustable static z-sbDBA, which provides reduced flexibility but easier actuation, yielded similar dose reductions as the z-sbDBA. Using the highly adjustable sbDBA instead, even higher dose reductions of about 30 % to 60 % were achieved. Irrespective of practical issues, the DBAs are able to redistribute the x-ray radiation more dose efficiently than state-of-the-art static bowtie filters. In conclusion, this evaluation emphasizes the benefits of ROI imaging for CT diagnostics as feasible with the proposed DBA designs.

Finally, the differences, advantages, and potential fields of applications were compared between the sbDBA, the z-sbDBA and the adjustable static z-sbDBA. Although the sbDBA facilitates the largest dose reductions, it is debatable whether this DBA design can be realized in the near future due to its demanding mechanical requirements. The z-sbDBA provides an attractive compromise between fluence adaptation and mechanical effort while being suitable for imaging centered or little off-centered ROIs. In particular, the adjustable static operation mode of the z-sbDBA represents a promising concept of a compromise solution, which could be realized with manageable effort. Accordingly, it is recommended to first pursue the concept of the adjustable static z-sbDBA to leverage ROI imaging in x-ray CT diagnostics.

Overall, two new DBA concepts have successfully been validated for ROI imaging in CT with superior dose efficiency compared to state-of-the-art FFM technology. The promising results raise perspectives of future patient dose reductions enabled by ROI imaging using the presented DBAs.

Chapter 6

Additional considerations and future perspectives

6.1 Additional considerations

Comparison with alternative DBA concepts The mechanical realization of a movable DBA remains one of the major engineering tasks of FFM, as reported by many other studies. In literature, a variety of DBA approaches are proposed, which can be categorized by their basic working principles: movable bowtie-shaped concepts (translating[110] and double wedge[107] attenuator), wedge-based concepts (piecewise-linear,[111,112] piecewise-constant[102,113,114]), fluid-based concepts (tubes along[115,116,138] or perpendicular[117] with respect to the source-to-detector axis), or the MAD.[118–120] The above list covers a selection of relevant DBA approaches, which are detailed in Section 1.3.2 and in Figure 1.19. In many cases, the DBA concepts become insignificant as soon as it comes to the technical realization in a real CT system: either the duration to adjust the filter components exceeds the available time or the required space for the apparatus is not available in the packed CT gantry. Especially the concepts where solid DBA components are moved in and out of the fan beam (bowtie- or wedge-based DBAs), the required attenuator speed (e.g., velocities of about 25 cm/s or 40 cm/s are reported[111,113]) to adjust the DBA components in the demanded position is nontrivial regarding typical CT rotation times (commonly 1 s to 1/4 s).[150] When specifying the actuation, one faces the dilemma between high attenuator speed allowing a high flexibility on the one hand, and a precise adjustment on the other hand. Yet, these concepts might be more suitable for C-arm or radiography systems that rotate slower or not at all, respectively. Concepts based on fluids might face the issue of adaptation time and precision as well. Furthermore, it is unclear whether the flexible membrane employed in the DBA approach, where small, flexible cavities are filled and evacuated,[115,116] may resist the x-ray radiation exposure in the long term. Typically, the fluid- and wedge-based DBA approaches require a lot of space for the multiple components they consist of, which is hardly available inside a contemporary CT gantry. On the contrary, one rather attempts to reduce the required space of CT components in order to increase the

bore radius of the CT gantry.[179,180] Hence, the compact design of the sbDBA and z-sbDBA are attractive in this aspect. The first z-sbDBA prototype was accommodated in a regular collimator box, which usually carries the conventional bowtie filter(s) in a clinical CT. Furthermore, the duration to change the angular position across the projections, necessary to realize the prescribed trajectories, is assumed to be realistic for typical CT acquisition times.

The compact MAD concept, Figure 1.19(g), allows to adjust the transmission by only small lateral displacements (sub-millimeter range).[118] Similar to the sbDBA, it can shift the peak transmission laterally and features a structure along the fan beam width. In contrast to the sbDBA, it produces bell-shaped transmission profiles as achievable with the z-sbDBA. The main obstacle regarding the MAD concept is the trade-off between a high maximum x-ray transmission (transmissivity $\tau_{\max}$) and a high dynamic range of the achievable transmission. Depending on the duty cycle of the MAD grids, either a large dynamic range of the transmission profiles is accomplished at the expense of a lower maximum transmission or a higher maximum transmission through the MAD is enabled but then the dynamic range of the transmission profiles is sacrificed. These two situations correspond to either thick or thin bars of the two MAD grids, respectively.[120] Generally, a high x-ray throughput is valuable in CT imaging as the maximum x-ray fluence is limited by technical limitations of modern x-ray tubes (e.g., heat management of the anode disk).[24,48,98] So far, the MAD concept was only analyzed on a preliminary test bench of an x-ray system. In this setup, the sample was rotated and imaged by a stationary tube-detector setup.

In comparison with the alternative DBA concepts (e.g., the bowtie-shaped DBAs), the sbDBA delivers a high functionality regarding the transmission that can be achieved. The mechanical effort, however, is comparable to what other concepts demand but is certainly not trivial. The space the sbDBA requires is addressable and also the duration to adjust the angles is expected to be within reach of modern actuators. The z-sbDBA provides a moderate flexibility of transmission profiles as it is limited to symmetrical transmission profiles. This disadvantage in terms of functionality is in turn an advantage in terms of actuation. The mechanics of the z-sbDBA is much less complex than the mechanics of the sbDBA or alternative approaches, because there is only a single axis to be controlled. Due to the small tilts necessary, the time to adjust the angular position is sufficiently short. The motor employed in the z-sbDBA prototype was able to tilt the z-sbDBA two times from $\vartheta = 0.0°$ to $\vartheta = 2.0°$ and back within a gantry rotation time of 1 s. The space necessary is small and comparable to the space occupied by the bowtie filter, which the z-sbDBA surrogates. Hence, the technical demands required by the z-sbDBA are addressable compared to other DBA approaches: within the scope of this thesis, it was already possible to realize a first prototype of the z-sbDBA, which was successfully integrated into a clinical CT system. The presence of the sbDBA and the z-sbDBA lowers the transmissivity $\tau_{\max}$ by only about 20 % while maintaining their full dynamic range. Similar to the MAD design, the spectral properties are superior compared to other DBA approaches. In conclusion, the comparison with alternative DBA concepts reveals that the sbDBA and the z-sbDBA are assumed to be at least equivalent in their overall performance and in several aspects more practicable and realistic regarding their realization in CT imaging.

Potential dose reductions achieved with alternative DBA concepts The potential dose savings when performing FFM and ROI imaging are investigated in several studies using different ways to realize FFM.[103,111,112,114,117,127,129,130,132,133,135] A direct comparison between these studies is difficult as the authors use different measures to assess the image quality and to calculate the radiation dose, or employ different phantoms and use other reference cases in their comparisons. Additionally, variations arise from the optimization objective applied, the use of TCM, the consideration of a bowtie filter (and its specific transmission properties), the beam characteristics (e.g., tube voltage, mono-/poly-energetic), the inclusion of scatter radiation etc. Nevertheless, dose reductions in the range of approximately 30 % to 50 % compared to a standard bowtie filter are commonly reported in the aforementioned DBA studies. In Wang et al. (2019),[127] for example, the spine is selected as ROI in an abdomen phantom. The authors report that by using the MAD, the radiation dose is decreased by about 50 % relative to a full-field acquisition while maintaining the CNR. The study does not include the additional contributions of TCM, though. In a study on the piecewise-linear attenuator, the authors demonstrate a dose reduction of about 50 % in pancreas or aneurisma imaging compared to a bowtie filter (optimized TCM).[112] In a related study, they investigate the movable bowtie-shaped concepts, which yield a dose reduction of about 30 % at equal peak variance.[122] The FDBF concept, Figure 1.19(f), is shown to reduce the entrance-energy-fluence by over 60 % as compared to a conventional bowtie filter at equal peak noise.[117] The comparison with dose savings achieved by alternative concepts shows that the dose savings realized by the sbDBA and the z-sbDBA are comparable to the findings of other FFM research.[8,9]

Image quality assessment According to the methodology applied in this thesis, image quality was approximated with the inverse of the image variance σ^2. It must be acknowledged, however, that image quality is not fully described by the image variance.[67] Yet, this simplification is considered eligible for the purpose of this research since neither the modulation transfer function nor the contrast of the CT system are considerably affected by the fluence modulation. Consequently, it is assumed that the mean image variance within the ROI is a justified surrogate for the image quality assessment as part of the optimization method. A valid criticism concerning the selection of the image quality criterion might be that the image variance cannot characterize the noise isotropy in a reconstructed image.[122] Directional noise can deteriorate the image quality of the reconstructed image but does not necessarily raise the noise amplitude. To account for that, the NPS isotropy score was deployed as an addition image quality measure that evaluates the noise isotropy.

Admittedly, the mean image variance bears the risk of redistributing noise inappropriately: without providing further constraints to the x-ray fluence optimization, the image quality in some regions might be improved at the expense of increasing the image variance elsewhere. It is unfavorable when the x-ray fluence is redistributed from a diagnostically relevant region to an irrelevant one. To prevent such a situation, the spatial distribution of the image variance was determined for the different FFM configurations, as exemplified for imaging task I (Figure 5.5), to reveal such a variance distribution, if present. Alternatively,

the peak image variance might have been considered instead of the mean image variance. This metric is particular suitable for the detection of small lesions or calcifications and was considered in other DBA investigations.[117,122,125,135] In addition, other studies used the CNR,[126] the SNR,[103] or task-specific detectability indices[124,181] as image quality metric (Section 1.2.4). In this work, the mean image variance was chosen, following the theoretical considerations of Harpen (1999)[166] on the dose efficiency, see Section 3.3.3. In the end, the choice of the image quality metric depends on the specific clinical task.[122,124]

Method for TCM The employed TCM method (hsqTCM) calculated the tube current factor κ based on the maximum attenuation per projection, as stated in Eq. 3.1. The actual direction in which an x-ray beam propagates through the object was not taken into account. Consequently, the same tube current factor is obtained irrespective of whether the ray enters the object at a highly radiosensitive organ (e.g., breast tissue) and then penetrates the object or vice versa. The entrance dose of x-ray radiation is known to be high and decreases exponentially when further propagating through matter (Eq. 1.23). Existing studies on angular tube current modulation evince that the patient radiation dose can be optimized when accounting for the exact propagation direction through the object.[93,94] A study by Huck et al. (2021)[92] adopts the dose and image quality calculation method presented in this thesis to optimize the TCM as function of the projection angle. The authors demonstrate that the consideration of the x-ray propagation direction in combination with the z-sbDBA yields dose savings of up to 30 % compared to the hsqTCM method in combination with a conventional bowtie filter.[92]

Enhanced performance in photon counting CT In recent years, photon counting detectors (PCDs), which provide the functionality of spectral CT imaging, are subject of active research. PCDs are based on semi-conductors and allow to directly measure the energy of a single incident x-ray photon. Thus, the detector signal can be resolved using energy bins.[182,183] This upcoming technology has the potential to enhance the dose efficiency, the spatial resolution, and the image noise in CT diagnostics.[8,9,73,182,184,185] A major challenge, however, is the high x-ray fluence impinging on the PCD. If the count rate raises above a detector specific level, the detector suffers from count rate loss due to the limited temporal resolution – called pulse pile up effect – and the performance consequently degrades.[9,186,187] Nowadays, count rates of about 10^9 counts/s/mm^2 are common in clinical CT systems.[8,188] A solution to address this issue is to redistribute the emitted x-ray fluence in order to reduce the incident count rate on the detector. Among others,[111,117,188–191] McCollough et al. (2012),[8] and also Taguchi and Iwanczyk (2013),[184] suggest the usage of dynamic fluence filters to accomplish this essential aim. In several studies, the benefit of DBA usage in PCCT is investigated, yielding promising results.[111,114,117,135,175,188,189] Accordingly, PCCT might be another beneficial field of application for the sbDBA and the z-sbDBA. A further dose efficiency enhancement is expected from the symbiosis of PCCT and DBA usage. In a first investigation, one may analyze the reduction in dynamic range

of the detector signal that is achievable when using the new proposed DBAs instead of contemporary bowtie filters.

Dose and image quality when imaging miscentered patients The importance of correct patient positioning is investigated in a variety of studies.[125,192–198] Consent prevails on the relevance of correct patient positioning. The authors emphasize the dose penalties and image quality deterioration arising when imaging miscentered patients. As investigated in, e.g., Mao et al. (2018)[125] or in Hsieh et al. (2014),[112] the respective DBAs are able to account for the misplacement and thus improve the dose efficiency or the image quality, respectively. Considering the results obtained from imaging task II and imaging task III, one can deduce an improved dose efficiency when using the sbDBA that allows to "follow" off-centered objects. The lateral shift of the peak transmission enabled by the sbDBA may also be valuable when imaging miscentered patients. Although the z-sbDBA does not enable a lateral shift, at least some benefit can be expected from its usage compared to a static bowtie filter. Given a patient that is positioned off-centered – for example a few centimeters too high – the z-sbDBA still allows to adapt the transmission: at lateral projections, where the center of the patient cross-section is above the CT isocenter, a broader z-sbDBA transmission profile could be used to adequately expose the upper part of the body. Accordingly, the x-ray fluence is sufficient for the entire patient cross-section. Beneath the back of the patient, the transmission profile would be too wide and the fluence unnecessarily high. This, however, does not deteriorate the dose efficiency as the excess radiation would merely miss the patient. In comparison, photon starvation might occur at the upper part of the body when using a static bowtie filter instead. At projections along the a/p axis, the patient seems centered. Only the width of the patient appears different between projections from the front (wider) or the back (narrower). This effect, comparable to a "magnification" on the CT detector, occurs due to the varying distances between the x-ray source, the patient and the detector. Unlike the static bowtie filter, the z-sbDBA could adapt to the changing patient width appearing from different projections by modulating the shape of the transmission profile. The requirements on the patient positioning could benefit from such a functionality. This can reduce patient preparation time and save radiation dose. However, these considerations have not yet been investigated for the sbDBA or the z-sbDBA. Thus, in a future study the potential of this application should be explored.

6.2 Future perspectives

Personal opinion

In this thesis, the concepts of the sbDBA and the z-sbDBA have comprehensively been analyzed: from experimental measurements focusing on the DBA x-ray transmission and photon interactions through (mechanical) aspects for operating the DBAs on a CT system up to the potential for clinical diagnostic applications. During this research, some more aspects arose that are worth being investigated but are beyond the scope of this work. A few

aspects were already suggested in the preceding Section 6.1. This concerns particularly the potential benefit of using the sbDBA or the z-sbDBA in PCCT and their value to overcome issues in terms of patient positioning. On top of that, the following investigations and measure are suggested to be pursued in order to further explore this technology:

- *Identify the most promising clinical applications for ROI imaging.* Besides cardiac imaging as investigated in this work, additional ROI applications such as cancer staging (e.g., liver or pancreas cancer), abdominal aortic aneurysm imaging,[112] or imaging of the middle and inner ear (e.g., Cochlea implant, deafness, vertigo etc.) are conceivable. Furthermore, ROI imaging might also facilitate prophylactic screening (e.g., lung[48] or mammography screening[199]) and promote the usage of CT in image-guided radiotherapy[200,201] (e.g., brachytherapy, target volume positioning, pretreatment imaging for planning), and interventions. Together with radiologists and oncologists, different organs and applications can be analyzed to extend the scope and eventually, to enhance the clinical potential of ROI imaging.

- *Evaluate the possibility to center off-centered ROIs.* After identifying promising applications for ROI imaging, an evaluation could assess whether the method of centering off-centered ROIs by adjusting the table height and the patient position can be extended to other cases, comparable to imaging task III. This method, however, is limited by, e.g., the bore radius of a CT system, the patient table movement, the FOV, and the patient mobility. Moreover, when imaging off-centered objects, particularly in combination with TCM, care must be taken to avoid image artifacts and dose penalties.[184,196,197]

- *Revise the shape and structuring of the attenuation sheets.* As mentioned in Section 2.1, the shape of the attenuation sheets was determined heuristically. Knowing the relevant clinical applications allows to further optimize the exact shape and the structuring of the attenuation sheets. For example, one feature of the z-sbDBA is the wave-like curvature on one side of its attenuation sheets, which mainly determines the width of the transmission profiles. Depending on what is determined to be a typical cross-section of relevant ROIs, the shape can be redesigned. Another feature relates to the aspect ratio (see Section 2.1.2) of the attenuation sheets. In the current z-sbDBA design, a tilt of only about 1.5° covers the entire dynamic range for fluence modulation. This is beneficial regarding the duration to adjust the filter. At the same time, however, the small movement is prone to errors as minor deviations from the prescribed angle or some noise on the motor control might considerably change the transmission. Thus, a reasonable aspect ratio that balances the duration of the adjustment and the angular tolerance can enhance the DBA performance. These considerations are applicable to the sbDBA as well.

- *Systematically investigate the mechanical sensitivity.* As mentioned multiple times in this thesis, the sensitivity of the DBAs to mechanical inaccuracies is one major challenge regarding the DBA realization. Deviating angular alignments between the

calibration and the object measurement or perturbations during the data acquisition distort the resulting HU values and cause ring artifacts (Figure 4.6). To specify the actuation system, it is helpful to know the acceptable tolerances for a given DBA trajectory. Thus, an analysis that systematically investigates the mechanical sensitivity is recommended. For example, the difference in HU values of reconstructed images could be evaluated depending on the angular deviation to gain a better understanding of the impact of trajectory perturbations. Moreover, the reproducibility of a specific angular position and the discrepancy when driving the DBA to a given position in clockwise versus counterclockwise direction are relevant to the specification.

- *Evaluate whether a spectral correction is necessary.* The investigations on the spectral dependency and scatter radiation revealed that the spectrum of the x-ray beam changes slightly when passing the z-sbDBA (lead; moderate changes) or the sbDBA (tungsten; marginal changes). In Gang et al. 2019,[120] the authors applied a spectral correction to account for spectral shifts due to oblique x-rays that graze an edge of the attenuating tungsten bars of the MAD. The spectral correction was shown to suppress image artifacts.[120,202] Such artifacts, even if not yet noticed in image reconstructions analyzed in this thesis, might also occur when using the sbDBA or the z-sbDBA and should be considered in future research.

- *Refine the trajectory determination method.* The trajectory determination method applied in this thesis is not suitable for daily routine in clinical practice, as elaborated in Section 5.1. While this method was appropriate for the aim of this research, future works should develop methods that determine the DBA trajectory without *a priori* knowledge and in much shorter time, preferably in real-time. Potential methods have already been proposed in literature, compare Section 5.1. With additional modifications, some of them might also be suitable to determine trajectories for the sbDBA and the z-sbDBA. The development of a fast and precise trajectory determination method is essential to advance CT ROI imaging in clinical use.

This short overview provides a list of suggested investigations that are considered as useful and purposeful regarding the development of the DBA concepts and to eventually foster CT ROI imaging. These considerations are intended to promote an improved understanding of the characteristics of the DBAs and to identify the most suitable clinical fields of applications. In addition to further research on the DBAs, it is also vital to advance the maturity and finally the commercialization of DBAs to provide patients with improved, individualized low-dose CT diagnostics by ROI imaging.

Conclusion

The aim of this thesis was to develop and to validate an x-ray filtration concept, suitable for FFM in CT imaging. Therefore, two novel x-ray filters, the sbDBA and the z-sbDBA, were proposed and their benefits in ROI imaging were evaluated. To this end, physical prototypes of the DBA concepts were built and successfully integrated into a clinical CT system.

In the first part of this thesis, measurements using a clinical CT system equipped with the DBA prototypes demonstrated the feasibility of FFM in a proof-of-concept. By only small tilts, both DBA prototypes were able to modulate the propagated x-ray fluence – the key function of a dynamic x-ray filter – and achieved a wide range of transmission profiles. The sbDBA offered a highly flexible modulation of the transmission profile, promoted by the additional capability of shifting the peak transmission also across the fan beam width. The high-frequency patterns occurring across the sbDBA transmission profiles were effectively eliminated using the z-sbDBA that employs a refined structuring of the attenuation sheets. Furthermore, it produced more suitable transmission profiles for CT imaging, i.e., smooth, bell-like shapes. However, the z-sbDBA is not capable of shifting the peak transmission laterally, but features simplified mechanics in turn.

A comparison with a regular CT system, which employs bowtie filters, revealed superior characteristics of the z-sbDBA and particularly of the sbDBA: the x-ray filtration achieved with the DBAs was substantially less dependent on the tube voltage (emission spectrum). Furthermore, adverse scatter radiation from interactions with the x-ray filters was reduced by about one order of magnitude when using a DBA instead of a bowtie filter. These features of the DBAs contribute to an easier data acquisition, enhanced image quality, and reduced radiation burden to the patient.

First-time image reconstructions from data acquired with the new proposed DBAs provided reasonable images of homogeneous phantoms, although some suffered from ring artifacts. The mechanical reliability of the actuation system still requires some engineering effort. In light of the fact that initial prototypes of the DBAs, which exhibit a strong structuring, were placed in the beam path of a clinical CT system for the first time, the overall image quality was promising, though.

The second part of this thesis focused on the application of the DBAs in ROI imaging and compared their dose efficiency with that of state-of-the-art FFM technology. For this purpose, an optimization criterion was developed to optimize the angular movement (i.e., the trajectory) of the DBAs regarding a given imaging task. The criterion aimed at minimizing the dose deposition in the phantom and maximizing the image quality (i.e., min-

imum mean variance) inside the ROI. The trajectory optimization method was applied to three different imaging tasks, including a heterogeneous female thorax. It returned smooth DBA trajectories that reflect the ROI geometry: on a projection-wise basis, the emitted x-ray fluence was adapted to the changing width of the ROI cross-section and – in the case of the sbDBA – additionally to its lateral occurrence.

The optimized DBA trajectories were then used to compare the dose efficiency between the DBAs and current FFM solutions, including TCM and two kinds of bowtie filters as used in modern CT systems. In addition, the adjustable static operation mode of the z-sbDBA was evaluated. It holds the angular adjustment during the data acquisition at an angle that is optimized for the given imaging task beforehand. The evaluations demonstrated that the DBAs facilitate the imaging of the ROI at high image quality while effectively reducing the dose deposition in surrounding non-ROI tissue. While maintaining the ROI image quality, the DBAs enabled substantial dose savings compared to conventional bowtie filters: depending on the imaging task, the z-sbDBA reduced the patient radiation doses by about 15 % to 30 % compared to a regular bowtie filter. It is remarkable that even though the adjustable static z-sbDBA offers only a limited flexibility but thereby a simplified mechanic, it yielded comparable dose savings. The highly adjustable sbDBA achieved dose reductions of about 30 % to even 60 % relative to a regular bowtie filter.

This second part demonstrated, in summary, that the proposed DBAs combined with the developed trajectory optimization method can successfully enable a projection-wise, task- and patient-specific modulation of the x-ray fluence. The adaptive radiation exposures yielded a leap in dose efficiency compared to the bowtie filters of contemporary CT systems. Taking also practical considerations into account, the z-sbDBA is deemed to represent a reasonable balance between fluence adaptation and mechanical effort, well-suited for imaging centered ROIs. Particularly, the adjustable static operation mode of the z-sbDBA may be an simple solution that can be realized with limited effort.

Although some further development is required to enhance the maturity of the DBAs, the presented x-ray filter concepts "*are notable [...] in that they are the closest to being demonstrated in a diagnostic CT scanner*", as acknowledged by the associate editor[m] who accompanied the author's latest research article on the DBA evaluation.[158]

To conclude, two fundamentally new DBA concepts have been developed and successfully validated for FFM in x-ray CT imaging. The presented DBAs offer superior dose efficiency compared to state-of-the-art FFM technology. Unlike alternative DBA concepts, the benefits of the sbDBA and the z-sbDBA were demonstrated using physical prototypes installed in a clinical CT system. The promising results associated with the DBAs presented in this thesis will, hopefully, advance x-ray CT imaging by paving the way toward low-dose ROI imaging and elevating the "well-being and health" of future patients.

---

[m] Original extract of the written comment by the associate editor (unknown name) on the proposed DBA concepts in comparison to other DBA approaches. This statement was received during the revision of the author's journal paper on ROI imaging using the proposed DBAs, as reported in Huck et al. (2021).[158]

Bibliography

[1] *Declaration Of Geneva - The Physician's Pledge*. World Medical Association. 2017. URL: https://www.wma.net/policies-post/wma-declaration-of-geneva/ (visited on 04/16/2021).

[2] *Recommendations of the ICRP on Radiological Protection - Publication 87: Managing Patient Dose in Computed Tomography*. Vol. 30. 4. International Commission on Radiological Protection (ICRP), 2000. ISBN: 008-044-0835. URL: http://journals.sagepub.com/doi/pdf/10.1177/ANIB_30_4 (visited on 03/04/2021).

[3] *European Council Directive 2013/59/Euratom on basic safety standards for protection against the dangers arising from exposure to ionising radiation, and repealing Directives 89/618/Euratom, 90/641/Euratom, 96/29/Euratom, 97/43/Euratom and 2003/122/Euratom*. Council of the European Union, 2014. URL: https://eur-lex.europa.eu/legal-content/EN/TXT/PDF/?uri=CELEX:32013L0059&from=EN (visited on 03/04/2021).

[4] A. Trugenberger-Schnabel, A. Löbke-Renl, and J. Peter, eds. *Umweltradioaktivität und Strahlenbelastung: Jahresbericht 2014*. Bundesamt für Strahlenschutz (Bundesministerium für Umwelt, Naturschutz und nukleare Sicherheit), 2016. URL: http://nbn-resolving.de/urn:nbn:de:0221-2016091514109 (visited on 05/05/2021).

[5] A. Trugenberger-Schnabel, D. Merchel, A. Löbke-Renl, and J. Peter, eds. *Umweltradioaktivität und Strahlenbelastung: Jahresbericht 2018*. Bundesamt für Strahlenschutz (Bundesministerium für Umwelt, Naturschutz und nukleare Sicherheit), 2021. URL: https://doris.bfs.de/jspui/handle/urn:nbn:de:0221-2021011124821 (visited on 05/05/2021).

[6] *Radiation Protection no. 180: Medical Radiation Exposure of the European Population, Part 1*. European Commission, 2014. URL: https://ec.europa.eu/energy/sites/ener/files/documents/RP180.pdf (visited on 03/05/2021).

[7] C. H. McCollough, A. N. Primak, N. Braun, J. Kofler, L. Yu, and J. Christner. "Strategies for reducing radiation dose in CT". In: *Radiologic Clinics* 47.1 (2009), pp. 27–40. DOI: 10.1016/j.rcl.2008.10.006.

[8] C. H. McCollough, G. H. Chen, W. Kalender, S. Leng, E. Samei, K. Taguchi, G. Wang, L. Yu, and R. I. Pettigrew. "Achieving routine submillisievert CT scanning: report from the summit on management of radiation dose in CT". In: *Radiology* 264.2 (2012), pp. 567–580. DOI: 10.1148/radiol.12112265.

[9] N. J. Pelc. "Recent and future directions in CT imaging". In: *Annals of Biomedical Engineering* 42.2 (2014), pp. 260–268. DOI: 10.1007/s10439-014-0974-z.

[10] M. M. Lell and M. Kachelrieß. "Recent and upcoming technological developments in computed tomography: high speed, low dose, deep learning, multienergy". In: *Investigative Radiology* 55.1 (Jan. 2020), pp. 8–19. DOI: 10.1097/RLI.0000000000000601.

[11] H. Alkadhi and A. Euler. "The future of computed tomography: personalized, functional, and precise". In: *Investigative Radiology* 55.9 (Sept. 2020), pp. 545–555. DOI: 10.1097/RLI.0000000000000668.

[12] D. Wachabauer, S. Mathis-Edenhofer, and H. Moshammer. "Medical radiation exposure from radiological and interventional procedures in Austria". In: *Wiener klinische Wochenschrift* 132 (2019), pp. 563–571. DOI: 10.1007/s00508-019-01557-0.

[13] *Exposition de la population française aux rayonnements ionisants liée aux actes de diagnostic médical en 2012*. Institut de Radioprotection et de Sûreté Nucléaire, 2012. URL: https://www.irsn.fr/FR/expertise/rapports_expertise/radioprotection-homme/Pages/Rapport-IRSN-HOM-2014-006_Exposition-rayonnements-ionisants-diagnostic-medical.aspx#.YK9hBahLiUk (visited on 05/05/2021).

[14] *Exposure of the population to ionising radiation from diagnostic medical imaging procedures in France in 2017*. Institut de Radioprotection et de Sûreté Nucléaire, 2017. URL: https://www.irsn.fr/EN/publications/technical-publications/Documents/IRSN_Report-Expri_102020.pdf (visited on 05/05/2021).

[15] A. Aroua, E.-T. Samara, F. O. Bochud, R. Meuli, and F. R. Verdun. "Exposure of the Swiss population to computed tomography". In: *BMC medical imaging* 13.1 (2013), pp. 1–5. DOI: 10.1186/1471-2342-13-22.

[16] J. Bize, R. LeCoultre, A. Viry, and F. Verdun. "Strahlenexposition der Schweizer Bevölkerung durch Röntgendiagnostik 2018". In: (2018). URL: https://survey.raddose.ch/Raddose/media/edr2018-rapport-final-v14bis-2020-de.pdf.

[17] S. M. Huck. "Dynamic Beam attenuation in CT - Experimental Validation of a Novel Concept". MA thesis. Ludwig-Maximilians-Universität München, 2017.

[18] A. Oppelt. *Imaging Systems for Medical Diagnostics: Fundamentals, Technical Solutions and Applications for Systems Applying Ionizing Radiation, Nuclear Magnetic Resonance and Ultrasound*. Publicis MCD, 2005. ISBN: 978-3-895-78226-8.

[19] T. M. Buzug. *Computed Tomography - From Photon Statistics to Modern Cone-Beam CT*. Berlin Heidelberg: Springer Science & Business Media, 2008. ISBN: 978-3-540-39408-2.

[20] W. A. Kalender. *Computed Tomography: Fundamentals, System Technology, Image Quality, Applications*. John Wiley & Sons, 2011. ISBN: 978-3-895-78644-0.

[21] W. Schlegel, C. P. Karger, and O. Jäkel. *Medizinische Physik: Grundlagen - Bildgebung - Therapie - Technik*. 1. Aufl. Berlin Heidelberg New York: Springer-Verlag, 2018. ISBN: 978-3-662-54801-1.

[22] E. Samei and N. J. Pelc. *Computed Tomography - Approaches, Applications, and Operations*. 1st ed. Springer Nature, 2020. ISBN: 978-3-030-26957-9.

[23] W. A. Kalender. "X-ray computed tomography". In: *Physics in Medicine and Biology* 51.13 (2006), R29. DOI: 10.1088/0031-9155/51/13/R03.

[24] J. A. Seibert. "X-ray imaging physics for nuclear medicine technologists. Part 1: Basic principles of x-ray production". In: *Journal of Nuclear Medicine Technology* 32.3 (2004), pp. 139–147. URL: https://tech.snmjournals.org/content/jnmt/32/3/139.full.pdf.

[25] J. A. Seibert and J. M. Boone. "X-ray imaging physics for nuclear medicine technologists. Part 2: X-ray interactions and image formation". In: *Journal of Nuclear Medicine Technology* 33.1 (2005), pp. 3–18. URL: https://tech.snmjournals.org/content/jnmt/33/1/3.full.pdf.

[26] J. H. Hubbell. "Review of photon interaction cross section data in the medical and biological context". In: *Physics in Medicine and Biology* 44.1 (1999), R1. DOI: 10.1088/0031-9155/44/1/001.

[27] A. Wehnelt. "Über den Austritt negativer Ionen aus glühenden Metallverbindungen und damit zusammenhängende Erscheinungen". In: *Annalen der Physik* 319.8 (1904), pp. 425–468. DOI: 10.1002/andp.19043190802.

[28] W. Duane and F. L. Hunt. "Proceedings of the American Physical Society. On X-ray Wave-Lengths". In: *Phys. Rev.* 6 (Aug. 1915), p. 166. DOI: 10.1103/PhysRev.6.166.

[29] F. Tessier and I. Kawrakow. "Calculation of the electron–electron bremsstrahlung cross-section in the field of atomic electrons". In: *Nuclear Instruments and Methods in Physics Research Section B: Beam Interactions with Materials and Atoms* 266.4 (2008), pp. 625–634. DOI: 10.1016/j.nimb.2007.11.063.

[30] H. Krieger. *Grundlagen der Strahlungsphysik und des Strahlenschutzes*. 4th ed. Berlin Heidelberg: Springer Science & Business Media, 2012. ISBN: 978-3-834-81815-7. DOI: 10.1007/978-3-8348-2238-3.

[31] H. G. Moseley. "The high-frequency spectra of the elements". In: *The London, Edinburgh, and Dublin Philosophical Magazine and Journal of Science* 26.156 (1913), pp. 1024–1034. DOI: 10.1080/14786441308635052.

[32] A. Thompson et al. *X-Ray Data Booklet*. Lawrence Berkeley Laboratory, Berkeley, CA, USA, 2009. URL: https://xdb.lbl.gov/xdb-new.pdf.

[33] A. Einstein. "Über einen die Erzeugung und Verwandlung des Lichtes betreffenden heuristischen Gesichtspunkt". In: *Annalen der Physik* 322.6 (1905), pp. 132–148.

[34] P. Auger. "Sur l'effet photoélectrique composé". In: *Journal de Physique et le Radium* 6.6 (1925), pp. 205–208. DOI: 10.1051/jphysrad:0192500606020500.

[35] W. R. Hendee and E. R. Ritenour. *Medical Imaging Physics*. Ed. by 4. John Wiley & Sons, 2003. ISBN: 0-471-38226-4.

[36] D. R. White. "An analysis of the Z-dependence of photon and electron interactions". In: *Physics in Medicine and Biology* 22.2 (1977), p. 219. DOI: 10.1088/0031-9155/22/2/003.

[37] J. W. Strutt. "On the light from the sky, its polarization and colour". In: *The London, Edinburgh, and Dublin Philosophical Magazine and Journal of Science* 41.271 (1871), pp. 107–120. DOI: 10.1080/14786447108640452.

[38] J. W. Strutt. "On the light from the sky, its polarization and colour". In: *The London, Edinburgh, and Dublin Philosophical Magazine and Journal of Science* 41.273 (1871), pp. 274–279. DOI: 10.1080/14786447108640479.

[39] J. W. Strutt. "On the scattering of light by small particles". In: *The London, Edinburgh, and Dublin Philosophical Magazine and Journal of Science* 41.275 (1871), pp. 447–454. DOI: 10.1080/14786440408636055.

[40] J. J. Thomson. "On the structure of the atom: an investigation of the stability and periods of oscillation of a number of corpuscles arranged at equal intervals around the circumference of a circle; with application of the results to the theory of atomic structure". In: *The London, Edinburgh, and Dublin Philosophical Magazine and Journal of Science* 7.39 (1904), pp. 237–265. DOI: 10.1080/14786440409463107.

[41] A. H. Compton. "A quantum theory of the scattering of x-rays by light elements". In: *Physical Review* 21.5 (1923), p. 483. DOI: 10.1103/PhysRev.21.483.

[42] R. Speller and J. Horrocks. "Photon scattering - a 'new' source of information in medicine and biology?" In: *Physics in Medicine and Biology* 36.1 (1991), p. 1. DOI: 10.1088/0031-9155/36/1/001.

[43] O. Klein and Y. Nishina. "Über die Streuung von Strahlung durch freie Elektronen nach der neuen relativistischen Quantendynamik von Dirac". In: *Zeitschrift für Physik* 52.11-12 (1929), pp. 853–868. DOI: 10.1007/BF01366453.

[44] P. Bouguer. *Essai d'optique sur la gradation de la lumière*. Claude Jombert, 1729. DOI: 10.1259/jrs.1922.0026.

[45] J. H. Lambert. *Lamberts Photometrie: photometria, sive de mensura et gradibus luminis, colorum et umbrae*. Wilhelm Engelmann Verlag, 1760.

[46] A. Beer. "Bestimmung der absorption des rothen Lichts in farbigen Flüssigkeiten". In: *Annalen der Physik und Chemie* 86.1 (1852), pp. 78–88. DOI: 10.1002/andp.18521620505.

[47] T. Laubenberger and J. Laubenberger. *Technik der medizinischen Radiologie: Diagnostik, Strahlentherapie, Strahlenschutz; für Ärzte, Medizinstudenten und MTRA*. 7th edition. Deutscher Ärzteverlag, Jan. 1999. ISBN: 978-3769111323.

[48] J. Hsieh. *Computed Tomography Principles, Design, Artifacts, and Recent Advances*. Ed. by 2. SPIE. John Wiley & Sons, 2009. ISBN: 978-0-8194-7533-6.

[49] H. Alkadhi, S. Leschka, P. Stolzmann, and H. Scheffel. *Wie funktioniert CT?* Berlin Heidelberg New York: Springer-Verlag, 2011. ISBN: 978-3-642-17803-0.

[50] W. C. Röntgen. "On a new kind of rays". In: *Science* 3.59 (1896), pp. 227–231.

[51] J. Radon. "Über die Bestimmung von Funktionen durch ihre Integralwerte längs gewisser Mannigfaltigkeiten". In: *Berichte über die Verhandlungen der Königlich-Sächsischen Gesellschaft der Wissenschaften zu Leipzig* 69 (1917). Ed. by Königlich Sächsische Gesellschaft der Wissenschaften, pp. 262–277.

[52] A. M. Cormack. "Representation of a function by its line integrals, with some radiological applications". In: *Journal of Applied Physics* 34.9 (1963), pp. 2722–2727. DOI: 10.1063/1.1729798.

[53] A. M. Cormack. "Representation of a function by its line integrals, with some radiological applications. II". In: *Journal of Applied Physics* 35.10 (1964), pp. 2908–2913. DOI: 10.1063/1.1713127.

[54] W. H. Oldendorf. "Isolated flying spot detection of radiodensity dis-continuities-displaying the internal structural pattern of a complex object". In: *IRE transactions on bio-medical electronics* 8.1 (1961), pp. 68–72. DOI: 10.1109/TBMEL.1961.4322854.

[55] G. N. Hounsfield. "Computerized transverse axial scanning (tomography): Part 1. Description of system". In: *The British Journal of Radiology* 46.552 (1973), pp. 1016–1022. DOI: 10.1259/0007-1285-46-552-1016.

[56] W. Kalender, W. Seissler, and P. Vock. "Single-breath-hold spiral volumetric CT by continuous patient translation and scanner rotation". In: *Proceedings of the 75th anniversary scientific assembly and annual meeting Radiological Society of North America*. Vol. 173. 1989, p. 414. URL: https://inis.iaea.org/search/search.aspx?orig_q=RN:21087158.

[57] W. A. Kalender, W. Seissler, E. Klotz, and P. Vock. "Spiral volumetric CT with single-breath-hold technique, continuous transport, and continuous scanner rotation". In: *Radiology* 176.1 (1990), pp. 181–183. DOI: 10.1148/radiology.176.1.2353088.

[58] T. G. Flohr, S. Schaller, K. Stierstorfer, H. Bruder, B. M. Ohnesorge, and U. J. Schoepf. "Multi–detector row CT systems and image-reconstruction techniques". In: *Radiology* 235.3 (2005), pp. 756–773. DOI: 10.1148/radiol.2353040037.

[59] T. G. Flohr et al. "First performance evaluation of a dual-source CT (DSCT) system". In: *European Radiology* 16.2 (2006), pp. 256–268. DOI: 10.1007/s00330-005-2919-2.

[60] H. in Europe. *Zurück in die Zukunft - Eine Reise durch die Geschichte der Computertomographie von damals bis heute*. 2012. URL: https://healthcare-in-europe.com/de/news/2012-zurueck-in-die-zukunft.html (visited on 03/18/2021).

[61] M. M. Lell, J. E. Wildberger, H. Alkadhi, J. Damilakis, and M. Kachelriess. "Evolution in computed tomography: The battle for speed and dose". In: *Investigative Radiology* 50.9 (2015), pp. 629–644. DOI: 10.1097/RLI.0000000000000172.

[62] S. Dirnberger, K. Schroll-Bakes, M. Schusser, and I. Zenger. *Die Geschichte der Röntgentechnik bei Siemens Healthineers*. Ed. by S. H. H. Institute. Siemens Healthcare GmbH, 2020. URL: https://www.medmuseum.siemens-healthineers.com/publikationen (visited on 03/19/2021).

[63] R. A. Brooks and G. Di Chiro. "Statistical limitations in x-ray reconstructive tomography". In: *Medical Physics* 3.4 (1976), pp. 237–240. DOI: 10.1118/1.594240.

[64] H. D. Nagel. "CT parameters that influence the radiation dose". In: *Radiation dose from adult and pediatric multidetector computed tomography*. Springer, 2007, pp. 51–79. DOI: 10.1007/978-3-540-68575-3_4.

[65] J. Baek and N. J. Pelc. "The noise power spectrum in CT with direct fan beam reconstruction". In: *Medical Physics* 37.5 (2010), pp. 2074–2081. DOI: 10.1118/1.3378673.

[66] K. Stierstorfer and M. Spahn. "Self-normalizing method to measure the detective quantum efficiency of a wide range of x-ray detectors". In: *Medical Physics* 26.7 (1999), pp. 1312–1319. DOI: 10.1118/1.598626.

[67] E. Samei and E. Krupinski. *The Handbook of Medical Image Perception and Techniques*. Ed. by 2. Cambridge University Press, 2009. ISBN: 978-0-521-51392-0.

[68] J. H. Siewerdsen and D. A. Jaffray. "Cone-beam computed tomography with a flat-panel imager: magnitude and effects of x-ray scatter". In: *Medical Physics* 28.2 (Feb. 2001), pp. 220–231. DOI: 10.1118/1.1339879.

[69] P. M. Joseph and R. D. Spital. "The effects of scatter in x-ray computed tomography". In: *Medical Physics* 9.4 (1982), pp. 464–472. DOI: 10.1118/1.595111.

[70] *Recommendations of the ICRP on Radiological Protection - Publication 103*. Vol. 37. 2-4. International Commission on Radiological Protection (ICRP), 2007. URL: http://journals.sagepub.com/doi/pdf/10.1177/ANIB_37_2-4.

[71] W. Jacobi. "The concept of the effective dose a proposal for the combination of organ doses". In: *Radiation and environmental biophysics* 12.2 (1975), pp. 101–109. DOI: 10.1007/BF01328971.

[72] C. H. McCollough and B. A. Schueler. "Calculation of effective dose". In: *Medical Physics* 27.5 (2000), pp. 828–837. DOI: 10.1118/1.598948.

[73] L. Yu, X. Liu, S. Leng, J. M. Kofler, J. C. Ramirez-Giraldo, M. Qu, J. Christner, J. G. Fletcher, and C. H. McCollough. "Radiation dose reduction in computed tomography: techniques and future perspective". In: *Imaging in Medicine* 1.1 (Oct. 2009), p. 65. DOI: 10.2217/iim.09.5.

[74] *Recommendations of the ICRP on Radiological Protection - Publication 60*. Vol. 21. 1-3. International Commission on Radiological Protection (ICRP), 1991. URL: http://journals.sagepub.com/doi/pdf/10.1177/ANIB_21_1-3.

[75] *Radiation Protection N° 178: Referral Guidelines for Medical Imaging - Availability and Use in the European Union*. European Commission. 2014. URL: https://ec.europa.eu/energy/sites/ener/files/documents/178.pdf (visited on 04/11/2021).

[76] *Appropriateness Criteria*. American College of Radiology. URL: https://acsearch.acr.org/list (visited on 03/05/2021).

[77] M. K. Kalra, M. M. Maher, T. L. Toth, L. M. Hamberg, M. A. Blake, J.-A. Shepard, and S. Saini. "Strategies for CT radiation dose optimization". In: *Radiology* 230.3 (2004), pp. 619–628. DOI: 10.1148/radiol.2303021726.

[78] K. Stierstorfer, U. Kuhn, H. Wolf, M. Petersilka, C. Suess, and T. Flohr. "Principle and performance of a dynamic collimation technique for spiral CT". In: *93rd Radiological Society of North America Annual Meeting. Chicago, IL, USA*. Nov. 2007, pp. 25–30. URL: http://archive.rsna.org/2007/5006895.html.

[79] J. A. Christner, V. A. Zavaletta, C. D. Eusemann, A. I. Walz-Flannigan, and C. H. McCollough. "Dose reduction in helical CT: dynamically adjustable z-axis X-ray beam collimation". In: *American Journal of Roentgenology* 194.1 (2010), W49–W55. DOI: 10.2214/AJR.09.2878.

[80] A. B. Sigal-Cinqualbre, R. Hennequin, H. T. Abada, X. Chen, and J.-F. Paul. "Low-kilovoltage multi–detector row chest CT in adults: feasibility and effect on image quality and iodine dose". In: *Radiology* 231.1 (2004), pp. 169–174. DOI: 10.1148/radiol.2311030191.

[81] Y. Nakayama et al. "Abdominal CT with low tube voltage: preliminary observations about radiation dose, contrast enhancement, image quality, and noise". In: *Radiology* 237.3 (2005), pp. 945–951. DOI: 10.1148/radiol.2373041655.

[82] Y. Funama et al. "Radiation dose reduction without degradation of low-contrast detectability at abdominal multisection CT with a low–tube voltage technique: phantom study". In: *Radiology* 237.3 (2005), pp. 905–910. DOI: 10.1148/radiol.2373041643.

[83] J. G. Fletcher, N. Takahashi, R. Hartman, L. Guimaraes, J. E. Huprich, D. M. Hough, L. Yu, and C. H. McCollough. "Dual-energy and dual-source CT: is there a role in the abdomen and pelvis?" In: *Radiologic clinics of North America* 47.1 (2009), pp. 41–57. DOI: 10.1016/j.rcl.2008.10.003.

[84] J. R. Haaga, F. Miraldi, W. Macintyre, J. P. LiPuma, P. J. Bryan, and E. Wiesen. "The effect of mAs variation upon computed tomography image quality as evaluated by in vivo and in vitro studies." In: *Radiology* 138.2 (1981), pp. 449–454. DOI: 10.1148/radiology.138.2.7455129.

[85] W. A. Kalender, H. Wolf, C. Suess, M. Gies, H. Greess, and W. A. Bautz. "Dose reduction in CT by on-line tube current control: principles and validation on phantoms and cadavers". In: *European Radiology* 9.2 (1999), pp. 323–328. DOI: 10.1007/s003300050674.

[86] T. L. Toth. "Dose reduction opportunities for CT scanners". In: *Pediatric Radiology* 32.4 (2002), p. 261. DOI: 10.1007/s00247-002-0678-7.

[87] L. Kopka, M. Funke, N. Breiter, K. Hermann, R. Vosshenrich, and E. Grabbe. "An anatomically adapted variation of the tube current in CT. Studies on radiation dosage reduction and image quality". In: *RöFo: Fortschritte auf dem Gebiet der Röntgenstrahlen und der Nuklearmedizin* 163.5 (1995), pp. 383–387. DOI: 10.1055/s-2007-1016013.

[88] S. M. Giacomuzzi, B. Erckert, T. Schöpf, M. C. Freund, P. Springer, A. Dessl, and W. Jaschke. "The smart-scan procedure of spiral computed tomography. A new method for dose reduction". In: *RöFo: Fortschritte auf dem Gebiet der Röntgenstrahlen und der Nuklearmedizin* 165.1 (1996), pp. 10–16. DOI: 10.1055/s-2007-1015707.

[89] M. Gies, W. A. Kalender, H. Wolf, C. Suess, and M. T. Madsen. "Dose reduction in CT by anatomically adapted tube current modulation. I. Simulation studies". In: *Medical Physics* 26.11 (1999), pp. 2235–2247. DOI: 10.1118/1.598779.

[90] W. A. Kalender, H. Wolf, and C. Suess. "Dose reduction in CT by anatomically adapted tube current modulation. II. Phantom measurements". In: *Medical Physics* 26.11 (1999), pp. 2248–2253. DOI: 10.1118/1.598738.

[91] S. Ulzheimer, H. Endt, and T. Flohr. "Computed tomography - patient dose and dose reduction technologies". In: *Health physics* 100.3 (2011), pp. 325–328. DOI: 10.1097/HP.0b013e318209635e.

[92] S. M. Huck, G. S.-K. Fung, K. Parodi, and K. Stierstorfer. "A method for optimization of the x-ray tube current in ROI imaging using a simulation framework for radiation dose and image quality calculation for arbitrary fluence distributions". In: *Medical Imaging 2021: Physics of Medical Imaging*. Ed. by H. Bosmans, W. Zhao, and L. Yu. Vol. 11595. International Society for Optics and Photonics (SPIE). San Diego, CA, USA (online), Feb. 2021, pp. 11–21. DOI: 10.1117/12.2580828.

[93] C. Hohl, C. Suess, J. E. Wildberger, D. Honnef, M. Das, G. Mühlenbruch, A. Schaller, R. W. Gunther, and A. H. Mahnken. "Dose reduction during CT fluoroscopy: phantom study of angular beam modulation". In: *Radiology* 246.2 (2008), pp. 519–525. DOI: 10.1148/radiol.2462061968.

[94] A. Seidenfuss, A. Mayr, M. Schmid, M. Uder, and M. M. Lell. "Dose reduction of the female breast in chest CT". In: *American Journal of Roentgenology* 202.5 (2014), W447–W452. DOI: 10.2214/AJR.13.10541.

[95] K. M. Hanson. "Spectral analysis of non-stationary CT noise". In: *Int. Symposium and Course on Computed Tomography*. Apr. 1980. URL: https://kmh-lanl.hansonhub.com/talks/ct80.abs.html (visited on 01/26/2020).

[96] T. L. Toth, E. Cesmeli, A. Ikhlef, and T. Horiuchi. "Image quality and dose optimization using novel x-ray source filters tailored to patient size". In: *Medical Imaging 2005: Physics of Medical Imaging*. Vol. 5745. International Society for Optics and Photonics. 2005, pp. 283–291. DOI: 10.1117/12.595465.

[97] S. Graham, D. Moseley, J. Siewerdsen, and D. Jaffray. "Compensators for dose and scatter management in cone-beam computed tomography". In: *Medical Physics* 34.7 (2007), pp. 2691–2703. DOI: 10.1118/1.2740466.

[98] J. T. Bushberg and J. M. Boone. *The Essential Physics of Medical Imaging*. 3rd ed. Lippincott Williams & Wilkins, 2011. ISBN: 978-0-7817-8057-5.

[99] N. Mail, D. Moseley, J. H. Siewerdsen, and D. Jaffray. "The influence of bowtie filtration on cone-beam CT image quality". In: *Medical Physics* 36.1 (2009), pp. 22–32. DOI: 10.1118/1.3017470.

[100] F. Lück, D. Kolditz, M. Hupfer, and W. A. Kalender. "Effect of shaped filter design on dose and image quality in breast CT". In: *Physics in Medicine and Biology* 58.12 (2013), p. 4205. DOI: 10.1088/0031-9155/58/12/4205.

[101] S. A. Graham, J. H. Siewerdsen, and D. A. Jaffray. "Intensity-modulated fluence patterns for task-specific imaging in cone-beam CT". In: *Medical Imaging 2007: Physics of Medical Imaging*. Vol. 6510. International Society for Optics and Photonics. 2007, p. 651003. DOI: 10.1117/12.713724.

[102] T. P. Szczykutowicz and C. Mistretta. "Practical considerations for intensity modulated CT". In: *Medical Imaging 2012: Physics of Medical Imaging*. International Society for Optics and Photonics. 2012, 83134E–83134E. DOI: 10.1117/12.911355.

[103] S. Bartolac, S. Graham, J. Siewerdsen, and D. Jaffray. "Fluence field optimization for noise and dose objectives in CT". In: *Medical Physics* 38.1 (2011), pp. 2–17. DOI: 10.1118/1.3574885.

[104] S. M. Huck, G. S.-K. Fung, K. Parodi, and K. Stierstorfer. "Sheet-based dynamic beam attenuator – A novel concept for dynamic fluence field modulation in x-ray CT". In: *Medical Physics* 46.12 (2019), pp. 5528–5537. DOI: 10.1002/mp.13690.

[105] T. G. Schmidt, R. Fahrig, N. J. Pelc, and E. G. Solomon. "An inverse-geometry volumetric CT system with a large-area scanned source: A feasibility study". In: *Medical Physics* 31.9 (2004), pp. 2623–2627. DOI: 10.1118/1.1786171.

[106] J. Sperl, D. Beque, B. Claus, B. De Man, B. Senzig, and M. Brokate. "Computer-assisted scan protocol and reconstruction (CASPAR) – Reduction of image noise and patient dose". In: *IEEE Transactions on Medical Imaging* 29.3 (2010), pp. 724–732. DOI: 10.1109/TMI.2009.2034515.

[107] T. L. Toth, E. J. Tkaczyk, and J. Hsieh. *Method and apparatus of radiographic imaging with an energy beam tailored for a subject to be scanned*. US Patent 7,076,029 B2. General Electric, July 2006.

[108] M. Yahata, A. Izuhara, and M. Maida. *X-ray distribution adjusting filter apparatus and X-ray CT apparatus using the same*. US Patent 7,082,189 B2. General Electric, July 2006.

[109] D. M. Hoffman. *Rotatable filter for a pre-subject CT collimator having multiple filtering profiles*. US Patent 7,046,756 B2. General Electric, May 2006.

[110] J. S. Arenson, D. Ruimi, O. Meirav, and R. H. Armstrong. *X-ray flux management device*. US Patent 7,330,535 B2. General Electric, Feb. 2008.

[111] S. S. Hsieh and N. J. Pelc. "The feasibility of a piecewise-linear dynamic bowtie filter". In: *Medical Physics* 40.3 (Mar. 2013), p. 031910. DOI: 10.1118/1.4789630.

[112] S. S. Hsieh, D. Fleischmann, and N. J. Pelc. "Dose reduction using a dynamic, piecewise-linear attenuator." In: *Medical Physics* 41.2 (Feb. 2014), p. 021910. DOI: 10.1118/1.4862079.

[113] T. P. Szczykutowicz and C. A. Mistretta. "Design of a digital beam attenuation system for computed tomography: Part I. System design and simulation framework." In: *Medical Physics* 40.2 (Feb. 2013), p. 021905. DOI: 10.1118/1.4773879.

[114] T. P. Szczykutowicz and C. A. Mistretta. "Design of a digital beam attenuation system for computed tomography. Part II. Performance study and initial results." In: *Medical Physics* 40.2 (Feb. 2013), p. 021906. DOI: 10.1118/1.598738.

[115] F. Franz, L. Hans, and S. R. Franz. *Adaptives Röntgenfilter und Verfahren zur Adaptiven Schwächung einer Röntgenstrahlung*. German Patent DE 10 2012 206 953 B3. Siemens AG, Apr. 2012.

[116] V. V. Mohandas. "Adaptable Collimator - A Simulation Approach". MA thesis. RWTH Aachen, 2018.

[117] P. Shunhavanich, S. S. Hsieh, and N. J. Pelc. "Fluid-filled dynamic bowtie filter: Description and comparison with other modulators". In: *Medical Physics* 46.1 (2019), pp. 127–139. DOI: 10.1002/mp.13272.

[118] A. J. Mathews, T. Steven, G. Gang, S. Kawamoto, W. Zbijewski, J. H. Siewerdsen, R. Levinson, and J. W. Stayman. "Design of dual multiple aperture devices for dynamical fluence field modulated CT". In: *CT-Meeting: Fifth International Conference on Image Formation in X-Ray Computed Tomography*. Ed. by F. Noo. Salt Lake City, UT, USA, May 2016, pp. 29–32. URL: https://www.ct-meeting.org/data/ProceedingsCTMeeting2018.pdf.

[119] J. W. Stayman, A. Mathews, W. Zbijewski, G. Gang, J. Siewerdsen, S. Kawamoto, I. Blevis, and R. Levinson. "Fluence-field modulated x-ray CT using multiple aperture devices". In: *Medical Imaging 2016: Physics of Medical Imaging*. Vol. 9783. International Society for Optics and Photonics. 2016, p. 97830X. DOI: 10.1117/12.2214358.

[120] G. J. Gang, A. Mao, W. Wang, J. H. Siewerdsen, A. Mathews, S. Kawamoto, R. Levinson, and J. W. Stayman. "Dynamic fluence field modulation in computed tomography using multiple aperture devices". In: *Physics in Medicine and Biology* 64.10 (2019), p. 105024. DOI: 10.1088/1361-6560/ab155e.

[121] S. Bartolac and D. Jaffray. "Compensator models for fluence field modulated computed tomography". In: *Medical Physics* 40.12 (2013), p. 121909. DOI: 10.1118/1.4829513.

[122] S. S. Hsieh and N. J. Pelc. "Control algorithms for dynamic attenuators". In: *Medical Physics* 41.6 (2014). DOI: 10.1118/1.4875727.

[123] W. Stiller, L. Veloza, G. Pahn, and H.-U. Kauczor. "A theoretical model for calculating MDCT beam-shaping filter geometry: Comparison of calculated attenuation profile and Monte-Carlo simulated transmission spectra to measurements (WE-C-110-09)". In: *97th Radiological Society of North America Annual Meeting. Chicago, IL, USA*. 2011. DOI: 10.1118/1.3613348.

[124] G. J. Gang, J. H. Siewerdsen, and J. W. Stayman. "Task-Driven optimization of fField and regularization for model-based iterative reconstruction in computed tomography". In: *IEEE Transactions on Medical Imaging* 36.12 (2017), pp. 2424–2435. DOI: 10.1109/TMI.2017.2763538.

[125] A. Mao, G. J. Gang, W. Shyr, R. Levinson, J. H. Siewerdsen, S. Kawamoto, and J. W. Stayman. "Dynamic fluence field modulation for miscentered patients in computed tomography". In: *Journal of Medical Imaging* 5.4 (2018), p. 043501. DOI: 10.1117/1.JMI.5.4.043501.

[126] W. Wang, G. J. Gang, A. Mao, A. Sisniega, J. H. Siewerdsen, and J. W. Stayman. "Volume-of-interest (VOI) CT imaging with dynamic beam filtering using multiple aperture devices". In: *CT-Meeting: Fifth International Conference on Image Formation in X-Ray Computed Tomography*. Ed. by F. Noo. Salt Lake City, UT, USA, May 2018, pp. 213–217. URL: https://www.ct-meeting.org/data/ProceedingsCTMeeting2018.pdf.

[127] W. Wang, G. J. Gang, J. H. Siewerdsen, R. Levinson, S. Kawamoto, and J. W. Stayman. "Volume-of-interest imaging with dynamic fluence modulation using multiple aperture devices". In: *Journal of Medical Imaging* 6.3 (2019), p. 033504. DOI: 10.1117/1.JMI.6.3.033504.

[128] R. N. Chityala, K. R. Hoffmann, D. R. Bednarek, and S. Rudin. "Region of interest (ROI) computed tomography". In: *Medical Imaging 2004: Physics of Medical Imaging*. Vol. 5368. International Society for Optics and Photonics. 2004, pp. 534–541. DOI: 10.1117/12.534568.

[129] D. Heuscher and F. Noo. "CT dose reduction using dynamic collimation". In: *CT-Meeting: Second International Conference on Image Formation in X-Ray Computed Tomography*. Ed. by F. Noo. Salt Lake City, UT, USA, 2012, pp. 115–118. URL: https://www.ct-meeting.org/data/ProceedingsCTMeeting2012.pdf.

[130] B. Oktay and F. Noo. "Reduction of dose by focusing the x-Ray beam to a specific region of interest: Monte Carlo assessment". In: *CT-Meeting: Third International Conference on Image Formation in X-Ray Computed Tomography*. Ed. by F. Noo. Salt Lake City, UT, USA, 2014, pp. 279–282. URL: https://www.ct-meeting.org/data/ProceedingsCTMeeting2014.pdf.

[131] S. Veloza. "Experimental Dosimetry and Simulation of Computed Tomography Radiation Exposure: Approaches for Dose Reduction". PhD thesis. Ruprecht-Karls-Universität Heidelberg, 2012.

[132] W. Stiller, S. Veloza, and H.-U. Kauczor. "Attenuation-based dynamic CT beam-shaping filtration in dependence of fan and projection angle: Evaluation of a new method for radiation exposure reduction by Monte-Carlo simulation of spatial dose distribution". In: *NSS/MIC, IEEE*. IEEE. 2012, pp. 2625–2632. DOI: 10.1109/NSSMIC.2012.6551599.

[133] T. P. Szczykutowicz and C. Mistretta. "Volume of interest CT implemented with a dynamic bowtie filter". In: *Medical Imaging 2013: Physics of Medical Imaging*. Vol. 8668. International Society for Optics and Photonics. 2013, 86682R. DOI: 10.1117/12.2005924.

[134] D. Kolditz, Y. Kyriakou, and W. A. Kalender. "Volume-of-interest (VOI) imaging in C-arm flat-detector CT for high image quality at reduced dose". In: *Medical Physics* 37.6 (2010), pp. 2719–2730. DOI: 10.1118/1.3427641.

[135] T. P. Szczykutowicz and C. A. Mistretta. "Experimental realization of fluence field modulated CT using digital beam attenuation". In: *Physics in Medicine and Biology* 59.5 (2014), p. 1305. DOI: 10.1088/0031-9155/59/5/1305.

[136] S. Bartolac, S. Graham, J. Siewerdsen, and D. Jaffray. "Compensator approaches for intensity modulated computed tomography". In: *CT-Meeting: First International Conference on Image Formation in X-Ray Computed Tomography*. Ed. by F. Noo. CT Meeting. Salt Lake City, UT, USA, 2010, pp. 101–104. URL: https://www.ct-meeting.org/data/ProceedingsCTMeeting2010.pdf.

[137] W. Wang, G. J. Gang, J. H. Siewerdsen, and J. W. Stayman. "Volume-of-interest imaging using multiple aperture devices". In: *Medical Imaging 2019: Physics of Medical Imaging*. Ed. by T. G. Schmidt, G.-H. Chen, and H. Bosmans. Vol. 10948. International Society for Optics and Photonics. SPIE, 2019, pp. 533–538. DOI: 10.1117/12.2513427.

[138] J. R. Hermus and T. P. Szczykutowicz. "Two-dimensional dynamic fluid bowtie attenuators". In: *Journal of Medical Imaging* 3.1 (2016), pp. 013502–013502. DOI: 10.1117/1.JMI.3.1.013502.

[139] P. Shunhavanich, S. S. Hsieh, and N. J. Pelc. "Fluid-filled dynamic bowtie filter: a feasibility study". In: *Medical Imaging 2015: Physics of Medical Imaging*. Vol. 9412. International Society for Optics and Photonics. 2015, p. 94121L. DOI: 10.1117/12.2081673.

[140] F. Liu, G. Wang, W. Cong, S. S. Hsieh, and N. J. Pelc. "Dynamic bowtie for fan-beam CT". In: *Journal of X-ray Science and Technology* 21.4 (2013), pp. 579–590. DOI: 10.3233/XST-130386.

[141] S. S. Hsieh, M. V. Peng, C. A. May, P. Shunhavanich, D. Fleischmann, and N. J. Pelc. "A prototype piecewise-linear dynamic attenuator". In: *Physics in Medicine and Biology* 61.13 (2016), pp. 4974–4988. DOI: 10.1088/0031-9155/61/13/4974.

[142] S. S. Hsieh and N. J. Pelc. *Computed tomography system with dynamic bowtie filter*. US Patent 9,521,982 B2. The Board of Trustees of the Leland Stanford Junior University, Dec. 2016.

[143] T. P. Szczykutowicz and J. Hermus. "Fluid dynamic bowtie attenuators". In: *Medical Imaging 2015: Physics of Medical Imaging*. International Society for Optics and Photonics. 2015, p. 94120X. DOI: 10.1117/12.2077618.

[144] K. Stierstorfer. *Verfahren und Vorrichtung zum Einstellen eines räumlichen Absorptionsprofils eines Röntgenstrahls in einem Computertomographen*. German Patent DE 10 2016 213 990 B4. Siemens Healthcare GmbH, Feb. 2019.

[145] S. M. Huck and K. Stierstorfer. *Verfahren und Vorrichtung zum Einstellen einer räumlichen Intensitätsverteilung eines Röntgenstrahls*. International Patent Application WO 2019/161953 A1. Siemens Healthcare GmbH, July 2018.

[146] S. M. Huck, G. S.-K. Fung, K. Parodi, and K. Stierstorfer. "The z-sbDBA, a new concept for a dynamic sheet-based fluence field modulator in x-ray CT". In: *Medical Physics* 47.10 (2020), pp. 4827–4837. DOI: 10.1002/mp.14430.

[147] S. M. Huck, K. Parodi, and K. Stierstorfer. "First experimental validation of a novel concept for dynamic beam attenuation in CT". In: *CT-Meeting: Fifth International Conference on Image Formation in X-Ray Computed Tomography*. Ed. by F. Noo. Salt Lake City, UT, USA, May 2018, pp. 24–27. URL: https://www.ct-meeting.org/data/ProceedingsCTMeeting2018.pdf.

[148] S. M. Huck, G. S. K. Fung, K. Parodi, and K. Stierstorfer. "A new concept for fluence field modulation in x-ray CT: the z-sbDBA". In: *Medical Imaging 2020: Physics of Medical Imaging*. Ed. by G.-H. Chen and H. Bosmans. Vol. 11312. International Society for Optics and Photonics (SPIE). Houston, TX, USA, Feb. 2020, pp. 1–6. DOI: 10.1117/12.2543185.

[149] S. M. Huck and K. Stierstorfer. *Fokussierungsmodul für einen Formfilter und Formfilter zum Einstellen einer räumlichen Intensitätsverteilung eines Röntgenstrahls*. European Patent Application EP 3 217 408 A2. Siemens Healthcare GmbH, May 2017.

[150] S. H. GmbH. *SOMATOM Force – Technical specification*. Forchheim, Germany, 2017. URL: https://www.siemens-healthineers.com/computed-tomography/dual-source-ct/somatom-force (visited on 08/27/2020).

[151] Swiss Precision Instruments Inc. *SPI TRONIC Pro 360 Digital Level – Owner's Manual*. La Palma, CA, USA, 2016.

[152] Y. Kyriakou and W. A. Kalender. "Intensity distribution and impact of scatter for dual-source CT". In: *Physics in Medicine and Biology* 52.23 (2007), p. 6969. DOI: 10.1088/0031-9155/52/23/014.

[153] M. Petersilka, K. Stierstorfer, H. Bruder, and T. Flohr. "Strategies for scatter correction in dual source CT". In: *Medical Physics* 37.11 (2010), pp. 5971–5992. DOI: 10.1118/1.3504606.

[154] P. Prakash and J. M. Boudry. "Comparative study of bowtie and patient scatter in diagnostic CT". In: *Medical Imaging 2017: Physics of Medical Imaging*. Ed. by T. G. Flohr, J. Y. Lo, and T. G. Schmidt. Vol. 10132. International Society for Optics and Photonics. 2017, pp. 627–634. DOI: 10.1117/12.2253012.

[155] H. P. Chan and K. Doi. "The validity of Monte Carlo simulation in studies of scattered radiation in diagnostic radiology." In: *Physics in Medicine and Biology* 28.2 (Feb. 1983), pp. 109–29. DOI: 10.1088/0031-9155/28/2/001.

[156] Siemens Healthcare GmbH. "A Validation of MOCASSIM". Internal report (unpublished). Forchheim, Germany, 1992.

[157] S. Kappler, D. Niederlöhner, S. Wirth, and K. Stierstorfer. "A full-system simulation chain for computed tomography scanners". In: *Nuclear Science Symposium and Medical Imaging Conference (NSS/MIC)*. IEEE. 2009, pp. 3433–3436. DOI: 10.1109/NSSMIC.2009.5401779.

[158] S. M. Huck, G. S.-K. Fung, K. Parodi, and K. Stierstorfer. "On the potential of ROI imaging in x-ray CT - A comparison of novel dynamic beam attenuators with current technology". In: *Medical Physics* (2021). In Press. DOI: 10.1002/MP.14879.

[159] S. M. Huck, G. S.-K. Fung, K. Parodi, and K. Stierstorfer. "Fluence field modulation in x-ray CT for ROI imaging: Optimization of primary fluence and comparison of attenuator scenarios". In: *CT-Meeting: Sixth International Conference on Image Formation in X-Ray Computed Tomography*. Ed. by M. Kachelrieß. Regensburg, Germany (online), Aug. 2020, pp. 214–217. URL: https://www.ct-meeting.org/data/ProceedingsCTMeeting2020.pdf.

[160] B. F. für Medizinische Bildgebung und Bildverarbeitung (FORBILD). URL: http://www.imp.uni-erlangen.de/forbild (visited on 02/08/2020).

[161] W. Fu, X. Tian, G. M. Sturgeon, G. Agasthya, W. P. Segars, M. M. Goodsitt, E. A. Kazerooni, and E. Samei. "CT breast dose reduction with the use of breast positioning and organ-based tube current modulation". In: *Medical Physics* 44.2 (2017), pp. 665–678. DOI: 10.1002/mp.12076.

[162] A. C. Kak and M. Slaney. *Principles of Computerized Tomographic Imaging*. SIAM, 2001. ISBN: 978-0-898-71494-4. DOI: 10.1137/1.9780898719277.

[163] W. A. Kalender, S. Buchenau, P. Deak, M. Kellermeier, O. Langner, M. van Straten, S. Vollmar, and S. Wilharm. "Technical approaches to the optimisation of CT". In: *Physica Medica* 24.2 (2008), pp. 71–79. DOI: 10.1016/j.ejmp.2008.01.012.

[164] K. Matsubara, H. Kawashima, T. Chusin, and R. Okubo. "How to optimize radiation dose in computed tomography examinations: available methods and techniques". In: *Medical Physics International Journal* 5.2 (2017).

[165] *Basic Anatomical and Physiological Data for Use in Radiological Protection: Reference values - Publication 89*. Vol. 32. 3-4. International Commission on Radiological Protection (ICRP), 2002, pp. 1–277. URL: http://journals.sagepub.com/doi/pdf/10.1177/ANIB_32_3-4.

[166] M. D. Harpen. "A simple theorem relating noise and patient dose in computed tomography". In: *Medical Physics* 26.11 (1999), pp. 2231–2234. DOI: 10.1118/1.598778.

[167] J. W. Hayes, D. Gomez-Cardona, R. Zhang, K. Li, J. P. Cruz-Bastida, and G.-H. Chen. "Low-dose CBCT via raw counts domain low-signal correction schemes: Performance assessment and task-based parameter optimization (Part I: Assessment of spatial resolution and noise performance)". In: *Medical Physics* 45.5 (2018), pp. 1942–1956. DOI: 10.1002/mp.12856.

[168] L. Chen, C. K. Abbey, and J. M. Boone. "Association between power law coefficients of the anatomical noise power spectrum and lesion detectability in breast imaging modalities". In: *Physics in Medicine and Biology* 58.6 (2013), p. 1663. DOI: 10.1088/0031-9155/58/6/1663.

[169] E. Samei and M. J. Flynn. "An experimental comparison of detector performance for computed radiography systems". In: *Medical Physics* 29.4 (2002), pp. 447–459. DOI: 10.1118/1.1449873.

[170] E. Samei and M. J. Flynn. "An experimental comparison of detector performance for direct and indirect digital radiography systems". In: *Medical Physics* 30.4 (2003), pp. 608–622. DOI: 10.1118/1.1561285.

[171] B. Ohnesorge, T. Flohr, K. Schwarz, J. Heiken, and K. Bae. "Efficient correction for CT image artifacts caused by objects extending outside the scan field of view". In: *Medical Physics* 27.1 (2000), pp. 39–46. DOI: 10.1118/1.598855.

[172] J. Hsieh, E. Chao, J. Thibault, B. Grekowicz, A. Horst, S. McOlash, and T. Myers. "A novel reconstruction algorithm to extend the CT scan field-of-view". In: *Medical Physics* 31.9 (2004), pp. 2385–2391. DOI: 10.1118/1.1776673.

[173] Z. Yu, S. Leng, Z. Li, A. F. Halaweish, S. Kappler, E. L. Ritman, and C. H. McCollough. "How low can we go in radiation dose for the data-completion scan on a research whole-body photon-counting CT system". In: *Journal of Computer Assisted Tomography* 40.4 (2016), p. 663. DOI: 10.1097/RCT.0000000000000412.

[174] R. Juran and R. Hinz. "Extrafocal radiation of medical x-ray tubes with a rotating anode". In: *Radiologia Diagnostica* 31.1 (1990), pp. 91–98. ISSN: 0033-8354. URL: http://europepmc.org/abstract/MED/2343094.

[175] S. S. Hsieh and N. J. Pelc. "The piecewise-linear dynamic attenuator reduces the impact of count rate loss with photon-counting detectors". In: *Physics in Medicine and Biology* 59.11 (2014), p. 2829. DOI: 10.1088/0031-9155/59/11/2829.

[176] T. P. Szczykutowicz and J. Hermus. "Creation of an atlas of filter positions for fluence field modulated CT". In: *Medical Physics* 42.4 (2015), pp. 1779–1786. DOI: 10.1118/1.4915123.

[177] S. M. Huck, G. S.-K. Fung, K. Parodi, and K. Stierstorfer. "Optimized intensity modulation for a dynamic beam attenuator in x-ray computed tomography". In: *Medical Imaging 2019: Physics of Medical Imaging*. Ed. by T. G. Schmidt, G.-H. Chen, and H. Bosmans. Vol. 10948. International Society for Optics and Photonics (SPIE). San Diego, CA, USA: SPIE, Feb. 2019, pp. 539–545. DOI: 10.1117/12.2511704.

[178] F. Liu, Q. Yang, W. Cong, and G. Wang. "Dynamic bowtie filter for cone-beam / multi-slice CT". In: *PLoS ONE* 9.7 (2014), pp. 1–10. DOI: 10.1371/journal.pone.0103054.

[179] V. Wu, M. B. Podgorsak, T.-A. Tran, H. K. Malhotra, and I. Z. Wang. "Dosimetric impact of image artifact from a wide-bore CT scanner in radiotherapy treatment planning". In: *Medical Physics* 38.7 (2011), pp. 4451–4463. DOI: 10.1118/1.3604150.

[180] B. Beeksma, D. Truant, L. Holloway, and S. Arumugam. "An assessment of image distortion and CT number accuracy within a wide-bore CT extended field of view". In: *Australasian Physical & Engineering Sciences in Medicine* 38.2 (2015), pp. 255–261. DOI: 10.1007/s13246-015-0353-6.

[181] G. J. Gang, J. W. Stayman, W. Zbijewski, and J. H. Siewerdsen. "Task-based detectability in CT image reconstruction by filtered backprojection and penalized likelihood estimation". In: *Medical Physics* 41.8Part1 (2014), p. 081902. DOI: 10.1118/1.4883816.

[182] F. Farhadi, J. R. Rajagopal, M. Nikpanah, P. Sahbaee, A. A. Malayeri, W. F. Pritchard, E. Samei, E. C. Jones, and M. Y. Chen. "Review of technical advancements and clinical applications of photon-counting computed tomography in imaging of the torax". In: *Journal of Thoracic Imaging* 36.2 (Mar. 2021), pp. 84–94. DOI: 10.1097/RTI.0000000000000569.

[183] E. Wehrse et al. “Photon-counting detectors in computed tomography: from quantum physics to clinical practice”. In: *Der Radiologe* (Feb. 2021), pp. 1–10. DOI: 10.1007/s00117-021-00812-8.

[184] K. Taguchi and J. S. Iwanczyk. “Vision 20/20: Single photon counting x-ray detectors in medical imaging”. In: *Medical Physics* 40.10 (2013). DOI: 10.1118/1.4820371.

[185] M. J. Willemink, M. Persson, A. Pourmorteza, N. J. Pelc, and D. Fleischmann. “Photon-counting CT: technical principles and clinical prospects”. In: *Radiology* 289.2 (Nov. 2018), pp. 293–312. DOI: 10.1148/radiol.2018172656.

[186] K. Taguchi, E. C. Frey, X. Wang, J. S. Iwanczyk, and W. C. Barber. “An analytical model of the effects of pulse pileup on the energy spectrum recorded by energy resolved photon counting x-ray detectors”. In: *Medical Physics* 37.8 (2010), pp. 3957–3969. DOI: 10.1118/1.3429056.

[187] K. Taguchi, M. Zhang, E. C. Frey, X. Wang, J. S. Iwanczyk, E. Nygard, N. E. Hartsough, B. M. Tsui, and W. C. Barber. “Modeling the performance of a photon counting x-ray detector for CT: Energy response and pulse pileup effects”. In: *Medical Physics* 38.2 (2011), pp. 1089–1102. DOI: 10.1118/1.3539602.

[188] S. S. Hsieh and N. J. Pelc. “A dynamic attenuator improves spectral imaging with energy-discriminating, photon counting detectors”. In: *IEEE Transactions on Medical Imaging* 34.3 (2015), pp. 729–739. DOI: 10.1109/TMI.2014.2360381.

[189] H. Atak and P. M. Shikhaliev. “Photon counting CT: Effects of dynamic beam attenuator on image quality”. In: *Nuclear Instruments and Methods in Physics Research Section A: Accelerators, Spectrometers, Detectors and Associated Equipment* 867 (2017), pp. 58–71. DOI: 10.1016/j.nima.2017.04.016.

[190] D. Li, D. Zeng, S. Li, Y. Ge, Z. Bian, J. Huang, and J. Ma. “MDM-PCCT: Multiple dynamic modulations for high performance spectral PCCT imaging”. In: *IEEE Transactions on Medical Imaging* 39.11 (2020), pp. 3630–3642. DOI: 10.1109/TMI.2020.3001616.

[191] M. A. Juntunen, P. Sepponen, K. Korhonen, V.-M. Pohjanen, J. Ketola, A. Kotiaho, M. T. Nieminen, and S. I. Inkinen. “Interior photon counting computed tomography for quantification of coronary artery calcium: pre-clinical phantom study”. In: *Biomedical Physics & Engineering Express* 6.5 (2020), p. 055011. DOI: 10.1088/2057-1976/aba133.

[192] T. Toth, Z. Ge, and M. P. Daly. “The influence of patient centering on CT dose and image noise”. In: *Medical Physics* 34.7 (2007), pp. 3093–3101. DOI: 10.1118/1.2748113.

[193] M. Habibzadeh, M. R. Ay, A. K. Asl, H. Ghadiri, and H. Zaidi. “Impact of miscentering on patient dose and image noise in x-ray CT imaging: phantom and clinical studies”. In: *Physica Medica* 28.3 (2012), pp. 191–199. DOI: 10.1016/j.ejmp.2011.06.002.

[194] T. Kaasalainen, K. Palmu, A. Lampinen, and M. Kortesniemi. "Effect of vertical positioning on organ dose, image noise and contrast in pediatric chest CT—phantom study". In: *Pediatric Radiology* 43.6 (2013), pp. 673–684. DOI: 10.1007/s00247-012-2611-z.

[195] D. Gomez-Cardona, J. P. Cruz-Bastida, K. Li, A. Budde, J. Hsieh, and G.-H. Chen. "Impact of bowtie filter and object position on the two-dimensional noise power spectrum of a clinical MDCT system". In: *Medical Physics* 43.8Part1 (2016), pp. 4495–4506. DOI: 10.1118/1.4954848.

[196] T. P. Szczykutowicz, A. DuPlissis, and P. J. Pickhardt. "Variation in CT number and image noise uniformity according to patient positioning in MDCT". In: *American Journal of Roentgenology* 208.5 (2017), pp. 1064–1072. DOI: 10.2214/AJR.16.17215.

[197] N. Saltybaeva and H. Alkadhi. "Vertical off-centering affects organ dose in chest CT: Evidence from Monte Carlo simulations in anthropomorphic phantoms". In: *Medical Physics* 44.11 (2017), pp. 5697–5704. DOI: 10.1002/mp.12519.

[198] I. Barreto, R. Lamoureux, C. Olguin, N. Quails, N. Correa, L. Rill, and M. Arreola. "Impact of patient centering in CT on organ dose and the effect of using a positioning compensation system: Evidence from OSLD measurements in postmortem subjects". In: *Journal of Applied Clinical Medical Physics* 20.6 (2019), pp. 141–151.

[199] T. Hunger, E. Nekolla, J. Griebel, and G. Brix. "Wissenschaftliche Bewertung und rechtliche Zulassung von radiologischen Früherkennungsuntersuchungen in Deutschland". In: *Der Radiologe* (Oct. 2020), pp. 1–7. DOI: 10.1007/s00117-020-00758-3.

[200] D. Parsons and J. L. Robar. "An investigation of kV CBCT image quality and dose reduction for volume-of-interest imaging using dynamic collimation". In: *Medical Physics* 42.9 (Aug. 2015), pp. 5258–5269. DOI: 10.1118/1.4928474.

[201] T. P. Szczykutowicz, J. Hermus, M. Geurts, and J. Smilowitz. "Realization of fluence field modulated CT on a clinical TomoTherapy megavoltage CT system". In: *Physics in Medicine and Biology* 60.18 (2015), p. 7245. DOI: 10.1088/0031-9155/60/18/7245.

[202] G. Gang, A. Mao, J. Siewerdsen, and W. Stayman. "Implementation and assessment of dynamic fluence field modulation with multiple aperture devices". In: *CT-Meeting: Fifth International Conference on Image Formation in X-Ray Computed Tomography*. Ed. by F. Noo. Salt Lake City, UT, USA, May 2018, pp. 47–51. URL: https://www.ct-meeting.org/data/ProceedingsCTMeeting2018.pdf.

List of Figures

List of Tables

Danksagung

An dieser Stelle möchte ich einigen Menschen, die auf direkte oder indirekte Weise zum Erfolg dieser Arbeit beigetragen haben,

Danke

sagen. Eine Promotion ist, wie vieles im Leben, kein Selbstläufer. Es bedarf Mitmenschen, die hinter einem stehen, die motivieren und inspirieren, die einem "Türen" öffnen aber auch kritisieren und hinterfragen. Ein paar dieser Menschen möchte ich gerne hervorheben und mich für ihre besondere Unterstützung bedanken.

Am Erfolg dieser Arbeit war insbesondere Dr. Karl Stierstorfer (Siemens Healthcare GmbH) beteiligt. Zunächst Danke, Karl, dass du mir die Möglichkeit gegeben hast, dieses Projekt in Kooperation mit Siemens Healthineers durchzuführen. Ich könnte mir kaum ein Promotionsthema vorstellen, dass besser zu mir gepasst hätte. Du warst ein toller Mentor für mich und ich habe von dir viel über die CT Bildgebung gelernt. Für diese Arbeit aber auch darüber hinaus war es wertvoll, dass du mir gezeigt hast, wo ein "hemdsärmliger" Ansatz oftmals ausreicht oder wo stattdessen das Detail im Vordergrund steht. Bei Fragen hast du dir die notwendige Zeit genommen und hast mir ansonsten viel Raum für meine eigenen Ideen gelassen.

Ich möchte mich bei Prof. Katia Parodi (LMU München, Lehrstuhl für Medizinische Physik) herzlich bedanken. Danke Katia, dass du diese Promotion mit viel Interesse akademisch begleitet hast und aufgeschlossen für dieses Promotionsthema warst. Ich schätze die reibunglose, vertrauensvolle Zusammenarbeit mit dir sehr. Mit vielfältigen und interessanten Themen im Rahmen des Curriculums für Medizinphysik hast du bereits während meines Masterstudiums einen wesentlichen Grundstein für meine Freude an der Medizinphysik und damit auch für diese Arbeit gelegt.

Aus der Ferne hat mich Dr. George S. K. Fung (Siemens Medical Solutions US, Inc.) unterstützt. Danke George, dass du – auch wenn wir meist nur über den Atlantik kommunizieren konnten – mir wertvolle Ratschläge weitergegeben hast, für die Zeit am Scanner und für deine unglaublich motivierenden Worte.

Bei der technischen Realisierung war ich auf die Expertise einiger Kollegen aus der Mechanik und Elektronik angewiesen, die mir erfolgreich geholfen haben, funktionsfähige Prototypen zu bauen und in ein CT System zu integrieren. Danke Matthias B., Maurizio B., Robert S., sowie Ralf B., Wolfgang S. und Denise G. für euer Engagement und, dass ihr meine neugierigen Fragen geduldig beantwortet habt.

Außerdem möchte ich mich bei den Kollegen und Studenten in unserer Abteilung, insbesondere Viktor H., Julien E. und Jan M., für eine unterhaltsame, kurzweilige Zeit bedanken. Es war toll, mit euch die Arbeits- und Freizeit zu verbringen und ich freue mich auf zukünftige Dart- und Mölkky-Turniere.

Einen ganz besonderen Dank möchte ich meinen Freunden und meiner Familie widmen, allen voran meinen Eltern, Jenny und Krissi. Jeder von euch hat seinen individuellen Teil dazu beigetragen, wo ich heute stehe. Ihr seid großartig.

Sascha Manuel Huck

Juni 2021